NORTHWESTERN UNIVERSITY

Ultrahigh Vacuum Transmission Electron Microscopy Studies of Semiconductor Surfaces

A DISSERTATION

SUBMITTED TO THE GRADUATE SCHOOL

IN PARTIAL FULFILLMENT OF THE REQUIREMENTS

for the degree of

DOCTOR OF PHILOSOPHY

Field of Materials Science and Engineering

By

Ganesh Jayaram, G., Ph.D.,

EVANSTON, ILLINOIS

December 1995

ABSTRACT

Ultrahigh Vacuum Transmission Electron Microscopy Studies of Semiconductor Surfaces

Ganesh Jayaram

A consequence of the termination of a semiconductor bulk material at the surface is that the atoms on these surfaces typically rearrange themselves in periodicities different from the bulk, i.e., the surface reconstructs, under ultrahigh vacuum (UHV) conditions. This structure needs to be understood prior to characterizing the behavior of metal contacts deposited on to these surfaces. Many structural aspects of the technologically relevant (001) surfaces of Si and GaAs (and that of metals deposited on to them) are subjects of controversy and gaining an understanding of some of these were the principal objectives of this thesis study.

High resolution transmission electron microscopy imaging (HREM) and diffraction (TED) data collected under UHV conditions were analyzed in a qualitative and/or quantitative fashion to shed light on these issues. From quantitative analyses of the intensities of the diffraction spots an asymmetric dimer structure model was proposed for arrangement of atoms on the Si(001)-2x1 surface. A similar rigorous analysis of HREM

(and TED) data resulted in the determination of the geometric structure and chemical identity of species in the annealed Au-Si(001) system. The morphology of the three-dimensional islands of Ag that nucleate and grow on the clean Si(001) surfaces at room temperature was also resolved, primarily from HREM data. The influence of substrate cleanliness on the chemistry of a metal-semiconductor interface, specifically, the Au-GaAs(001) system, was demonstrated from qualitative analyses of data from some preliminary experiments. Finally, the role of deposition parameters, e.g., substrate temperature and metal deposition, in determining the final microstructure of MoS_2 solid lubricant films was elucidated using HREM and TED data recorded under both UHV and conventional vacuum conditions.

These studies demonstrate the potency of HREM and TED techniques in resolving surface atomic structures to accuracies of 0.005nm and also, the necessity for UHV conditions to enable any meaningful interpretation of the collected data. In combination with Auger electron and X-ray photoelectron spectroscopy data, these techniques constitute the ideal surface analysis tool in characterizing the surface completely in terms of both the geometrical arrangement and chemical identity.

Prof. Laurence D. Marks

Department of Materials Science and Engineering

Northwestern University, Evanston Il 60208

ACKNOWLEDGEMENTS

During the course of this thesis study I have had the fortune of interacting with numerous individuals who have helped me mature both professionally and personally. I owe a considerable debt of gratitude to them for their continual support through my many travails.

I am grateful to Prof. L. D. Marks for his guidance and empathy, and for teaching me the art and science of ultrahigh vacuum microscopy.

It has also been my great pleasure to colloborate with Dr. M. R. Hilton at the Aerospace Corporation, CA and I would like to thank him specially for finding the financial resources to support my two trips to the International Conference on Metallurgical Coatings and Thin Films in San Diego, CA.

Members of the Ultrahigh Vacuum Transmission Electron Microscopy group at Northwestern University, both past and present, have contributed in no small measure to my achievements. Among them I would like to thank Dr. Jin Pin Zhang, Dr. Derren Dunn and Dr. Peirong Xu for counselling me on the art of sample preparation and the general aspects of microscopy. I have cherished the company of Dr. N. Doraiswamy (Dorai), Donna Kroening, Boris Vuchic, Richard Plass, Brad Storey, Bob Passeri, Dr. Hong Zhang and those "first years": Christopher Collazo-Davila, Eric Landree and Dan Grozea. Their tolerance of my humor and ego is appreciated.

Friends outside the lab, in the graduate Indian student community : V. Ravikumar

(Ravi), Amit Malik, Rajiv Ramanathan, Karthik Hariharan, Manoj Khangeonkar, Akbar Merchant and Dhruv Agrawal also deserve special thanks.

Finally, this thesis bears a strong testament to the continual emotional blessing and the faith of my family members.

Dedicated to my parents

Mrs. Laxmi Jayaraman and Mr. K. S. Jayaraman

and my uncle

Mr. K. S. Viswanathan

TABLE OF CONTENTS

LIST OF FIGURES AND TABLES

TABLES **PAGE**

1 INTRODUCTION

1.1 Why surfaces ?

The motivation behind studies of the surfaces of materials is probably best summed up in the words of Lord Rayleigh: "The surfaces of bodies are the field of very powerful forces of whose action *we know but little*". Advances in techniques in this century has thankfully mitigated the part of the statement in italics. The first part of the statement, however, still holds true today, and constitutes the underlying theme of the field of surface science.

At a fundamental level surfaces are of great interest because they represent a rather special kind of defect in the solid state[1]. Much of our understanding of solids is based on the fact that they are, in essence, perfectly periodic in three dimensions; the electronic and vibrational properties can be described in detail using methods which rely on this periodicity. The creation of a surface breaks this periodicity in one direction, and can lead to structural changes as well as the introduction of localized electronic and vibrational states. Gaining a proper understanding of these effects is not only of fundamental interest, but is also of use in "real world" applications like heterogeneous catalysis and the fabrication of semiconductor devices. For the latter, the formation of metal-semiconductor junctions with desirable properties is strongly influenced by the tendency for chemical interactions to occur between the metal and the semiconductor. Thin film growth studies also reveal that many materials will not grow in a layer-by-layer

fashion on certain other materials, and these limitations in "atomic engineering" need to be understood properly if exotic multilayer devices are to be built[1].

Most semiconductor surfaces appear to involve some kind of structural rearrangement of the atoms relative to a simple repetition of the bulk lattice. The phenomenon is called *surface reconstruction* and these rearrangements would have to be well characterized prior to attempting a detailed understanding of the behavior of metal on such surfaces. To understand this phenomenon, let us take the case of a clean surface which consists only of atoms that constitute either the bulk or those that have been deposited onto it. This diperiodic structure[2] (periodic in two dimensions) can be thought to arise due to a simple cleavage of the triperiodic structure in the bulk. Thermodynamics dictates that the solid adopts a crystal structure that would minimize its total energy. Therefore, if the cleavage does not perturb the material energetically, the arrangement of atoms on the surface would be exactly the same as a planar termination of the bulk. Such an "ideal surface" is, however, more of an exception than the rule for semiconductors, and this can be understood on the basis of the bonding characteristics of these materials.

Truly directional chemical bonds exist between atoms in both elemental and compound semiconductors, e.g., Si and GaAs respectively. Creation of a surface via cleavage of the bulk material results in dangling bonds. In the case of no atomic relaxation, these dangling bonds would have charge densities that are energetically unfavorable[3]; the material would thus be in an unstable or metastable state. Redistribution of the dangling bond charge density so as to satisfy the valences of all the surface species can be done by forming new bonds at the surface, either between the

surface atoms themselves or between the surface atoms and adsorbates. Atoms involved in such bond formation might also relax structurally, with the relaxation extending from the surface to possibly a few layers into the bulk. Such a relaxation process introduces local strain fields in the material and the balance between the energy cost incurred in this process and the energy gain accompanying a reduction in dangling bond density determines the nature of the surface reconstruction. Given these constraints, whether or not a specific structure is achieved under given surface preparation conditions depends on the kinetic limitations on the atomic motions necessary to achieve it.

The terminology that is commonly used in defining such a surface structure/ reconstruction cell is the one suggested by Wood[2]. The vectors defining the unit mesh of the surface structure are expressed in terms of the underlying mesh of the bulk (the ideal surface described above would therefore be characterized as a (1x1) type, since the locations of atoms on the surface are identical to those in the bulk). For tetrahedrally coordinated semiconductors with either a diamond (Si, Ge) or zincblende (GaAs) structure, the surface cell is defined in multiple units of the bulk cell along the <110> directions, e.g., the Si(hkl)-m x n structure means that the surface cell (h,k and l are the Miller indices of the surface plane) has a periodicity that is m x n times larger than the underlying bulk unit cell along the two mutually orthogonal <110> directions.

Aside from the geometrical arrangement, for a complete description of a solid surface, determination of the identity and concentration of the chemical species present at the surface in question is essential. These two aspects are strongly governed by the outcome of the numerous competitive mechanisms operating at the surface, e.g., gas phase

molecules from the surrounding ambient that condense or adsorb on the surface can either nucleate clusters or diffuse either on or into the surface; evaporation of the surface or adsorbate atoms into the ambient, and diffusion of species from the bulk to the surface is also possible[4]. While for a surface in thermodynamic equilibrium with the environment these mechanisms would all proceed in opposite directions with equal rates, most real life processes like thin film growth are of the non-equilibrium kinetic type and the final morphology depends on a balance between these processes.

For proper characterization of surface properties at the atomic level the composition of the surface should remain essentially constant during the course of the experiment. This requires limiting the rate of arrival of reactive species from the surrounding gas phase in the time-frame of observation, thus necessitating very highly controlled, i.e., ultrahigh vacuum (UHV), conditions. Such conditions become even more imperative for surfaces that react readily with the residual gases in the UHV chamber and undergo either a change in structure or chemistry, or both; a case in point will be highlighted in Chapter 3.

1.2 Surface Characterization Techniques

Broadly speaking, techniques that study surfaces can be classified on the basis of the surface properties that they investigate, e.g., structure, chemical, or electronic. Either an incident beam of electrons or photons is used to probe the surface, and the exiting electrons and/or photons are analyzed to provide the desired information.

Structural information can be gathered in real space using microscopy techniques or in reciprocal space using one of the many diffraction techniques; in some cases, a combination of the two is also used. Data is collected in the serial mode in Scanning Electron Microscopy (SEM), Scanning Transmission Electron Microscopy (STEM) and Scanning Tunneling Microscopy (STM), while Transmission Electron Microscopy (TEM), Reflection Electron Microscopy (REM) and Low Energy Electron Microscopy (LEEM), and the associated companion diffraction techniques of Transmission Electron Diffraction (TED), Reflection High Energy Electron Diffraction (RHEED) and Low Energy Electron Diffraction (LEED) record information in the parallel mode. The above techniques use an incident electron beam to probe the surface; incident photon based techniques for surface structure information include Photoelectron Emission Microscopy (PEEM) and X-ray Diffraction (XRD).

On a similar theme, electronic structure or chemical state characterization of the surface is performed using either an incoming electron-exiting electron probe as in Auger Electron Spectroscopy (AES) and Electron Energy Loss Spectroscopy (EELS), or an incident photon-exiting electron probe as in X-ray Photoelectron Spectroscopy (XPS) and Ultraviolet Photoelectron Spectroscopy (UPS). Since electron spectroscopy techniques are used to resolve the identity of the atomic species, it is relevant to delve into the basics of chemical characterization in some detail.

1.2.1 *Chemical Characterization*

The chemical characterization techniques described above involve detection of electrons in the kinetic energy range of 15-1000 eV emitted or scattered from the first few monolayers of the surface[5]. Of these the ones most commonly used are AES and XPS (and have also been recently added on to the UHV-HREM facility at Northwestern University, as described in Chapter 2).

In AES, one directs a relatively high energy electron beam (> 1 keV) at the surface and collects the spectrum of backscattered electrons, *N(E)*. *N(E)* exhibits an elastic peak due to electrons that pass undisturbed in the solid, and a long, seemingly featureless tail of electrons that have lost energy in the solid. These could be primary electrons that exit the solid after losing energy in a single well-defined event or secondary electrons that lose energy through multiple inelastic collisions. While signal from the latter is truly structureless, the former shows up as small peaks in *N(E)* and more clearly in the derivative signal, $dN(E)/dE$. The precise energy position of the sharp structure in the derivative spectrum is the elemental chemical signature of the surface. The kinetic energy of the Auger electron, E_{KIN}, is given by

$$E_{KIN} = E_{n1} - E_{n2} - E_{n3} \qquad (1.1)$$

where E_{n1}, E_{n2} and E_{n3} are the binding energies corresponding to the level ionized first by the incoming beam, the level from which an electron drops down to fill the initially

ionized level, and the level from which the Auger electron is ejected, respectively. The kinetic energy of the Auger electron is thus independent of the initial mode of ionization.

In XPS too, one takes advantage of the short mean free path of electrons in matter and the elemental specificity of core-level binding energies. A source of monochromatic x-rays, typically MgK_α (1254 eV) or AlK_α (1487 eV), is incident on the sample surface, and the spectrum of emitted electrons is analyzed. This spectrum invariably displays peaks at kinetic energies, E_{KIN}, in the surface sensitive range; these energies are related to the element specific binding energies, E_B, and the incident photoelectron energy, $\hbar\omega$, by the Einstein photoelectric equation

$$E_{KIN} = \hbar\omega - E_B - \phi_s \tag{1.2}$$

where ϕ_s is the spectrometer work function.

1.2.2 *Structure Characterization*

The structure characterization techniques mentioned above differ on the basis of the energy and geometry of the beam incident on the specimen, and thus provide surface information at different sensitivities, i.e., resolution and imaging speed. For example, while relatively low resolution, high speed imaging is possible using REM, LEEM and PEEM, high resolution, slow speed imaging is possible using SEM, STEM and STM.

REM is used in real time to study growth, electromigration and surface structural

changes induced on heating to temperatures as high as 1200°C[6-9], while its diffraction mode, RHEED, is the most commonly used technique to study the surface structure, and/or morphology evolution during thin film deposition, e.g., the real time dynamic surface measurements performed during MBE growth of GaAs(001)[10-12]. However, REM suffers from geometric distortions due to the grazing incidence and the resolution is limited at present to about 0.2nm in the plane and 0.9nm perpendicular to the beam.

Such distortions are avoided by both LEEM and PEEM. Very low energy electrons (~5-200eV) are used in LEEM and LEED studies to achieve high surface sensitivities. LEEM has been used to image in real time, thermally activated surface processes[13,14] including changes in surface morphology[15] and epitaxial growth during metal deposition[16-20] with a current spatial resolution of 20nm. Intensities in LEED patterns have been quantified and used to identify and resolve many surface structures, e.g., the simple dimer structure of the Si(001)-2x1 surface was first proposed[21], and subsequently modified using LEED[22]. Spectroscopic variations of LEEM can also be used to provide spatially resolved compositional information (Auger electron emission spectroscopy), albeit, with corresponding loss of speed[23,24].

In comparison to REM and LEEM, PEEM has a lower resolution (of about 200nm) due to the energy spread of the incident photons when no energy analyzer is used; this has however proved to be more than adequate in resolving the spatial chemical kinetics of reaction processes[25]. Addition of an energy analyzer improves the spatial resolution (down to 10-50nm) at the cost of signal, and hence, speed[26-31].

SEM scans the incident electron beam over the surface and images are formed

using the secondary electrons emitted from the sample. Resolution down to 5-10nm can be obtained using a field emission cathode[32], and when used under UHV conditions, can have sub-monolayer sensitivity[33-35]. In STEM, an electron probe is scanned serially over the sample, similar to a SEM, and the transmitted electrons as well as any surface scattering processes are used to obtain images[36-39]. With this approach, Auger images at a resolution of about 2nm have been obtained. In principle, the type of techniques used to image surfaces in transmission (see below) can also be used in such an instrument, although to date this has not been done. In many respects rather similar to the SEM and STEM, STM uses an atomically sharp metal tip to scan at heights ~ 0.5nm above the surface and the tunneling current between the tip and the surface is used to probe the local structure and morphology. Lateral and vertical resolutions down to 0.3nm and 0.001nm are obtainable using STM; however, there is a smaller field of view, the data collection is slower, and is limited by the scanning speed of the tip. In addition to surface structure information at the atomic level, it is also possible to image real time kinetic processes, e.g., formation of domains[40], motion of steps[41], vacancies[42] and static processes, e.g., epitaxial growth[43,44] using a STM.

The above techniques all use processes which are specifically surface sensitive and thus the majority of the signal comes from the first few surface monolayers. However, most of them, with the exception of REM, STEM, and STM, suffer from the common problem that the probe averages over a large area, and thus information from near-ideal crystal regions and regions with imperfections like steps, kinks etc., all contribute to the final signal. An inherent limitation therefore is that inhomogeneous surface processes at

the atomic level, which play a significant role in thin film epitaxy, cannot be characterized. Also, little information on the interaction of the bulk defects with the surface is revealed from LEEM, REM, and STM studies. This assumes importance since erroneous interpretation of the state of the material is possible when one gleans such information solely from the LEED and RHEED patterns, e.g., sharp reconstruction spots in LEED and RHEED patterns are usually taken as indicators of a well ordered material; however, a TEM image from a region showing similar patterns in the case of the Si(111)-7x7 reconstructed surface revealed an extensive amount of defects in the bulk[45]. STM studies are further limited to conducting materials since electrons have to tunnel between the tip and the surface. Although the very high surface-only sensitivity of the STM provides an excellent picture of the surface structure, it has also proved to be a limitation in other cases, e.g., in deciphering the structure of the Si(111)-7x7 surface, where the reconstruction proceeds many layers into the bulk. Therefore a technique that is highly sensitive to both the surface and the bulk and can also be interfaced with chemical characterization techniques is highly desirable.

TEM imaging, and the companion diffraction technique, TED, offer such a solution. In the plan view transmission geometry described in the following chapter, electrons carry information from both the surface (top and bottom) and the bulk. The surface signal in this case is therefore relatively weak, and isolating surface information is a more complex task; in this respect, the transmission technique differs from the above in terms of the surface sensitivity of the scattering process. Furthermore, unlike STM, SEM, REM, etc. which can look at bulk crystals, extensive sample preparation is required

so that the crystal is electron transparent, i.e., a few hundred Angstroms thick ideally. Despite these disadvantages, the TEM imaging and TED techniques are very powerful tools in surface science analysis, e.g., unlike STM, TEM can look at insulators and can also provide information on bulk defect interaction with the surface. Further, atomic resolution on a scale similar to the STM has been recently reported, e.g., of Bi atoms on Si(111) surface[46] and the Ir(001)-5x1 surface[47]. Finally, dynamic processes like surface modifications under high temperatures and gas etching treatments[48], and *in situ* growth[49,50] can also be imaged. Information about the structure of the surface (and any morphological changes) can also be obtained from quantitative analysis of intensities in TED patterns[51-54]; in fact, a combination of diffraction and imaging techniques is almost always used in characterizing a material in a TEM.

A combination of these techniques was used in the course of my graduate study to characterize, mainly, the structure of the (001) surfaces of Si and GaAs, and that of metal deposited on to them, in an ultrahigh vacuum high resolution transmission electron microscope (UHV-HREM). The motivation behind the choice of the systems was that in spite of their higher technological relevance (since they are the primary growth faces of device material), the (001) surfaces have been relatively less researched than the cleavage planes in these materials, i.e., the (111) plane in Si and the (110) plane in GaAs respectively. Also, the nature of the reconstruction mechanism, i.e., atom dimerization, for these surfaces remains a point of controversy.

More specifically, models for the surface structure of clean Si(001) and annealed Au-Si(001) systems were proposed from quantitative analyses of diffraction and imaging

data respectively, and interesting growth morphologies (and structure) revealed for Ag films deposited on clean Si(001) surfaces at room temperature. The viability of preparing clean surfaces of GaAs(001) was investigated, and the behavior of Au deposited on to surfaces of differing cleanliness charted.

Studies on the influence of different deposition parameters on the final microstructure of MoS_2 solid lubricant thin films were also conducted (as part of a collaborative effort with Dr. M. R. Hilton at Aerospace Corporation, CA) in both the ultrahigh vacuum and conventional vacuum microscopes, to gain better insight into their fracture behavior, and storage and contamination issues for application in space mechanisms.

This thesis dissertation is organized in the following manner. Chapter 2 details the experimental techniques and the surface science instrumentation used in these studies. Results on the structure of clean Si(001) surfaces and that of metals deposited on to them are presented in Chapters 3 and 4 respectively, while those on the GaAs(001) and MoS_2 systems are detailed in Chapters 5 and 6. Chapter 7 highlights the ramifications of these studies and presents suggestions for future work.

Specific contributions that I would like to acknowledge are those of Prof. L. D. Marks for coding the routines used in structure determination of the clean Si(001) and the Au-Si(001) surfaces, Dr. D. Narayanaswamy for carrying out the data reduction in the Ag-Si(001) system, Dr. M. R. Hilton for providing the films and valuable insights into the characterization study described in Chapter 6, and Christopher Collazo-Davila and Eric Landree for much of the data collection on the SPEAR.

2. EXPERIMENTAL TECHNIQUES

Prior to detailing the experimental aspects of the transmission imaging and diffraction techniques, a brief description of the underlying theory in each case is presented here. A more complete explanation can be found in books[55-58] on these topics.

2.1 Diffraction

2.1.1 *Kinematical Theory*

The simplest approach to describing diffraction from a crystal is to use the Kinematical theory where the incoming electron beam is assumed to be elastically scattered once by the crystal planes in the material. Elastic scattering is the term used to define those scattering processes in which the energy of the electron is not changed. The momentum of the electron is, however, changed, and an angular distribution of electrons, characteristic of the scattering body, is observed in the diffraction patterns. (Since the scattering body, i.e., the atoms, molecules, etc. recoils as a whole in this process, due to its large mass, an insignificant transfer of energy from the incident electron to the body occurs.)

This elastic scattering process is described by the solution of the non-relativistic Schroedinger wave equation, i.e.,

$$\nabla^2\psi(\underline{r}) + (8\pi^2 me/h^2)\ \{E + V(\underline{r})\}\ \psi(\underline{r}) = 0 \qquad (2.1)$$

where $V(\underline{r})$ is the crystal potential in volts, E the accelerating voltage applied to the electrons, m the electron mass and $\psi(\underline{r})$ the probability wave for the electron. In the absence of a crystal, i.e., $V(\underline{r}) = 0$, the solution for the above equation is a plane wave of the form

$$\psi(\underline{r}) = \exp(2\pi i \underline{k}.\underline{r}) \tag{2.2}$$

where the magnitude of $\underline{k}$, the wave vector, is defined as

$$|k| = 1/\lambda = \underline{p}/2\pi h \tag{2.3}$$

where $h^2k^2/2m = eE$ (2.4)

In the above equations $\underline{p}$ is the electron momentum, λ the electron wavelength and m the relativistically corrected mass of the electron. The magnitude of the wave vector is thus defined by the electron energy and its direction by the lenses and deflection system above the specimen (the direction after the specimen is determined by the scattering of the wave as it passes through the crystal). In the presence of a crystal potential, i.e., a positive or a negative charge, the incident plane wave defined by equation 2.2 would get scattered from each such point resulting in a spherical wave. The amplitude (and phase) of such a wave scattered from a single point $\underline{r}$, is equal to

$$-(2\pi ime/h^2k)\ V(\underline{r}) \tag{2.5}$$

where the term $2\pi me/h^2k$, in the above equation, is defined as the interaction constant, σ. At large distances away from the crystal, this spherical wave can be considered equivalent to a plane wave, given by

$$\psi(\underline{r}) = -(i\sigma) \int V(\underline{r}) \exp(2\pi i \underline{k}.\underline{r}) . d\underline{k} \qquad (2.6)$$

The integral is used to sum waves that have wave vectors of the same magnitude but are in different directions, and is called a Fourier integral. Since such scattering occurs from many different points in the crystal, at a point $\underline{R}$ away from the sample the final wave would be defined by either the constructive or destructive interference of these spherical wavefronts. The wave scattered in a direction $\underline{k}'$ can then be written as

$$\Psi(\underline{k}') = -(i\sigma) \int V(\underline{r}) \exp(2\pi i \, [\underline{k}-\underline{k}'].\underline{r}) \, d\underline{r} \qquad (2.7)$$

where $[\underline{k}-\underline{k}'].\underline{r}$ defines the phase shift due to scattering from two points spaced $\underline{r}$ apart. Defining the difference between the scattered and incident wave vectors, i.e., $\underline{k}'-\underline{k}$, as the scattering vector, $\underline{u}$ (its magnitude is the spatial frequency in reciprocal/diffraction space), the above equation reduces to

$$\Psi(\underline{k}') = -(i\sigma) \, V(\underline{u}) \qquad (2.8)$$

where $V(\underline{u})$ is the Fourier transform of the crystal potential $V(\underline{r})$, i.e.,

$$V(\underline{u}) = \int V(\underline{r}) \exp(-2\pi i \underline{u}.\underline{r})\, d\underline{r} \qquad (2.9)$$

The relative strength of diffraction of the incident wave into different scattering vectors can then be mapped using the Ewald sphere construction. In the case of elastic scattering, the magnitude of the incident and scattered wave vectors would be equal, i.e., $k = k'$. The intersection of $V(\underline{u})$ with a sphere of radius equal to the wave vector (at the high voltages used in TEM, this sphere can be considered planar, from equation 2.4) defines the amplitude of the wave at each point $\underline{u}$. The intensity is then given by

$$I(\underline{k}) = \Psi(\underline{k}') \Psi^*(\underline{k}') \qquad (2.10)$$

While a qualitative description of the diffraction process and the intensities is thus possible using a kinematical approach, it suffers from many drawbacks.

a) The single scattering assumption is based on a weak interaction of the electron with the crystal, i.e., for small values of $\sigma V(\underline{u})$. Such an approximation would therefore be valid only in describing intensities arising due to scattering from single atoms of weak crystal potential, i.e., low atomic number (since σ is nearly constant at the high voltages used in TEM's). In all other cases multiple scattering processes would have to be considered, and in this scenario the wave would scatter from the diffracted beam into other directions (in addition to scattering back into the incident direction). Under such circumstances, the kinematic theory assumption of the transmitted beam being very much stronger than the diffracted beam would be invalid.

b) In the case of thicker materials (5 to 10 times the mean free path of elastic scattering), the assumption of only elastic scattering does not hold true and in fact, the intensities of the beams are damped due to inelastic scattering. Much of this scattering occurs at very small angles (e.g., 0.1-1 mrad) and broadens the sharp Bragg spots. In thicker samples, different processes, e.g., thermal diffuse scattering (arising from motion of atoms in solids), single electron excitations (which is the origin of the peaks in energy loss spectra) or plasmons (which are collective excitations of the electrons), result in a broad continuous intensity distribution. Finally, when an objective aperture is used to form images, electrons that scatter inelastically outside of the aperture do not contribute to the final image and are thus effectively absorbed.

The intensity of the spots results from a combination of these processes and these effects are taken into consideration in the more rigorous dynamical theory which considers the coherent interactions of many hundreds of diffracted beams produced simultaneously inside a crystal.

2.1.2 *Dynamical Theory*

In contrast to the kinematical theory, the amplitude of the incident (and diffracted) wave is allowed to vary with depth in the crystal. In the simplest case involving the incident beam and a single strongly diffracted beam, i.e., the two beam approximation, the wave function is defined as

$$\psi(\underline{r}) = \phi_o \exp(2\pi i \underline{k}.\underline{r}) + \phi_u \exp(2\pi i \underline{k}'.\underline{r}) \quad (2.11)$$

where ϕ_o and ϕ_u represent the amplitudes of the incident and scattered wave, with $\underline{k}$ and $\underline{k}'$, the corresponding wave vectors. Similar to the kinematical theory described earlier, the two wave vectors are related by

$$\underline{k}' = \underline{k} + \underline{u} + \underline{s} \quad (2.12)$$

where the additional term $\underline{s}$, denotes a vector of magnitude equalling the deviation of the spot from the Ewald sphere in an off-Bragg case. The change in amplitude of the beams on passing through a slab of thickness dz is then given by

$$d\phi_o/dz = \pi i \phi_o/\xi_o + \pi i \phi_u \exp(2\pi i s z)/\xi_u \quad (2.13)$$

$$d\phi_u/dz = \pi i \phi_u/\xi_o + \pi i \phi_o \exp(-2\pi i s z)/\xi_u \quad (2.14)$$

where ξ_o and ξ_u represent the inverse of the atomic structure amplitude for the corresponding angles. This pair of coupled first order differential equations (also called the Howie-Whelan equations) linking the wave amplitudes of the incident and diffracted beam is regarded as the basic formulation of the dynamical theory.

An approach to model the intensities in the transmitted and diffracted beams due to such dynamical scattering phenomena in crystals was formulated by Cowley and Moodie[59]. In their formulation, the crystal is sliced into layers of infinitesimal thickness

(a few angstroms at most) along the beam direction, i.e., the multislice algorithm. An approximation is made that the scattering from any individual slice occurs on a single plane, and may be described by a "transmission function". A "propagation function" is used to describe the phase change of the wave function to the next plane, through an uniform medium (vacuum). This process of transmission followed by propagation is repeated for each slice sequentially until the bottom surface is reached, yielding the exit wavefunction of the electron. The transfer function of the microscope's objective lens, as will be detailed in the section on imaging theory, is applied to convert the phases of the beams at the exit surface of the crystal into phases which actually contribute to the final image.

2.1.3 *Experimental*

Diffraction data can be recorded in either the on-zone axis mode, where the incident electron beam is parallel to a major zone axis of the material, or in the off-zone axis mode, by tilting off the crystal zone axis. The off-zone mode is the one primarily used in surface structure studies, since it yields surface-sensitive information at high levels of accuracy[51]; this can be explained using the Ewald sphere construction.

In TEM samples, the thickness along the beam direction (a few tens of nm) is orders of magnitude smaller than the dimensions in the plane perpendicular to it (a few mm). Therefore, by the principle of reciprocity, there exist rods of intensity called rel rods in diffraction space in the direction parallel to the incident beam. It should also

become apparent that the rel rods from the surface layer will be longer than those arising from the bulk. Tilting off the zone axis therefore results in a more dramatic drop in the intensities of the bulk reflections relative to those of the surface, since a smaller portion of the corresponding rel rods now intersects the Ewald sphere, as illustrated in Figure 2.1.

To obtain the final surface structure using such data, either a kinematical or a dynamical approach as detailed above is used to numerically calculate the intensities that would arise from an initial model for the surface cell. The absolute intensities of the surface diffraction spots thus calculated are then compared against ones recorded experimentally, and the difference is minimized via numerical calculations in an iterative fashion to yield the final model. The kinematical approach was used rather successfully to solve the structures for Si(111)-7x7[51,52] and Si(111)-7x7:O surfaces[53], while the more rigorous dynamical approach was used in resolving the details of the Ir(001)-5x1[54] surface.

These surface structures can also be studied directly from HREM images. Rather analogous to the approach used in TED analyses, high surface sensitivities are obtained in the off-zone mode, as aptly demonstrated in the studies of the Si(111)-7x7[51] and Ir(001)-5x1[47] systems. The following section reviews the theory behind the general imaging process and also describes the different experimental imaging modes (classified on the basis of either the beams used in imaging or the specimen geometry with respect to the incident beam) for surface studies.

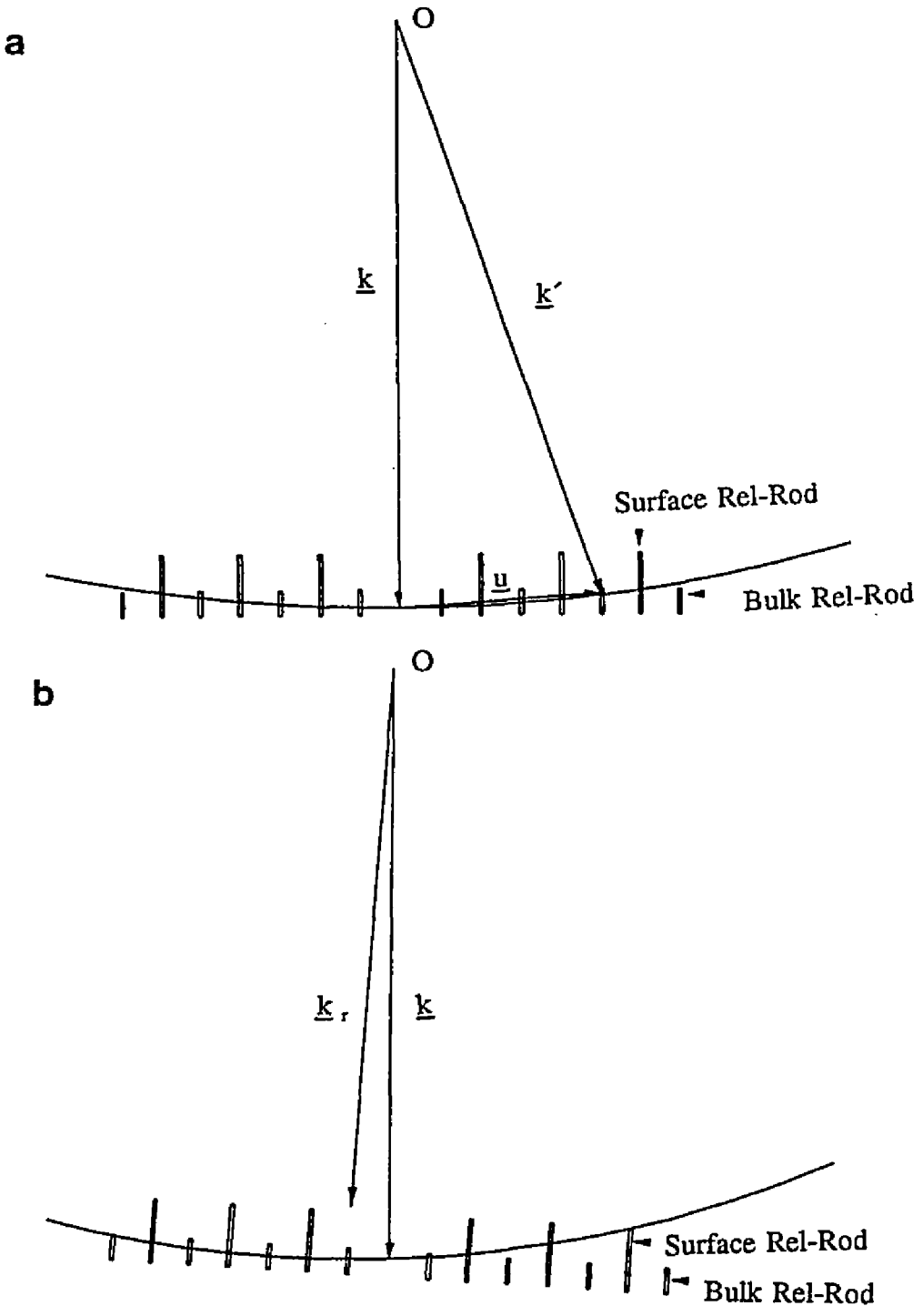

Figure 2.1. The Ewald sphere construction for (a) on-zone axis and (b) off-zone axis modes. O is the origin of the Ewald sphere, while $\underline{k}$, $\underline{k}'$, and $\underline{u}$ are the wave vectors defined in the text. $\underline{k}_r$ is the reference vector perpendicular to the reciprocal lattice and the angle between $\underline{k}$ and $\underline{k}_r$ in (b) defines the magnitude of the crystal tilt.

2.2 Imaging

2.2.1 *Theory*

The electron wave exiting the specimen is magnified by the magnetic lenses in the microscope to produce an image; these magnetic lenses are relatively imperfect (in comparison to the optical lenses) and have aberrations which limit the attainable resolution in different ways. The aberrations can be classified into two types: coherent, i.e., ones that introduce a fixed phase shift to the exit wave, and incoherent, i.e., ones that introduce a random phase shift to the exit wave. Defocus (varying the plane of focus by changing the current in the objective lens), astigmatism (arising due to defects in the pole piece), beam tilt (orientation of the incident beam with respect to the optic axis of the objective lens), and spherical aberration (which brings waves travelling in different directions into focus at different positions) are of the coherent type, while focal spread (spread in focus in the image due to ripples in objective lens current and energy spread of the electron source), drift, vibration, and beam convergence (range of angles that are used to form the image) are incoherent aberrations.

For an objective lens defocus of Δz and spherical aberration coefficient C_s, in the absence of beam tilt the wave exiting the specimen undergoes a coherent phase shift $\chi(u)$ at each spatial frequency $\underline{u}$ (defined in the two dimensions perpendicular to the beam); this phase shift term is defined as

$$\chi(\underline{u}) = \pi\Delta z\lambda\underline{u}^2 + 0.5\pi C_s\lambda^3\underline{u}^4 \qquad (2.15)$$

(If a small beam tilt ($\underline{w}$) is present, $\underline{u}$ in the above equation is replaced by $\underline{u}$-$\underline{w}$).

Its action on the incident plane wave in reciprocal space results in the modification:

$$\psi(\underline{u}) \text{ ----> } \psi(\underline{u}) \exp[-i\chi(\underline{u})] \tag{2.16}$$

In the absence of any beam convergence or energy spread (i.e., neglecting the incoherent aberrations), the final image can be written as[60]

$$I(\underline{r}) = \left| \mathcal{F}^{-1} \{\psi(\underline{u}) \exp[-i\chi(\underline{u})]\} \right|^2 \tag{2.17}$$

with $\mathcal{F}^{-1}$ denoting an inverse Fourier transform.

If the convergence and energy spread terms are included, the final image intensity would have to be summed over a range of these values. In a linear imaging model (analogous to kinematical diffraction) which does not consider the effects of multiple scattering, these incoherent phase shift terms are collectively defined as the envelope term, $E(\underline{u})$. This term damps out the frequencies that can be obtained in the image, thus defining the fundamental limit to the attainable resolution, and is of the form

$$E(\underline{u}) = S(\underline{\nabla}\chi(\underline{u})/2\pi)F(\lambda \underline{u}^2/2) \tag{2.18}$$

where S and F are the cosine Fourier transforms of the convergence and focal spread terms respectively.

In case of very weakly scattering specimens and for images recorded off the zone, a simple linear imaging theory[57,58] in combination with a weak scattering object (changes the phase and amplitude of the incident wave only slightly) approximation can be used to explain the recorded HREM images. The intensity at each point $\underline{r}$ can then be expressed as:

$$I(\underline{r}) = 1 + \sigma t \int [\{A(\underline{u})\cos\chi(\underline{u}) + B(\underline{u})\sin\chi(\underline{u})\}E(\underline{u}) + \eta(\underline{u})] \exp(2\pi i \underline{u}.\underline{r})\, d\underline{u} \qquad (2.19)$$

where $A(\underline{u})$ and $B(\underline{u})$ are the real and imaginary parts of the crystal potential, $V(\underline{u})$, in Fourier space, $\eta(\underline{u})$ is the background noise due to the statistics of the recording process and t the thickness. The lens system thus acts as a filter since only certain spacings are allowed to contribute to the final image while others are not; the contrast of the spacings are also changed in this process. To faithfully reconstruct the exit wave, these parameters should therefore be known; the process used in reconstructing the wave exiting an annealed Au-Si(001) surface is detailed in Chapter 4.

In the imaging process described above, the lattice fringes arise from the interference of the phases of the incident beam and all other diffracted beams (and also between diffracted beams themselves, in non-linear imaging); such images are therefore also called phase contrast images. It is also possible to select the beams that would contribute to the final image by masking out the rest using a physical aperture in the objective lens region. Images thus recorded are called diffraction contrast images.

2.2.2 *Diffraction Contrast Imaging*

The bright field mode derives its name from the fact that images recorded in this mode appear bright in the absence of a specimen; this arises since only the transmitted beam is used in the imaging process. Analogously, the dark field mode uses specific diffracted beams for imaging purposes, and consequently the images appear dark in the absence of a specimen. In the low resolution mode these two techniques are used mainly in defect and strain field analyses, while at higher resolution these can provide information on the surface domains[61-63]. Surface steps have been imaged using the bright field mode, e.g., MgO[63], while dark field imaging using forbidden reflections can be used to obtain contrast from surface terraces with atomic height steps as in case of Au(111)[64] and Au(001)[65]. Atomic scale steps on thin MgO crystals have also been revealed using weak-beam dark field imaging[66].

Differentiation is also possible on the basis of the geometry/orientation of the imaged surface to the incident beam (see some general reviews[60,67-69]), and the two such modes are profile and plan view.

2.2.3 *Profile Imaging*

In this case, the electron beam is parallel to the surface of interest and the surface profile is therefore imaged. If the surface involved is very thin, under the correct defocus conditions[70] the image can be interpreted in terms of the atomic positions on the surface. This mode provides information about displacements/ relaxations along the side surface,

i.e., normal to the top and bottom surfaces, and also translations perpendicular to the beam. It was first used to study the Au(110)-2x1 surface[71] and small particles[72], and has been used with considerable success in imaging surfaces of gold[71,73], silicon[74], germanium[75] and cadmium telluride[76]. Although very powerful, it suffers from two problems. The first is due to the fact that the surface imaged is very thin, and the structures may not accurately represent extensive two-dimensional surfaces. A more fundamental limitation is that a very thin region of the surface is intrinsically unstable, thermodynamically, and obtaining an equilibrium surface configuration is, therefore, exceedingly difficult, if not impossible.

2.2.4 *Plan View Imaging*

In this case, the electron beam is normal to the surface of interest, and interacts with the top and bottom surfaces, and the bulk material in between. A very important advantage is that one can approach thermodynamically stable flat surfaces, unlike the profile mode. Although one might think that the surface information would be obscured by the far stronger bulk scattering processes, as illustrated above (in section 2.1.3) this is not the case and it has turned out to be surprisingly simple to obtain surface information. Surface studies using the bright field, dark field, and high resolution techniques described above[46,47,61-66], and the ones reported in this thesis were all carried out in this mode.

2.3 Why a UHV-TEM ?

While investigations of surfaces at the atomic scale using these above techniques in conventional vacuum microscopes (10^{-4} to 10^{-6} Pa) are now fairly commonplace, the study of *clean* surfaces, as alluded to earlier, necessitates a well-controlled UHV environment. Further, thin film growth and/or annealing studies require incorporation of the accessories, i.e., for ion sputtering, annealing, gas etching, thin film deposition, RHEED, etc. either on to the microscope column itself (termed the *in situ design)*, which might affect the resolution, or in an attached UHV-surface science chamber (*ex situ design).* In both cases, from the point of view of HREM, there exists the problem of damping out the vibration induced by such add-ons. A challenge is therefore involved in designing a functional UHV-TEM and their sparse number bear a strong testament to this fact; a brief review of the developments in UHV-TEM technology is presented here.

That carbonaceous contamination of the surface results from electron bombardment of the residual hydrocarbons in conventional vacuum (~10^{-3} Pa) TEM's was first demonstrated by Ennos[77], while a separate investigation by Bassett[78] affirmed the need for better vacuum conditions around the specimen. Although the need for controlled UHV conditions around the sample region was appreciated following these studies, it was only in the late 1960s that rapid advances in stainless steel UHV technology enabled fabrication of the first UHV-TEM's.

Initial approaches to attain UHV conditions at the specimen region used either cryopumps[79-81] or an independent UHV chamber around the sample[82,83]. The *in situ design*

approach had two problems: the final pressure was at times compromised to the 10^{-7} Pa range due to degassing from viton seals, components, etc. of the accessories[84,85], while in cases where such add-ons necessitated considerable volume changes in the pole piece region of the TEM, a compromise on the HREM capabilities was inevitable[86]. Despite these limitations, both moderate[87], and high resolution[88] studies have been reported. The *ex situ design* approach was adopted by Profs. L. D. Marks and P. Stair in designing the UHV-HREM-surface science facility at Northwestern University. (A similar approach has been adopted more recently by Dr. R. Tromp and co-workers at IBM Corporation in their design of a UHV-HREM facility.) Since a significant portion of my graduate research involved the use of this facility and also by virtue of the fact that it still remains one of the very few, truly high resolution UHV-TEM's, its features are highlighted below.

2.4 The UHV-HREM facility

The facility comprises two main parts: a high resolution transmission electron microscope, and an attached surface science module; both chambers can be maintained under UHV conditions over significant periods of time.

2.4.1 *UHV-TEM*

The microscope is a Hitachi UHV H-9000 instrument that was targeted to achieve pressures in the low 10^{-8} Pa in the sample region when first delivered over eight years ago. Similar to the standard H-9000 version, this microscope is differentially pumped so

that the best vacuum conditions exist in the objective lens region. Differential pumping is achieved by operating a 60 l/s ion pump on the gun housing, and a 20 l/s diode ion pump each on the condenser, selected area, and projector lens region. A combination of a 420 l/s magnetically levitated, shock isolated tandem turbomolecular pump backed by a 1000 l/s home-built titanium sublimation pump operates on the objective lens region alone. This pumping system can maintain clean conditions subject of course to no leaks, power shutdowns, etc. Ringheaters mounted on the external flanges of the instrument and internal quartz halogen lamps (in the objective region) facilitate bake-outs to about 200°C.

UHV conditions are defined not only by the total pressure at the objective region, but also (in fact, mainly so) by the partial pressures of the residual gases, i.e., H_2, H_2O, CH_4 and CO. For example, despite the pumping methodology described above, one of the primary constituents of the well-baked out microscope was water vapor (read out using a quadrupole mass spectrometer); the source was traced to be the projector lens region, where the pumping was conduction limited. Therefore, over the past year or so, a modification to the pumping line was incorporated in the form of an additional set of bellows which connects this region directly to the turbomolecular pump facilitating pump-out of the water vapor during the bake-out. This set-up has enabled the system to operate successfully at stable pressures of 5×10^{-9} Pa.

Besides the pumping characteristics, other features of the instrument include:

1) A LaB_6 filament for relatively low energy spread and high brightness.
2) A TV rate camera to record images in real time.
3) A computer controlled image acquisition system (ITEX) that enables grabbing and

digitizing of images for on-line analyses.

4) A Gatan Parallel Electron Energy Loss Spectrometer (PEELS) unit to enable chemical characterization of the region being imaged, and

5) Tungsten evaporation filaments mounted via an external flange in the condenser region, facilitating *in situ* metal deposition studies.

2.4.2 *UHV-SSC*

Surface preparation was carried out in a UHV-Surface Science Chamber (UHV-SSC), coupled to the UHV-TEM via a gate valve; specimen transfer between the chambers was conducted under UHV conditions. Figure 2.2 shows a schematic of the original setup of the facility used in nearly all the studies reported in this thesis. Sample loading into the UHV-SSC from air was usually done through a load lock chamber, and the two chambers were isolated from each other via a gate valve. When the UHV-SSC was brought up to air, initial roughing down was done using a turbomolecular pump, while a combination of a 60 l/s ion pump and a 400 l/s titanium sublimation pump (and bake-outs) was used to achieve static pressures in the range of 5×10^{-9} Pa; the total pressure and component percentages being monitored using a quadrupole mass spectrometer. Surface science accessories mounted on the chamber included:

1) A differentially pumped Perkin-Elmer model # 04-300 ion gun for generating argon, xenon, or neon ion beams in the energy range of 2-5 kV which could be focussed down to a size of < 2 mm. These beams were used to sputter contaminants, mainly carbon, off

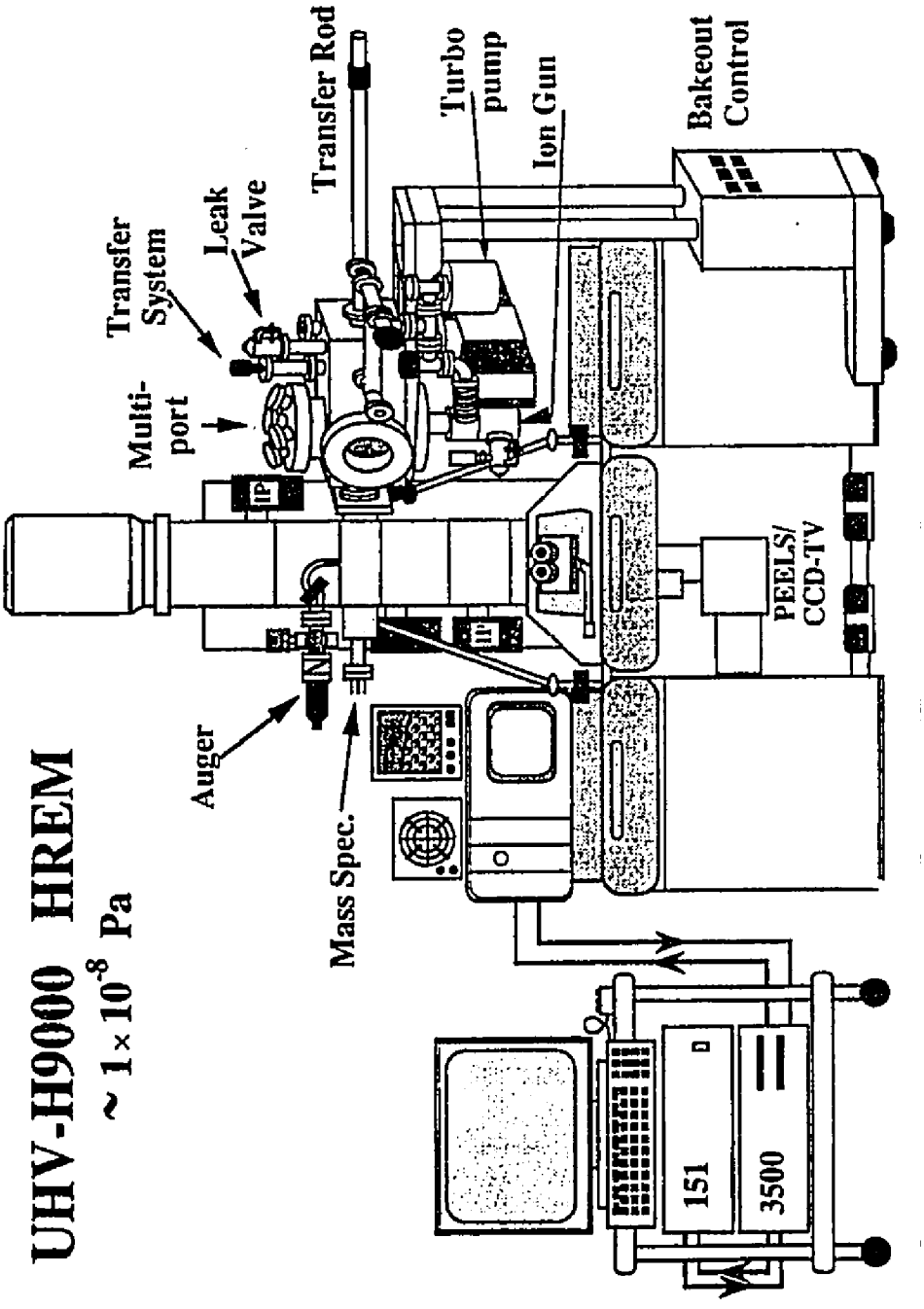

Figure 2.2. A schematic diagram of the original UHV-HREM facility comprising the UHV-H9000 microscope and the attached UHV-surface science chamber (courtesy of Dr. John Bonevich).

from the surface and also create thin areas, when the sample became too thick to be imaged in transmission.

2) A Kimball-Physics model # EMG-14 electron gun that could deliver up to 10 kV electrons at a current of 5 mA into a probe of diameter < 1 mm on the sample. The electron beam was used to anneal the damage introduced in the sample by the milling process described above.

3) Tungsten evaporation filaments, which when resistively heated, would deposit metal on to surfaces of interest.

4) A rotary-linear feedthrough, called the Transfer rod in the schematic, to transport the sample cartridge between the UHV-SSC and the UHV-TEM, and

5) A sample grabber mechanism, labelled as Transfer system in the schematic, to transfer the microscope cartridge between the UHV-SSC and the load lock chamber. This mechanism enabled the sample cartridge to be either detached from or lock into the Transfer rod inside the UHV-SSC. The cartridge was then rotated around by 90° and locked into a similar Transfer rod mechanism operating in the load lock chamber (the reverse procedure was followed during transfer into the UHV-SSC).

Although many clean surfaces were prepared and investigated using this setup, the facility suffered from a few drawbacks:

1) Only one sample could be loaded in at any given time resulting in large time delays between successive experiments.

2) Further, since almost 80-90% of the experimental time on the facility was devoted to preparation of a clean surface the UHV-TEM was not exploited to its fullest potential in

terms of data collection.

3) Finally, chemical characterization of the surfaces performed using PEELS in the transmission mode was limited in sensitivity to at best a few monolayers.

A step to alleviate these problems was taken over the past year with the replacement of the UHV-SSC by a multichamber Sample Preparation, Evaluation, Analysis, and Reaction (**SPEAR**) facility designed by Superior Vacuum Technology; the set-up is shown in Figure 2.3.

2.4.3 *SPEAR*

The SPEAR consists of a central transfer chamber which is attached to an Analytical chamber, and a Molecular Beam Epitaxy (MBE) chamber. The transfer chamber is pumped by a 400 l/s ion pump, while the MBE and analytical chambers are each pumped by a 220 l/s ion pump; each ion pump is in turn backed by a titanium sublimation pump. This combination enables all three chambers to reach a vacuum of 10^{-9} Pa. Specimen loading into or retrieval from the transfer chamber is done via a loadlock chamber, which is pumped down by a 210 l/s turbomolecular pump to the 10^{-8} Pa range in 6-12 hours. The transfer chamber consists of two sections at different heights: one which is attached via the gate valve to the UHV-TEM and the other, attached to the MBE, analytical, and load lock chambers. A linear transfer rod moves the sample between the UHV-TEM and the upper section, while a central linear-rotary transfer arm is used to transfer samples between the lower section and the other chambers in the

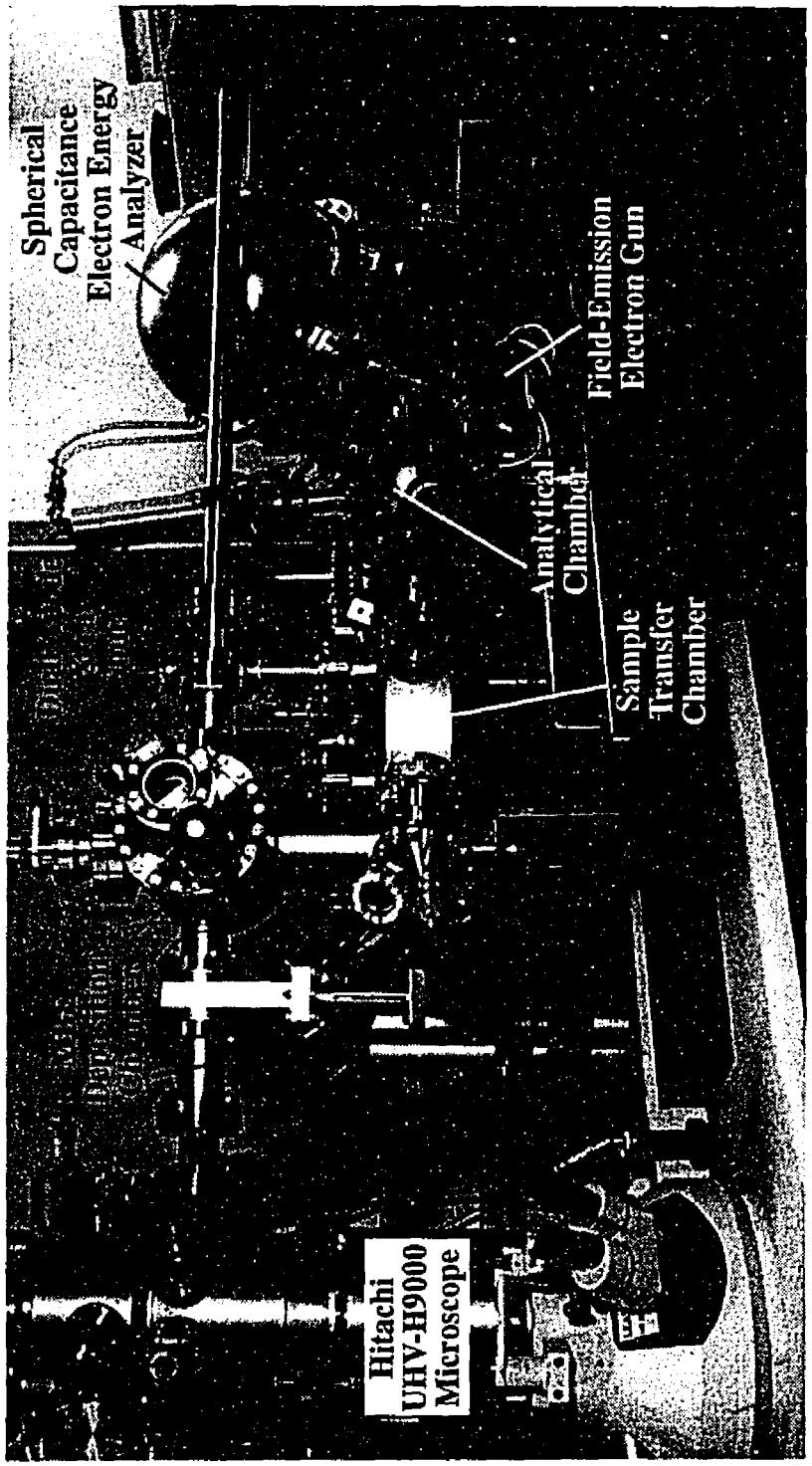

Figure 2.3. The current UHV-HREM facility comprising the UHV-H9000 microscope and the attached UHV-Sample Preparation, Evaluation, Analysis, and Reaction (SPEAR) chamber.

SPEAR. Sample transfer between the two sections is carried out via a vertical transfer rod which physically lifts the sample ring from the microscope cartridge or storage module and transfers it into the module or cartridge respectively; the module refers to a rectangular solid block with slots in which the molybdenum rings holding the specimens sit. The MBE chamber has four Knudsen cells, two of which are loaded with nuggets of gallium and arsenic respectively at the moment; resistive heating of the samples can also be carried out inside this chamber.

The analytical chamber is equipped to perform both clean surface preparation, and chemical and structural analyses of such surfaces. To enable this, a variety of instrumentation is mounted on this chamber:

1) A PHI-Electronics model # 06-660 differentially pumped Duoplasmatron Ion Gun for gentle removal of the surface contaminants using a variable energy (0.5-10 keV) beam of either oxygen, argon, or xenon ions. The gun is rated for a maximum extraction voltage of 10 kV with a minimum probe size of nearly 5μm and a maximum current density rated at 20 mA/cm^2 for a beam 50μm in diameter. Resistive heating of the sample holder is also possible in order to anneal out the defects/damage induced by the milling. Temperature during the anneal in either the MBE or the analytical chamber, is measured using a Mikron model # M190 Infrared Thermometer (range of 250-2000°C).

2) A FEI model # 13335 Thermal Field Emitter that can deliver up to 15 kV electrons at a current of 8 nA into a probe area, nearly 20nm in diameter on the sample. These electrons are then used to generate surface sensitive Auger and secondary electrons.

3) A PHI-Electronics model # 04-500 Dual Anode source for emitting either Mg or Al

K_α x-ray photons which generate electrons following interaction with the sample surface for XPS analyses.

4) A PHI-Electronics model # 10-360 Spherical Capacitor Energy Analyser with a multichannel detector to detect electrons that arise from the Auger and/or photoelectric process. The analyser has a maximum energy resolution of 0.1 eV and a minimum scanning area of 70μm x 70μm.

5) A Detector-Technology Inc. model # 1316E Channeltron secondary electron detector that detects secondary electrons produced due to interaction of either the electrons (emitted by the FEI gun) or the ion beam (generated by the Duoplasmatron gun) with the surface, and uses the secondary electrons to produce SEM images.

The advantages of the SPEAR over the original UHV-SSC are three-fold:

1) The superior surface spectroscopy and the additional SEM capabilities make it an ideal surface analysis facility, i.e., one that can completely characterize a solid surface in terms of what atoms are present, and where they sit.

2) Up to a total of eighteen samples can now be stored under vacuum at any given time in the three chambers.

3) There exist blanked-off ports on the transfer chamber, so extra surface science chambers can be added for other experiments, e.g., for sputter deposition.

2.5 Surface Preparation

The primary goal behind the design of the UHV-HREM facility is to prepare clean, well-ordered surfaces, which can be characterized completely in terms of the both the identity and geometrical arrangement of the surface species. This preparation is done in two stages, called *ex situ* or *in situ*, referring to the ones carried out external to or inside the facility. The objective of the first stage is to prepare a TEM grade specimen with electron transparent regions surrounding a hole in the center and also, with the least possible defect density. This criterion is crucial since it minimizes the time required to prepare a clean surface *in situ* thus enabling better usage of the microscopy capabilities of the facility.

2.5.1 *Ex Situ Preparation*

The *ex situ* stage used in preparation of the single crystal specimens of Si and GaAs in my graduate study was similar to that used in conventional TEM studies and usually commenced with ultrasonic cutting of bulk wafers into disks, 3mm in diameter. Since the thickness of these wafers is typically of the order of 0.5mm, the next step involved reducing this dimension, typically, to about 0.1-0.15mm. This was achieved by using diamond paste of varying grit sizes (9μm to 0.25μm). Either an uniform-width (~3mm) grinding wheel on the VCR dimpler stage, or mechanical hand-polishing (on abrasive cloth) was employed to provide the force required to enable the abrasive medium to perform effectively. When the dimpler stage was used, samples were mounted using

wax on to glass slides which were placed in a holder that could be rotated at adjustable speeds. The grinding wheel also rotated at adjustable speeds in the plane perpendicular to the sample, and a combination of these two motions and the abrasive paste resulted in thinning. Samples thus prepared were nearly uniformly thick across the lateral dimensions. Since a hole is required at the center, the samples were thinned using diamond abrasive pastes and dimpling wheels of appropriate dimensions, i.e., widths of 0.5-1mm, on the VCR dimpler stage. Depending on the final step of the process (described below), the dimpling process was carried out usually only on one side of the sample till the thickness at the center was roughly 0.04-0.07mm; the outer edges of the sample were still maintained at 0.1-0.15mm. To dismount the dimpled samples, the glass slides were heated to melt the wax; the samples were then slid off and washed in acetone to get rid of any wax residue.

Electron transparent regions in these samples were then achieved via the final step of either ion milling or chemical thinning. In case of the former, a greater thickness reduction at the center was the goal at the dimpling stage so as to minimize the milling time and therefore, the associated defect production. Samples were mounted on a liquid nitrogen cooled stage to minimize defect production and milling was performed in a Gatan Duo Ion mill using 4 keV Argon ions at 15° incidence. The main disadvantage with this technique is that it produces a high number of defects in the material despite the liquid nitrogen cooling; besides, for GaAs, preferential sputtering is a major concern. Chemical thinning, on the other hand, is advantageous not only from the point of view of lower defect density, but also because it produces relatively larger amounts of thin

areas, a point that I shall return to later. (Shallower dimples were used in samples that would be finally prepared by this route, since only a small thickness variation was required for preferential etch at the center.) In fact, the ion mill technique was used only to prepare the Si(001) sample used in the clean surface structure study, while the chemical thinning technique was adopted in preparing surfaces of both Si(001) and GaAs(001) for metal deposition study.

The dimpled samples were placed in the slot in a Teflon holder which was then held in a chemical bath. The etchant solution was constantly agitated using a magnetic stirrer and the etch process was monitored by noticing the changes in the specimen transparency to a light source. The composition of the etchant depended on the sample being thinned: a 10% HF + 90% HNO_3 solution was used for Si(001), while three different ones were used to etch GaAs. These included a 4% Bromine in Methanol solution, a combination of hydrofluoric, hydrochloric, and nitric acids with distilled water and finally, a 4:1:1 solution of sulfuric acid, hydrogen peroxide, and doubly distilled water. Solutions of these concentrations were used at the initial stages to provide the maximum etch rate, and as the thinning proceeded the samples were etched in solutions which were diluted to typically a half to a third of their original strength. The transfer was usually determined by the optical transparency of the central thin regions of the samples; in the case of Si it was the change in color from bright red to orange, and in GaAs it was the appearance of reddish regions at the center which initiated the step. Transfer into the solutions of lesser strength slowed the etch rate enabling detection of the very initial stages of the hole formation.

Although electron transparent central regions can be thus prepared, a major issue of concern with the chemical etch technique is hydrocarbon contamination that could arise due to a combination of improper handling, unclean hardware, and impure chemicals. Other sources of such contamination are back-streaming of the roughing pump oil, outgassing from the chamber walls, etc. The presence of hydrocarbons on the sample surface at this stage would necessitate some milling *in situ* since carbon does not desorb on heating in vacuum. Extreme care was therefore taken in handling specimens at the *ex situ* stage, and such electron transparent samples were taken out of the etchant and transferred either into purely distilled water, as in case of GaAs, or into a 9:1 distilled water - hydrofluoric acid solution in case of Si. The objective of this step was to minimize possible hydrocarbon contamination by building an oxide layer on the GaAs surface and a hydrogen layer on the Si surface, both of which desorb rather readily on heating. The samples were allowed to sit in these solutions for 10-15 minutes to enable sufficient build-up of these layers prior to loading into the microscope cartridge slot; a drop of the etchant solution, diluted to about a hundredth of its original strength, was put on the sample surface to further passivate it.

Ideal samples at this stage, when observed under the optical microscope showed extensive electron transparent regions surrounding the hole and pits away from the central hole. The pits arose due to the chemical etch process and resulted in production of greater amounts of thin regions (in comparison to ion milled samples) on annealing. This annealing stage and any other cleaning treatment, in order to achieve the final surfaces of desire, were carried out *in situ*.

2.5.2 *In Situ Preparation*

Despite the precautions taken in specimen handling, carbon is always present on the sample surface due to some combination of the sources mentioned above; removal of this and the other contaminants, and obtaining defect-free surfaces are the goals of *in situ* preparation. The GaAs(001) and clean Si(001) surfaces for surface structure and metal-deposition studies were prepared inside the UHV-SSC, while a "clean" GaAs(001) bulk surface for chemical characterization using XPS (and metal-deposition experiments), was recently prepared inside the SPEAR (unless specified, preparation was carried out in the UHV-SSC).

Surface preparation was conducted in two stages sequentially. The first step involved milling with 2-4 keV Argon ions at 30°-45° angle of incidence away from the surface normal, to either rid the surface of contaminants, prepare thin areas for TEM observation, or both; care was taken to avoid sputtering of the sample holder material on to the surface. Defects induced in the sample due to such high-energy, heavy ion milling were then annealed away by a 4-8 keV electron beam in the second step. These cycles were, typically, iterated many times before thin, relatively defect-free, reconstructed surfaces could be obtained. Metal deposition on to these clean surfaces was then carried out either inside the microscope or the UHV-SSC; prior to such depositions, the evaporator filaments were outgassed thoroughly to prevent carbon contamination.

The following chapter reports details on the clean Si(001) surfaces prepared using these techniques.

3. THE CLEAN Si(001) SURFACE STRUCTURE

3.1 Background

In the ideal (1x1) structure, each atom on the surface of Si(001) is two fold coordinated, bonding to two atoms in the underlying layer and thus has two dangling bonds. The high energy associated with these dangling bonds is lowered by the reconstruction of the surface atoms to a (2x1) type cell, using the Wood notation described in Chapter 1. The (2x1) structure was first observed by Schlier and Farnsworth in a LEED study[21,89] and since then many higher order reconstructions, e.g., the c(4x2)[90,91], c(4x4)[92,93], and various (2xn) structures[94,95], where $6 \leq n \leq 10$ have been reported. Considerable dispute surrounds the atom arrangement in the basic (2x1) surface cell; resolving this issue has been the subject of numerous theoretical and experimental studies (and was also the main motivation for this study).

Many alternative structures have been proposed to explain the locations of atoms in the surface cell, and the four main models are discussed here. A vacancy model in which half of the surface atoms are missing (Figure 3.1(a)) and a symmetric dimer model in which the surface atoms dimerize symmetrically (Figure 3.1(b)) were proposed by Schlier and Farnsworth[21,89]. A third alternative, termed the conjugate-chain model in which the surface atoms form zig-zag chains (Figure 3.1(c)), was also suggested[96], and later modified[97]. Finally, a variation of the symmetric dimer model, i.e., an asymmetric buckled-dimer structure was also proposed[98,99] (Figure 3.1(d)).

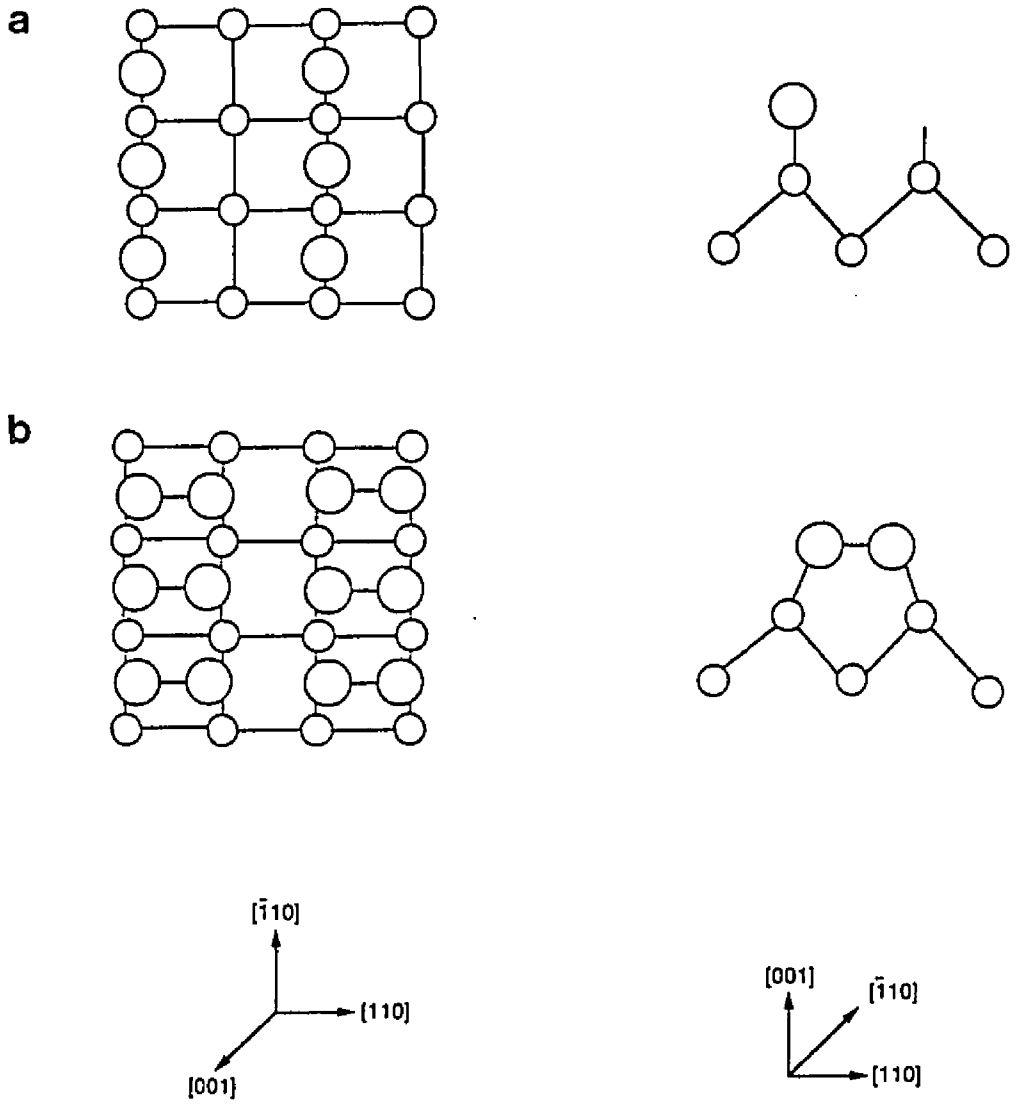

Figure 3.1.(a) Schematic of the vacancy model for the Si(001)-2x1 surface reconstruction. (b) Schematic of the symmetric dimer model for the Si(001)-2x1 surface reconstruction (adapted from LaFemina J. P. *Surf. Sci. Rep.* **1992,** *16,* 133).

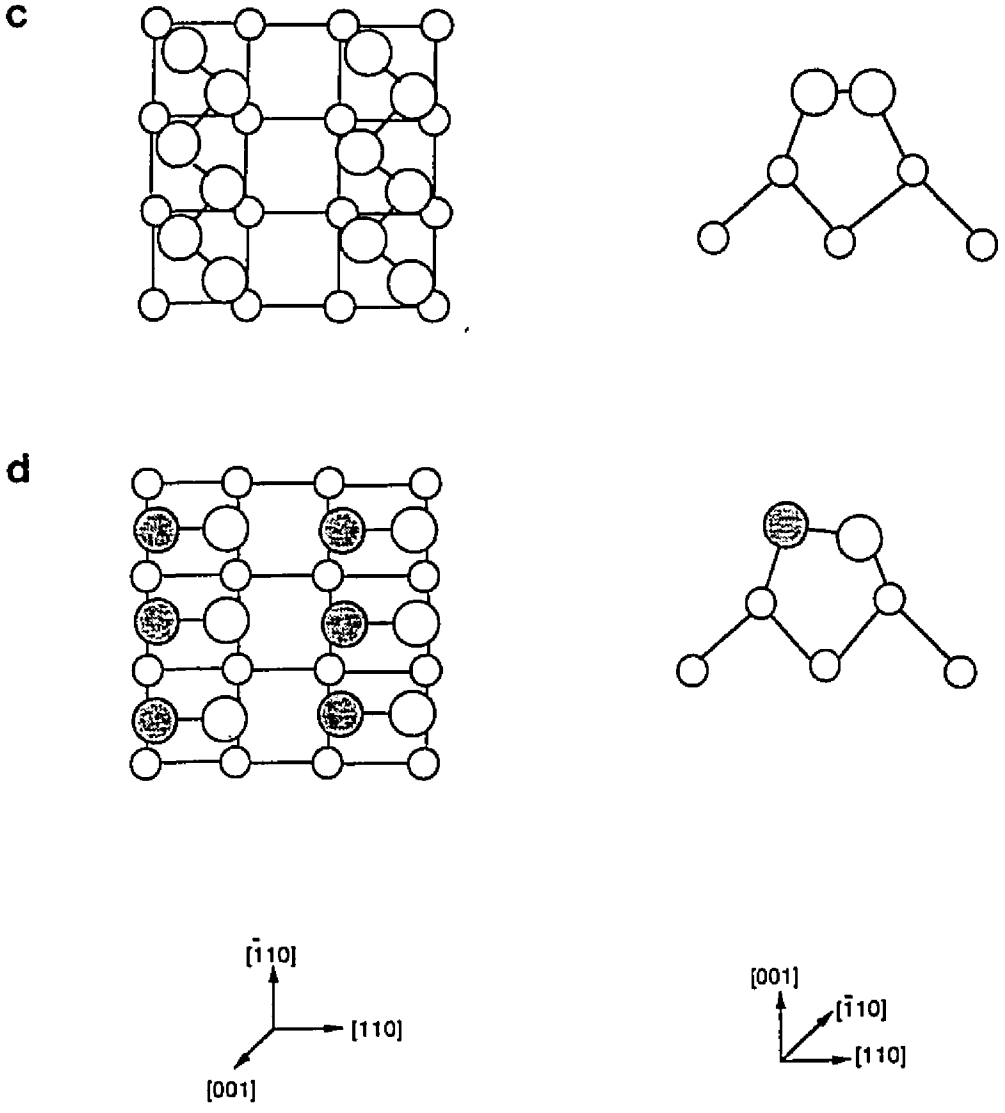

Figure 3.1. (c) Schematic of the conjugate chain model for the Si(001)-2x1 surface reconstruction. (d) Schematic of the asymmetric dimer model for the Si(001)-2x1 surface reconstruction; filled circles represent atoms buckled out of the surface plane (adapted from LaFemina J. P. *Surf. Sci. Rep.* **1992,** *16,* 133).

In the vacancy model, the reconstruction is established purely by eliminating half the surface atoms; there is, however, no reduction in the total number of dangling bonds, and such a structure would therefore be energetically unfavorable. The conjugate chain model is also unfavorable, since it involves significant motion of atoms on the surface, which is accompanied by a large local strain energy cost.

Photoemission studies[100,101], total energy calculations[98,99,102], and a kinematical LEED study[103] have all demonstrated a clear preference for the dimer models over the vacancy and conjugate-chain structures. The conjugate chain model[97] was reported to be favored over the dimer structure on the basis of better compatibility with LEED data, from an analysis which considered a two-layer reconstruction process. Using a simple Keating model to describe the subsurface elastic strain induced by surface dimerization, a kinematical LEED study[103] demonstrated that the penetration of the reconstruction was nearly five layers deep. Analysis performed using this deep-reconstructed symmetric-dimer model showed the structure to be compatible with LEED data; this conclusion was also supported by a quasi-dynamical LEED study[22], and ion scattering studies[104,105]. Early electronic structure computations[106,107] also showed a preference for the symmetric model (over the non-dimer ones), since this structure could best explain the photoemission data.

Empirical tight-binding calculations[98,99] first led to the proposal that the atoms involved in dimerization move unequal distances, both in and out of the surface plane, thus forming an asymmetric buckled structure. This was supported by other total energy minimization calculations[108,109], LEED studies[110-112], and more recently, by grazing incidence X-ray diffraction[113], and optical spectroscopy[114] studies. A variation of the

asymmetric buckled model incorporating twist was also suggested[110], although an equally good fit to the LEED data was demonstrated without invoking any dimer twisting[112]; total-energy computations also found such twisting to be energetically unfavorable[115,116].

Thus, while there is a general agreement that the dimer unit constitutes the basic building block of Si(001) reconstructed surfaces, the literature results are fairly inconclusive on the issue of dimer symmetry. One probable reason for the lack of agreement is that the energy difference between the two structures, i.e., 0.01-0.02 eV per atom[114-120], is actually comparable to the room temperature thermal energy suggesting that the dimers may fluctuate between the two configurations due to thermal excitations. This hypothesis was confirmed by real-space STM investigations.

The first STM studies[121,122] at room temperature indicated that only symmetric dimers were present on defect-free 2x1 surfaces. Buckled dimers were found in local regions with c(4x2) and p(2x2) symmetry near surface defects; the latter were thought to either induce or stabilize buckling in the adjacent dimers. A recent low temperature STM study[123] revealed, however, that on cooling the surface the number of buckled dimers increased at the expense of symmetric appearing dimers, and concluded therefore that the dimers must have an innate asymmetric structure which gets time averaged by room temperature thermal excitations to give a symmetric appearance (finite temperature molecular dynamics simulations[124] also support this suggestion). Recent surface stress[125] and total energy calculations[126], the latter at zero temperature, predict that these structures are actually more stable than either the symmetric or asymmetric (2x1) models.

Another compelling piece of evidence for the asymmetric model is provided by

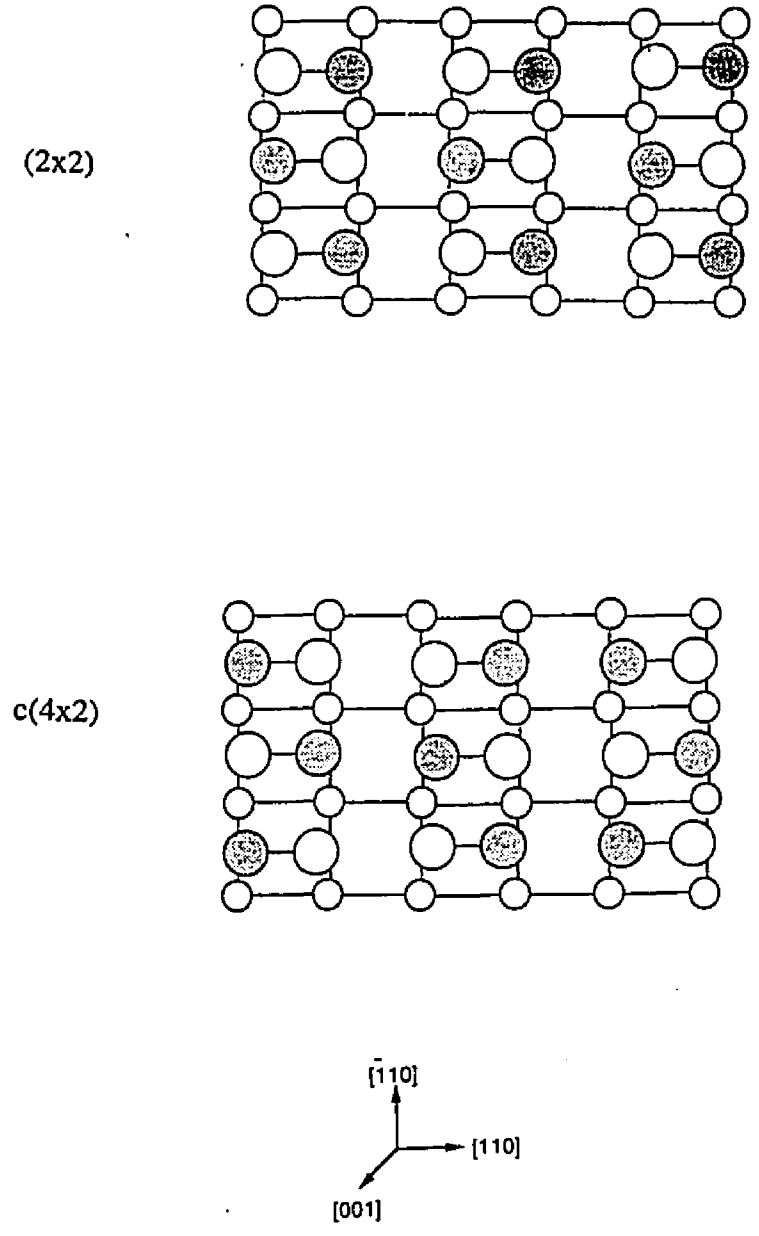

Figure 3.2. A schematic of the structure models for the 2x2 and c(4x2) reconstructions of the Si(001) surface; the filled circles represent atoms buckled out of the surface plane (adapted from LaFemina J. P. *Surf. Sci. Rep.* **1992**, *16*, 133).

the observation of the higher order structures by STM[121,122], and other earlier studies[90-93]; these structures are obtained by alternating the dimer tilting (Figure 3.2 shows the (2x2)and c(4x2) symmetries). Total-energy computations studying such higher-order reconstructions have concluded that the basic building block is asymmetric[98,99,102,116]. Energy differences between these higher order structures are also very small (3±13 meV[126]), highlighting the contribution of temperature as suggested above and thus explaining the multiple structures seen by STM[121,122].

3.2 Experimental Results

In the current study, irrespective of the *ex situ* route, i.e., ion milling or chemical thinning, clean surfaces of p-type Si(001) (B doped at 1 ohm-cm) wafers following *in situ* mill and anneal cycles were always characterized by the appearance of the 2x1 and 1x2 surface spots in TED patterns. These spots arise due to the rotation of the domain structure by 90° across each monolayer high step, i.e., orthogonal reconstruction domains. Figure 3.3(a) shows an experimental pattern, while Figure 3.3(b) is a schematic showing the reciprocal lattice corresponding to the two domains.

No additional spots corresponding to the higher order c(4x2) or p(2x2) structures were ever observed during the entire experiment. Prior to presenting details about the structure analyses, a few other points of interest about the surface need to be highlighted.

Consistent with the earlier STM report[122], a rather high density of steps and defects, i.e., stacking faults, was always found irrespective of the *ex situ* route. These

a

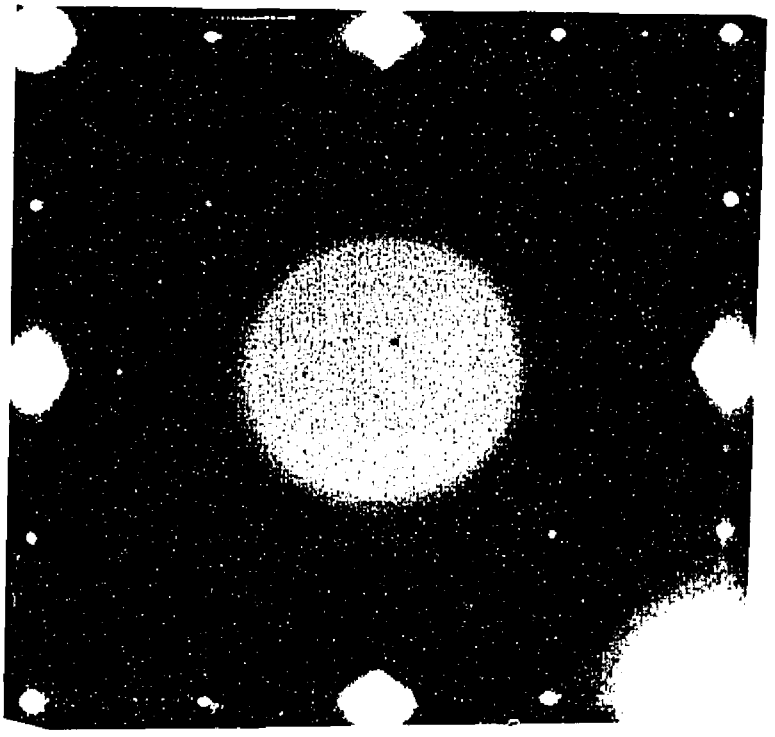

b

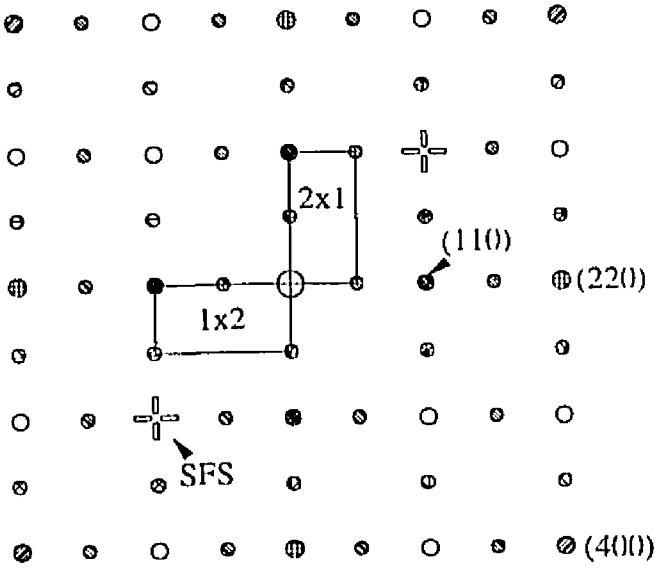

Figure 3.3.(a) A TED pattern obtained from a clean Si(001)-2x1 surface. (b) Schematic of the pattern in (a) showing the reciprocal unit mesh corresponding to the two orthogonal 2x1 domains in real space. SFS denotes the stacking fault streaks arising due to the finite size of stacking faults in the material (see text).

characteristics were revealed from both diffraction contrast images and also from the streaky nature of the (200) type spots along the <110> directions, in the off-zone axis pattern shown in Figure 3.3(a). The finite dimensions of these defects in real space give rise to rel-rods in diffraction space, whose intersection with the Ewald sphere result in streaks (labelled SFS in Figure 3.3(b)), depending on the diffraction conditions.

Although surface structure information on the atomic scale can be retrieved from both diffraction intensities and HREM images, the reconstruction dynamics of this system limited the retrieval to that from the TED patterns alone. As briefly mentioned in Chapter 2, one of the dominant species present in both the UHV-TEM and UHV-SSC is water vapor. Atomic hydrogen either native to the system or produced via splitting up of the water molecules under the electron beam, is reported to de-reconstruct the surface converting it back to a 1x1 structure[127,128]. The time available for the data collection was thus limited to 3-4 hours. This, in combination with the specimen drift as the sample cooled down to room temperature after the annealing treatment, precluded collection of HREM images of the clean surface.

Therefore, since the intensities of the surface spots in the TED patterns were the only available source of the atomic structure information, their values would have to be accurately measured[51,54]. One method of obtaining these values is by integrating the total intensity around each surface spot[54]. This technique however suffers from two main disadvantages: it is no longer accurate when the diffuse scattering in the TED patterns cannot be properly modelled and subtracted, and the low signal to noise levels of the surface spots also make the measurement difficult, since the intensity levels are on the

order of 10^{-4} of the incident beam or smaller. Instead, a cross-correlation technique which has been successfully used in quantitative analysis of transmission electron microscopy images[129,130] was used to measure the individual surface diffraction intensities in this case.

3.3 Data Analysis

3.3.1 *The Cross-Correlation Technique of Intensity Measurement*

The basic approach was to fit each surface spot with a motif and thereby extract the peak intensity value; the method was found to be robust for weak spots with a strong diffuse background. TED patterns were recorded on negatives with a series of exposures from 4 seconds to 60 seconds to cover the large dynamic range of the surface as well as bulk spots (intensity values of weak spots were evaluated from a long exposure negative, the strong spots from a short exposure, and a range of intensity of at least three orders of magnitude was thus obtained). The negatives were digitized to 8-bit using an Optronics P-1000 microdensitometer. The digitized intensity was calibrated against the electron dosage on the negative using a Faraday Cup in the microscope, and a linear relationship, with one count equivalent to 14 electrons was obtained.

The digitized patterns were processed using SEMPER software. To build a motif image for cross-correlation, a number of diffraction spots (eight in this case), such as those marked "M" in Figure 3.4(a), with relatively strong intensity and low background

were selected. They were cross-correlated, averaged, and normalized to form the final motif which had a total integrated intensity of unity. The motif image was then correlated locally with the spot of interest (either surface or bulk), and the matching value was taken as the intensity of that spot. Figure 3.4(b) demonstrates the success of this fitting method, where a 1x1 type spot, labelled A, was removed by subtracting the matched peaks from the original (Figure 3.4(a)) leaving the background unperturbed. This is also shown clearly in the line scans of Figure 3.5.

To determine the accuracy of the technique, the following test case was constructed: a Gaussian peak containing noise with a Poisson distribution was cross-correlated with a standard Gaussian (no noise), and the intensity value was obtained. This process was repeated several hundred times to establish a statistical distribution. The square of the standard deviation was found to be linear with the peak intensity, with a proportionality constant of 0.025. (Tests done with peak shapes other than a Gaussian, for example a Lorentzian, showed the same relationship.) The significance of this result will be discussed later.

Experimental intensities of both the bulk and surface spots were determined using this approach. The intensities of the bulk spots were used in evaluating the sample tilt and thickness using an initial estimate of the tilt from the Kikuchi lines in the TED patterns (the minimization procedure detailed in the next section was followed). Two sets of surface spots' data, one from each domain of the reconstruction, were obtained from

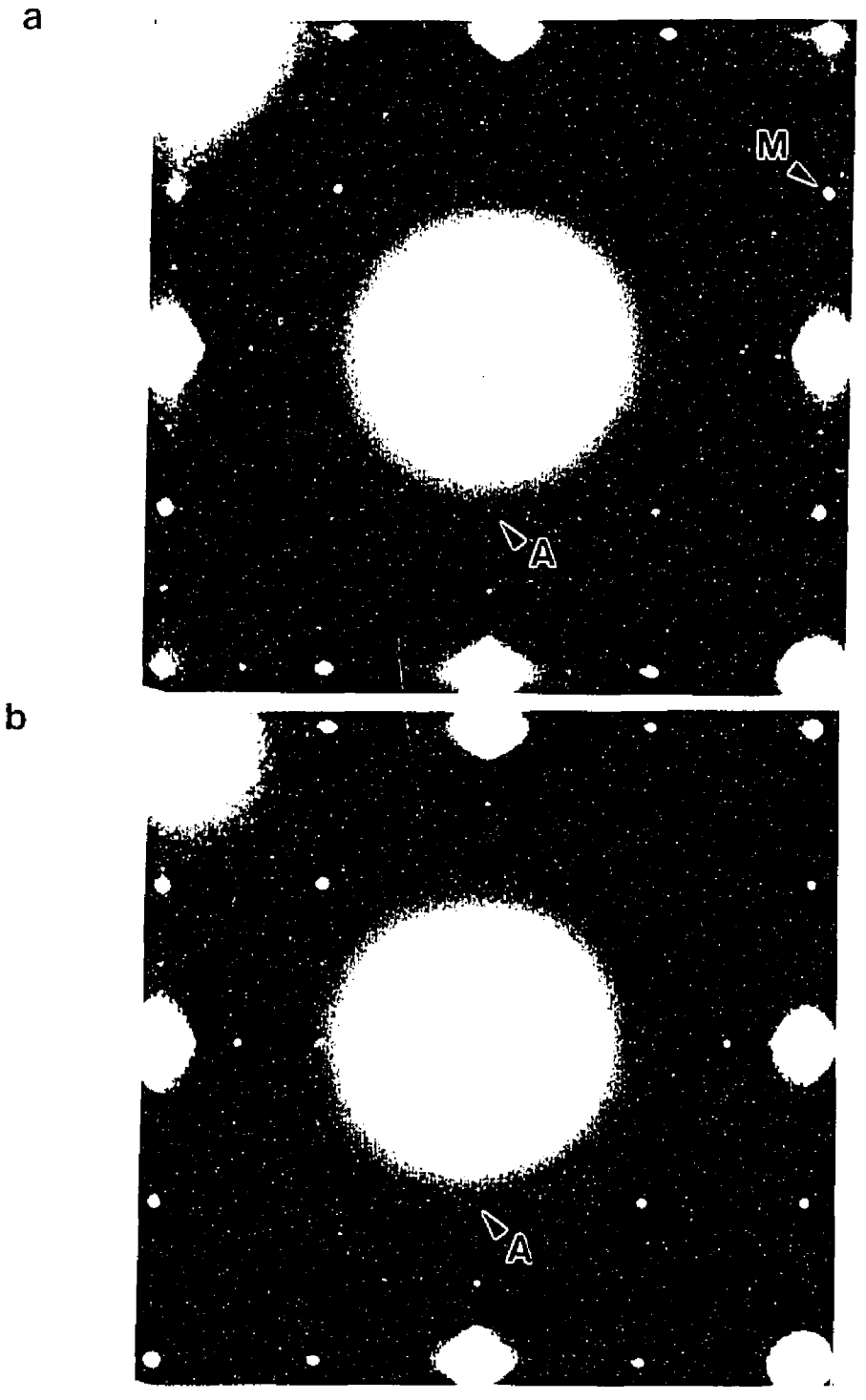

Figure 3.4.(a) The TED pattern of the clean surface in Figure 3.3, with the spot **M** denoting the motif spot and a 1x1 spot marked **A** for reference. (b) The spot marked **A** in (a) was removed using the cross-correlation technique (see text), leaving the background undisturbed.

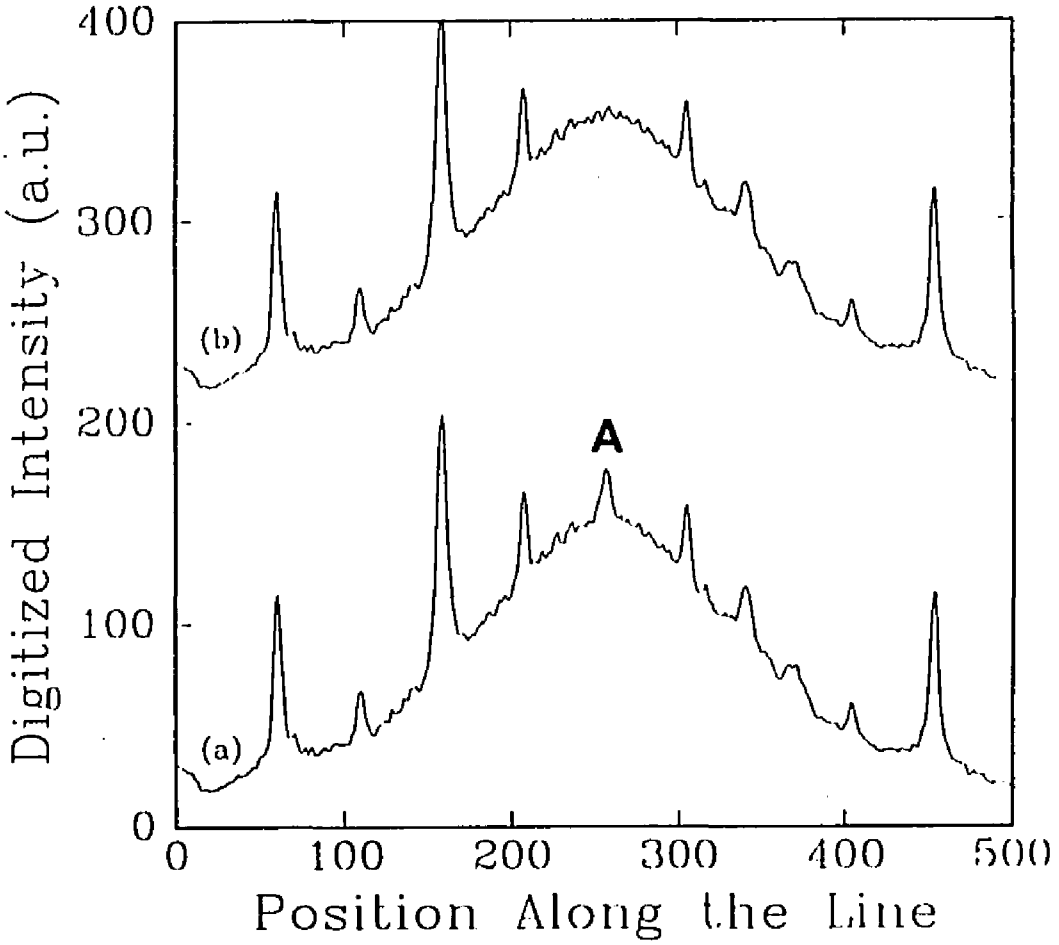

Figure 3.5. Line scans from Figures 3.4.(a) and (b) showing the clean removal of the spot marked "A".

each pattern. Typically, each set contained 50-100 independent beams and the patterns were collected for samples under two different tilt conditions of 54mrad and 83mrad; the sample thickness in the corresponding cases were 13.5nm and 45.6nm.

3.3.2 *Analysis Using Experimental Intensities*

The basic framework of the analysis was as follows: corresponding theoretical intensity values of these spots were estimated for a starting input structure of the surface (and bulk), using both a simple kinematical diffraction and a rigorous, double precision dynamical multislice approach. The input structure was optimized numerically in this process to yield the best fit between the experimental and calculated data. These minimizations[131] included two forms of reliability factors (R-factors) and reduced χ^2 fittings, and were performed using the routine NL2SOL from Netlib[132]. The R-factors and χ^2 are defined as follows:

$$R^n = (\Sigma\ |I_e(u) - I_c(u)|^n\ )/\ \Sigma I_e^n(u) \qquad (3.1)$$

$$\chi^n = \Sigma\ (\ |I_e(u) - I_c(u)\ |^n / \sigma^n(u)\ )*\ 1/(N-M) \qquad (3.2)$$

where $I_e(u)$ and $I_c(u)$ are the experimental and calculated intensities, and $\sigma(u)$ the standard deviation of the error distribution for each diffracted beam u. N is the number of diffraction beams and M the number of parameters that are varied. n=2 defines a standard form, while n=1 defines a more robust version. The R-factor (or reliability factor) defines

the error between the intensities generated for the input structure model and the corresponding experimental values and thus provdies a measure of the goodness of the fit; χ on the other hand estimates the confidence level of the final result of such a structure determination. It therefore follows that values close to 0 and 1 for the R-factor and χ^2 respectively are desirable in such quantitative analyses.

In the initial stages of the minimization, atoms on the surface and a few layers beneath it were allowed to freely vary (i.e., no constraints) from their ideal bulk positions along the "2" direction of the reconstruction (y axis in the calculations). Intensities were calculated for the resultant structures used a simple kinematical diffraction approach[51,52]; however, such minimizations yielded physically unrealistic atom positions. Besides their simplicity, the advantage of using such an approach is that the calculations save computer time. However, this approach suffers from many disadvantages as shown in Chapter 2 and has also been documented to be inadequate[133]. Minimizations of the experimental intensities against ones calculated from a dynamical approach yielded an asymmetric structure; however, χ^2 values (< 1) indicated an overfit of data.

Since the surface dimerization process is reportedly accompanied by substantial sub-surface strain[103], a strain field with the correct periodic structure for the reconstructed surface was applied to constrain the atom positions to obey the equations of inhomogeneous, isotropic elasticity[131]. This displacement/strain field has a periodic character in the x-y plane, and is of the form:

$$\mathbf{D(r)} = A\underline{\nabla}([z + \alpha|\omega) + B\underline{\nabla}\omega + C\underline{\nabla}\times(\underline{n}\omega) \qquad (3.3)$$

where ω is a harmonic function, $\underline{n}$ the unit vector, α (= 2(2-υ), υ is the Poisson's ratio) is a constant and A, B, C are variables. Defining x and y in terms of the unit cell, an appropriate form for ω is:

$$\omega = \exp(-2\pi q_z z)\exp(-2\pi i[q_x x + q_y y]) \qquad (3.4)$$

with $q_z^2 = q_x^2 + q_y^2$, where q_x and q_y are integers representing the Fourier periodicity of the reconstruction.

This form has enough generality to model any sub-surface distortions and has the correct physical form of decaying into the bulk of the material (while boundary effects may change the strain field for extremely thin materials, e.g., 2-4nm, they are not a problem for the thicknesses used here). The first two terms in equation 3.3 are associated with a longitudinal wave while the third term represents a shear wave; the latter is used only to model twist. Rather than varying the atom positions, A, B and q_y ($1 \leq q_y \leq 3$ in most calculations, $q_x = 0$) were varied (i.e., vary the strain field), with an appropriate choice of sine and cosine terms to enforce symmetry requirements if necessary.

The atomic positions in the symmetric and asymmetric dimer models proposed by Roberts and Needs[109] were used as the starting point of the minimization. Reconstructions were assumed to exist on both the top and bottom surfaces, and a linear incoherent combination of the two was used. Minimizations were performed using both domains of the reconstructions and multislice calculations were carried out for each, since the orientation with respect to the specimen tilt was different. Also, since intensities are

sensitive to the asymmetry direction, minimizations were carried out for both and an average value used. It should be noted that the absolute intensities correlated to approximately a monolayer coverage (of reconstruction) on both surfaces.

Initially, a four layer relaxation was assumed. The Debye Waller (DW) terms, which model the thermal diffuse scattering process, were used as variables for each of these layers since anisotropic mean square displacements have been reported[134]. However, the visual fits for higher order reflections were poor and the minimized DW values were physically unreasonable, i.e., much too small. Since intensities at larger reciprocal lattice vectors are very sensitive to both the strain field and the DW term, an incorrectly defined strain field can be compensated by unrealistic DW values. When eight layers were allowed to relax instead, good visual fits for higher order reflections were obtained and the DW terms minimized to physically realistic values. For such a relaxation model (i.e., eight layers), the minimizations were only weakly sensitive to variations in DW terms and therefore, fixed anisotropic DW values were used.

3.4 **Structure Model**

The final surface structure obtained from this analysis was clearly asymmetric within both the scatter bars between different minimizations, and error bars for each minimization. Table I lists the average atom positions obtained from the different procedures (corresponding to the different values of "n" in equations 3.1 and 3.2), at a 90% confidence level, with the associated error bars and maximum scatter

Table I

Atom positions for the asymmetric 2x1 structure as fractions of cell parameters, A = 0.383nm, B = 0.767nm, C = 0.543nm. Error bars for only the y positions are reported since z positions are measured only indirectly, while the x positions were not varied in the minimizations. Scatter values for the y and z positions are reported to give an idea about the reliability of the structure.

	x	y(scatter, error)	z(scatter)
Layer 1	0.500	0.332 (3E-03, 5E-03)	-0.024 (0.003)
	0.500	0.616 (2E-03, 5E-03)	0.024 (0.003)
Layer 2	0.000	0.225 (3E-03, 2E-03)	0.232 (0.002)
	0.000	0.698 (3E-03, 2E-03)	0.268 (0.003)
Layer 3	0.000	0.007 (7E-03, 3E-04)	0.569 (0.06)
	0.000	0.498 (6E-03, 4E-04)	0.431 (0.05)
Layer 4	0.500	0.001 (5E-04, 1E-04)	0.770 (0.02)
	0.500	0.499 (5E-04, 1E-04)	0.730 (0.02)
Layer 5	0.500	0.254 (2E-03, 1E-05)	0.9995 (1E-04)
	0.500	0.746 (2E-03, 1E-05)	1.0005 (1E-04)
Layer 6	0.000	0.251 (2E-03, 1E-05)	1.2499 (1E-04)
	0.000	0.749 (1E-03, 1E-05)	1.2501 (4E-05)

values for an eight layer relaxation model. Atom displacements in the seventh and eighth layers are not listed since they are very small in magnitude, i.e., ~ $5x10^{-6}$ nm. This structure is shown schematically both in side and top views in Figures 3.6 and 3.7 respectively.

3.5 Discussion

R-factors and χ^2 values (both standard and robust versions) for this structure were in the range of 0.10-0.12 and 1.08-1.5 respectively for the two diffraction cases, signifying excellent reliability of the structure. (These values of χ^2 also reflect on the accuracy of the estimate of the standard deviation parameter, i.e., the error estimate, for the intensity measurements.) The lower R-factors and χ^2 were obtained for the set with a larger number of beams, also a much better data set. The surface dimer bond is inclined out of the surface at an angle of 5°37′ and the bond length of 0.22nm is in excellent agreement with the asymmetric structures proposed by Yin and Cohen[108] as well as by Roberts and Needs[109] (referred to as YC and RN structures respectively).

In contrast to these and the other models in literature, atoms in the second layer of the model from this study do not move towards each other (although the intralayer bond length is identical to that reported for the RN and YC structures). The plausibility of this structure, i.e., low scatter and error bars, is attributed to the high sensitivity of the TED process to atomic displacements parallel to the surface. The dimer backbond lengths of 0.24-0.25nm lie in between the values for the RN (0.23nm) and YC (0.25-0.28nm)

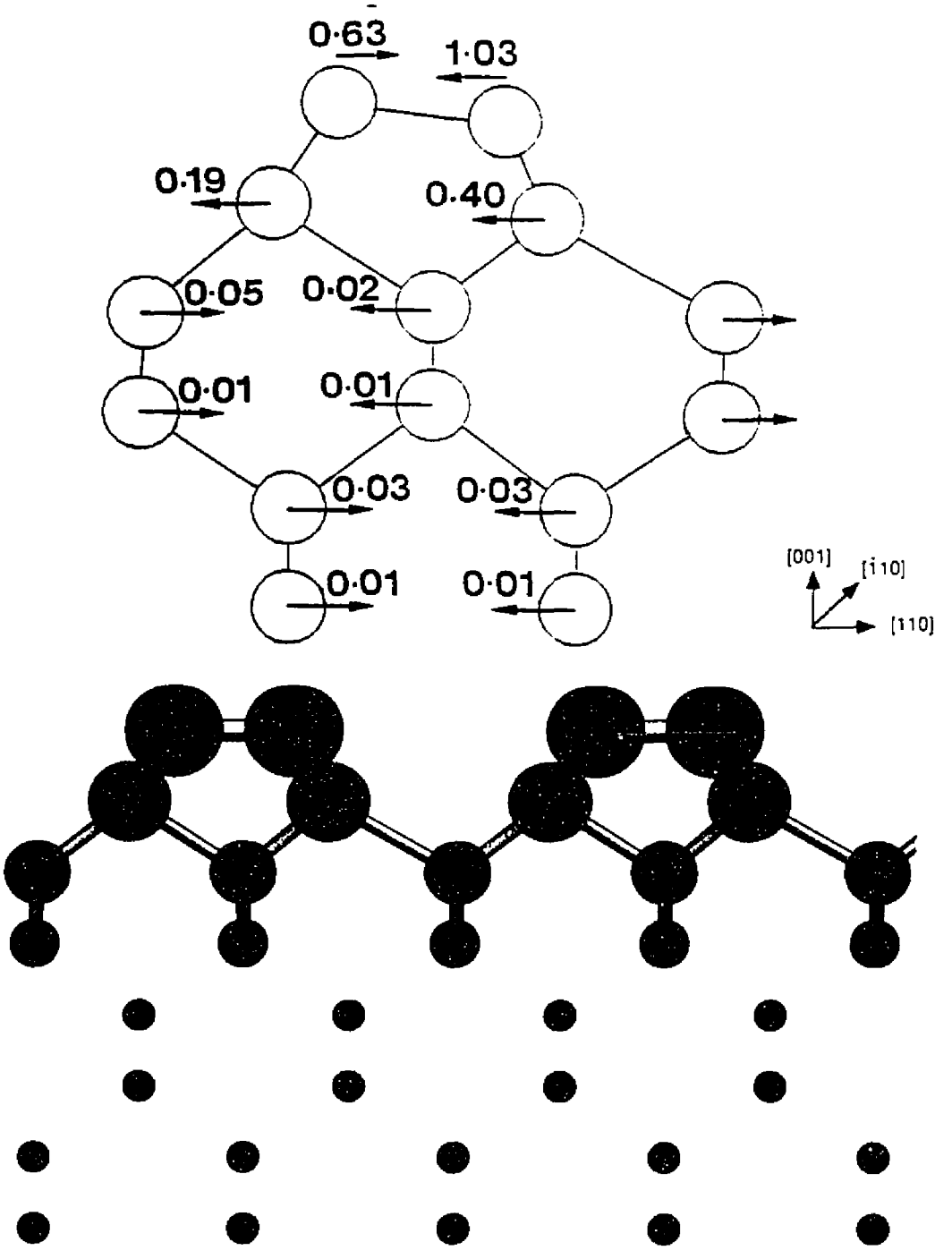

Figure 3.6. A side-view schematic of the Si(001)-2x1 structure model from the study, for a six layer relaxation model; the dimer bond lies in the plane of the paper. Arrows and numbers denote the direction and magnitude (in Å), of surface atom displacement away from the bulk locations in the dimerization process.

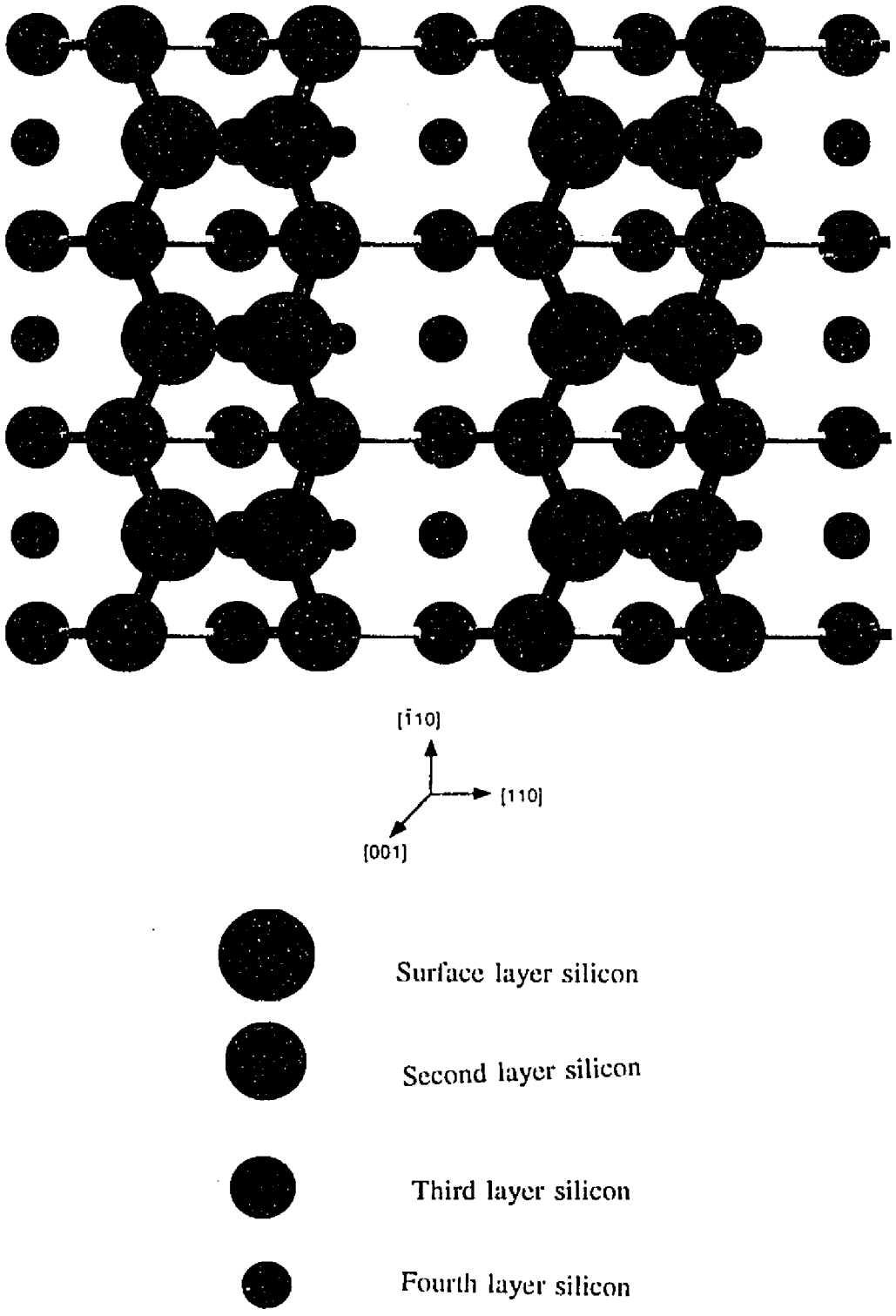

Figure 3.7. A top-view schematic of the surface structure shown in Figure 3.6.

structures. While atom displacements extending into the fourth layer are asymmetric, scatter in the atom positions for the third layer make it impossible to resolve the fine details of the structure of this layer. Atoms in all other subsequent layers in the unit cell move towards each other, with small displacements noticeable up to the sixth layer. In general, for the first four layers, this structure is in better agreement with the YC structure than the RN model.

Although the absolute atom displacements are small beyond the third layer, a strain field still needs to be modelled for at least an eight layer relaxation to obtain a good fit. Since TED is relatively insensitive to displacements along the beam direction (z), high error and scatter bars are associated with the Δz values, especially below the second layer. (It was possible to constrain the Δz values by increasing the number of q_y variables and still obtain the same Δy displacements.) The possibility of an asymmetric structure with twist[108] was explored by including the shear term in equation 3.3; however, structures with large scatter in the x values (0.1-0.2nm) and error bars were obtained.

When a constraint was imposed in the calculations to yield a symmetric structure, although the R-factors were higher only by 0.02, χ^2 values were 1.6-2.0, (in the two diffraction cases) signifying high errors in the fit. Table II gives a quantitative comparison for the asymmetric (simple tilt) and symmetric structures obtained in this work, using the better data set. A similar behavior, albeit, with higher values for these parameters were obtained using the other set.

Large enough step sizes were used in the calculations to avoid local minima. It

Table II

Summary of standard R-factors and χ^2 values for models calculated for the better data set show the conclusive preference for the simple asymmetric structure (i.e. no twist).

	4 layer relaxation	8 layer relaxation	Forced Symmetry
Structure Obtained	Asymmetric	Asymmetric	Symmetric
Standard R-factor	0.1158	0.113	0.133
χ^2	1.32	1.08	1.61
Visual Fit	Poor	Best	N.A

should be mentioned here that with the strain field minimized from rigorous dynamical calculations as the starting point, minimizations run in conjunction with pseudo-kinematical diffraction calculations yielded an asymmetric structure with identical atom positions. Also, both pseudo-kinematical and dynamical diffraction calculations run with free atom variability calculations on this structure minimized to exactly the same positions. Larger unit cell calculations carried out using atom positions in the c(4x2) and p(2x2) structures also yielded the asymmetric 2x1 model. This structure thus appears to be a minimum for all the methods.

Beside the structure model, this investigation revealed two other points of interest for quantitative diffraction analysis:

a) The limitations of the kinematical diffraction approach were exposed, even under the off-zone axis conditions (in the two diffraction cases here); in fact, such calculations can be used only to check the reliability of the structure pre-determined from a rigorous dynamical analysis.

b) While the structure obtained from fitting a large set (~100-200 beams/pattern) is statistically highly probable, overfitting the data by increasing the number of variable parameters (e.g., the twist case) in the minimizations should be avoided.

A final comment on the structure model: although an asymmetric structure is predicted, due to the inherent insensitivity of the calculations to the DW terms it is impossible to hypothesize on the validity of the dynamically fluctuating model suggested by STM[123].

4. METAL-Si(001) SYSTEMS

4.1 Introduction

Once the structure of a clean semiconductor surface is known, the behavior of metal deposits on these surfaces, both at room temperature and on annealing, needs to be understood since it has important ramifications in contact technology. For example, the presence of an oxide layer or alloy reportedly affects the contact resistance of the devices[135], while studies of high quality metal-semiconductor (MS) interfaces reveal that electrical properties such as the Schottky barrier height (SBH) depend strongly on the structure of the interface[136-138]. These two issues, i.e., the chemical and structure characteristics of the interface, are the focal points of interest in studies of MS interfaces.

The final structure of the interface depends strongly on the film nucleation and growth in the initial stages, which proceeds via one of the following three routes: two dimensional (2D) layer by layer or Frank-van der Merwe, three-dimensional (3D) islands or Volmer-Weber (VW), or a combination of the two, i.e., 2D layer plus 3D island, or Stranski-Krastanov (SK). A schematic of these modes is shown in Figure 4.1. In the latter two cases, further growth of the three-dimensional islands occurs by enlargement of pre-existing nuclei and/or coalescence of neighboring islands. During these processes, the islands can either retain their original structures or undergo recrystallization to form new structures. Therefore, an understanding of the initial structure and its evolution as a function of increased coverage (resulting in the final film) is highly desirable.

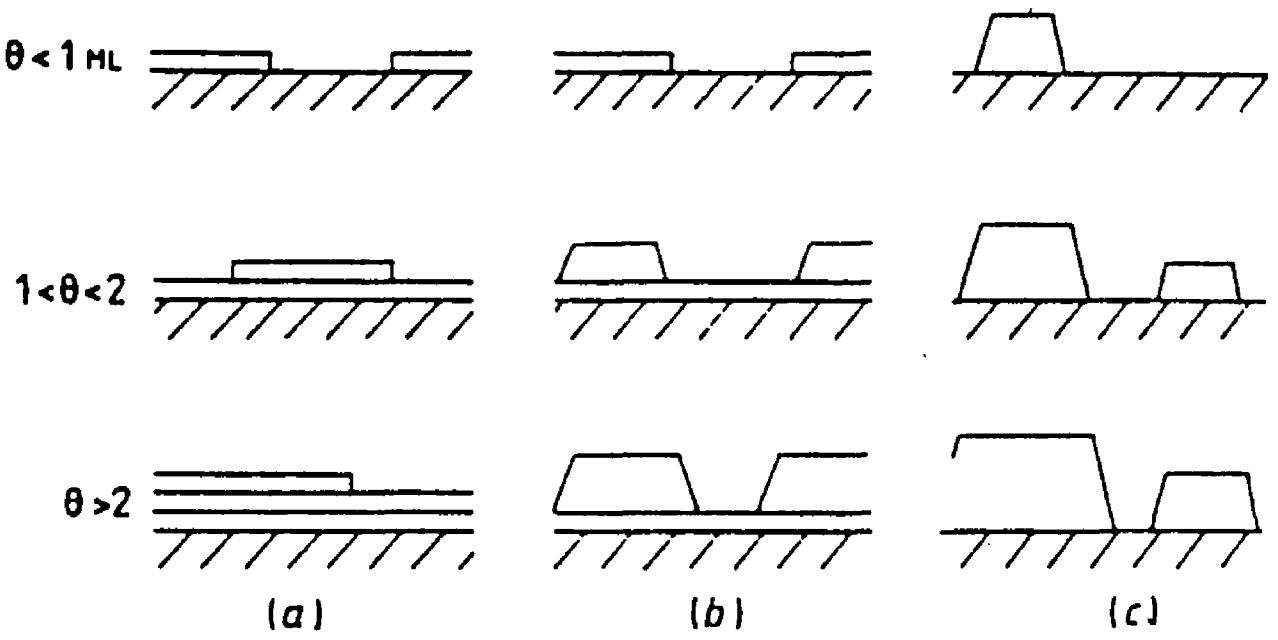

Figure 4.1. A schematic of the different modes of thin film nucleation and growth (after Venables, J. A.; Spiller, G. D. T.; Hanbücken, M. *Rep. Prog. Phys.* **1984,** *47,* 399) : (a) 2D layer by layer or Frank van der Merwe mode, (b) 2D layer plus 3D islands or Stranski-Krastanov mode and (c) 3D islands or Volmer-Weber mode. θ represents the coverage in monolayers (ML) for a hypothetical system.

The chemistry of a specific MS interface depends on the coverage of the metal layer and the temperature during or following deposition. The behavior of Ag and Au on clean Si(001) surfaces can be used as examples in this regard due to the differing chemical characteristics of the two interfaces (a SK growth mode is reported for both systems at room temperature, see the sections below). At room temperature, the Ag/Si(001) interface is atomically abrupt[139,140] (and thus constitutes an ideal system for study of SBH as a function of interfacial microstructure[138]), while the Au/Si(001) interface is mixed with the alloying mechanism reportedly proceeding only above a certain critical thickness[141-144].

The evolution of the MS systems, both structurally and chemically as a function of annealing (aside from coverage) is also important since some form of contact annealing or sintering is commonly used to reduce contact resistance to acceptable levels; in the case of the Au-Si(001) system, such annealing yields a variety of surface reconstructions[145-149].

Considering the rather disparate behavior of these two systems therefore, the room temperature behavior of Ag/Si(001) and annealing characteristics of Au/Si(001) surfaces were chosen as subjects for study; the more specific motivations in the two cases are presented in their respective sections.

4.2 Ag-Si(001)

4.2.1 *Background*

Since the issue of interfacial chemistry is well-established[139,140], i.e., atomically abrupt, studies mainly focus on the structural characteristics of the interface. The latter involve, for example, understanding both the growth mode and the orientation of the Ag layer (with respect to the underlying Si(001) substrate).

The nucleation and growth mode of Ag films on clean Si(001) surfaces at room temperature, both at the initial stages and for thicker films, has been characterized as being some combination of a 2D layer and 3D islands. The SK growth mode has been observed from STM[139,150-154], LEED-AES[155-159], surface reflectance spectroscopy-AES[160], and RHEED[140,161] investigations; on the other hand, 3D nucleation prior to completion of the 2D layer, which is termed a pseudo-SK mode, has also been reported in a recent STM study[162]. There also exists some controversy with regards to the saturation coverage (0.27 ML[152], 0.5 ML[150], 1 ML[154], and 1.5 ML[161]), and orientation relationship (<100>[155], <110>[150], and <111>[140,150,152,156] of Ag normal to the Si(001) surface reported), of the 2D Ag layer that forms in these cases.

Despite these investigations, surprisingly little is known about the structure of the 3D islands that grow atop the 2D layer. The external morphology is assumed to be flat with mostly {111} and {100} facets[152,159-161], and only two studies[163,164] even allude to the internal structure within the islands. In fact, most studies assume a simple single crystal structure.

It was this specific aspect of the interface that was chosen for study, i.e., an attempt was made to characterize the structure of the 3D islands in this system.

4.2.2 *Experimental Results*

TED Data

TED patterns collected following Ag deposition on to the clean surface showed features consistent with earlier diffraction studies[140,155,156], i.e., a decrease in the intensity of the Si surface reconstruction spots with increasing Ag coverage. Faint arcs whose spacings correspond to those of bulk Ag were also observed from the initial stages, suggesting the abruptness of the interface. One such pattern reproduced in Figure 4.2 shows the coexistence of the 2x1 spots of the clean substrate, and the (111) and (220) arcs of Ag. (With increasing deposition, an increase in the intensities of these arcs along with the disappearance of the one-half order spots, leaving behind a 1x1 surface, was observed; a true polycrystalline ring pattern developed at higher coverages[155].)

These arcs can be indexed in terms of a primary <110> epitaxy, i.e., normal to the surface, with some rotational disorder and strain, moiré fringes between the particles and substrate, and moiré fringes internal to the particles themselves[165,166]. The actual origin will be clarified later, but for the moment it should be noted that the TED patterns are actually highly misleading. Rather than carrying out such hypotheses about the structure of the film based solely on TED data, HREM images were analyzed.

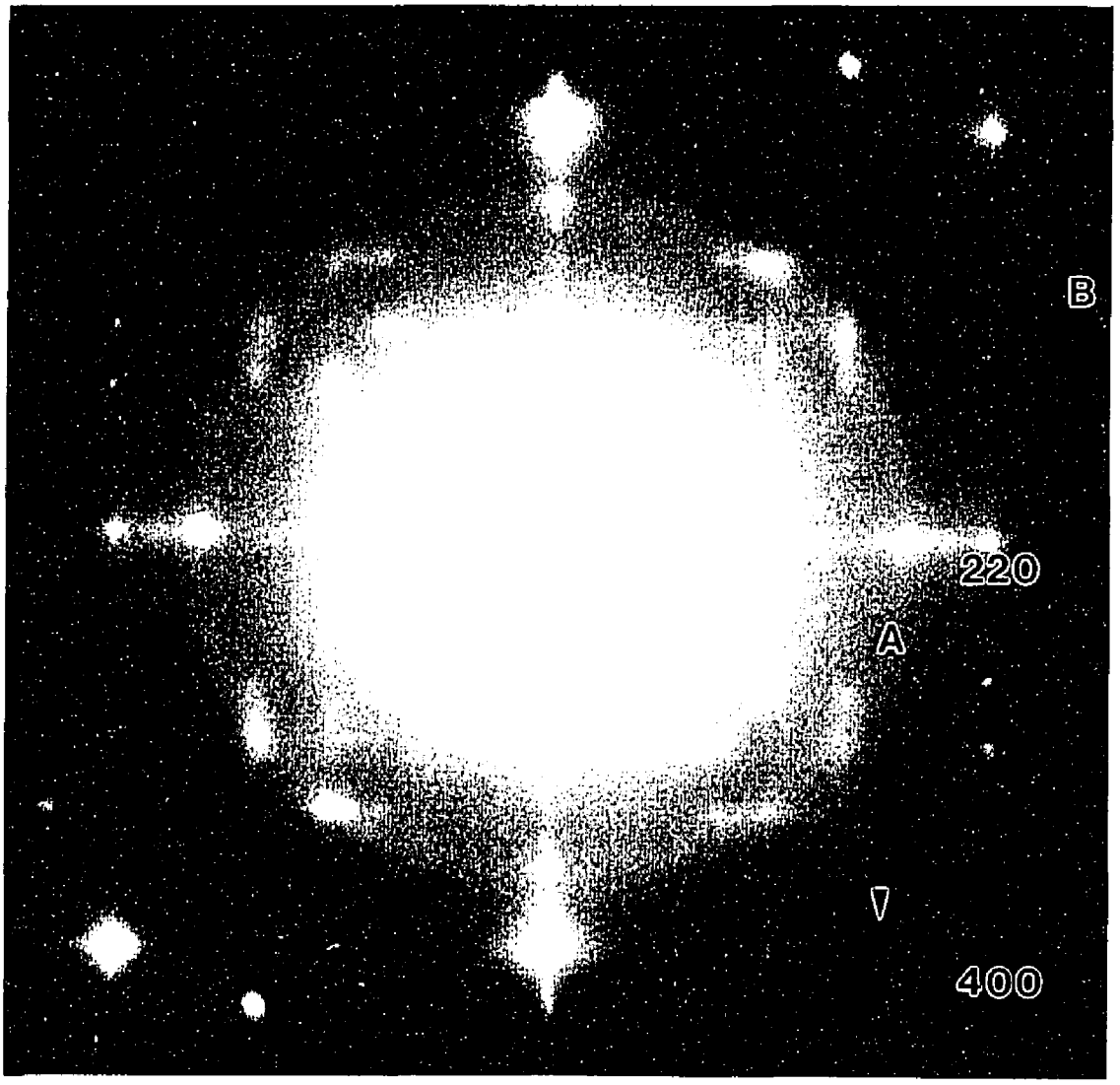

Figure 4.2. A typical TED pattern recorded following Ag-deposition on to Si(001)-2x1 surfaces at room temperature. A and B denote the (111) and (220) arcs of the Ag deposit respectively and a substrate reconstruction spot is arrowed.

HREM Imaging Data

HREM images were acquired in both the on- and off-zone axis modes. Aside from the dark contrast features of Ag with extensive moiré fringes, the on-zone axis images were difficult to interpret, in terms of providing information about the actual structure of the deposit layer; this arose due to the strong contribution of the underlying bulk signal. A typical on-zone image is shown in Figure 4.3. Reduction of the bulk signal resulting in a relative increase in sensitivity to these surface features was obtained by tilting the sample 2-3° off the (001) zone (analogous to the approach used in the clean surface study detailed in the earlier chapter). The contrast of all the images was further enhanced by the application of a Wiener-filter[167], which removed the shot noise without introducing any artifacts.

Such noise-filtered, off-zone images revealed the dark features (seen in the on-zone images) to be 3D Ag islands; one such image is shown in Figure 4.4. These islands had rather complicated structures, which were analyzed using SEMPER software and a data reduction scheme developed by Doraiswamy and Marks[168]. The next section details the results from such an analysis.

4.2.3 *Data Analysis*

Particles averaged 3 to 5nm in size; analyses revealed that about half of them were single crystals (Sc) and the rest were internally twinned structures (twinned between the adjoining (111) faces). These twinned structures form part of the family of multiply

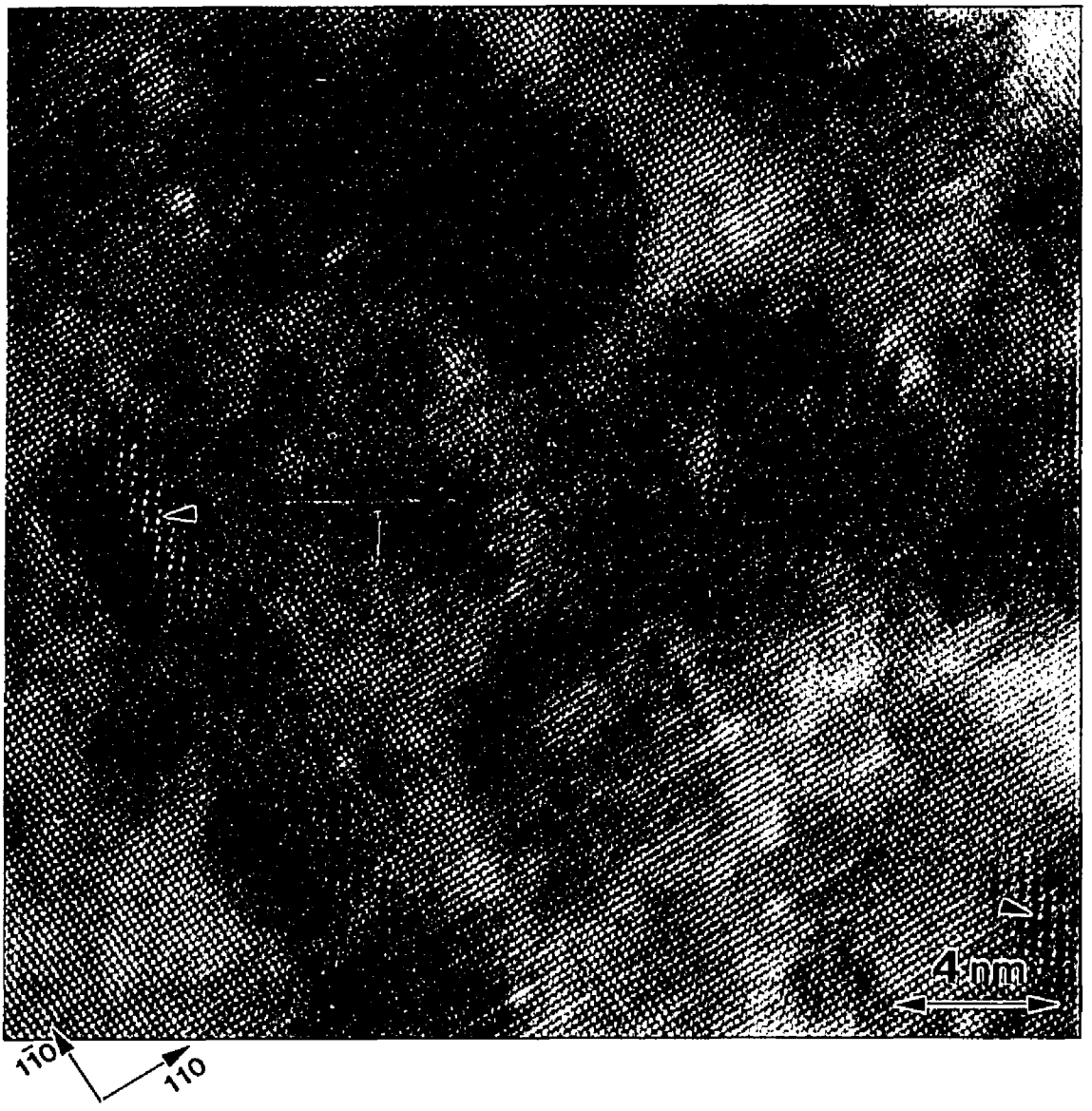

Figure 4.3. An on-zone image of Ag deposits on a Si(001)-2x1 surface at room temperature. The (220) fringes of the substrate and the moiré fringes in the features (arrowed) are apparent.

Figure 4.4. An off-zone image of the Ag-Si(001)-2x1 interface. The features with the moiré fringes in Figure 4.3 are resolved to be three-dimensional islands of Ag.

twinned particles (MTP's) reported first by Ino[165] for Au deposits on alkali halides. He modelled these particles in terms of arrangements of twin related single crystal tetrahedra packed along the (111) planes. The highest fraction of these MTP's were of the decahedral type (Dh) that had nucleated with a <110> epitaxy, as shown in Figure 4.5, while a very small fraction (2% of the total) was seen to be of the icosahedral (Ic) type with a <112> orientation (Figure 4.6). Of the Sc particles, most existed with a primary <100> epitaxy, a smaller number in a <110> epitaxy; an example of the latter is shown in Figure 4.7 (for more details on the structure of these MTP's as observed by HREM, see earlier reports on the topic[166,169]).

The morphology percentages of both the Sc and the Dh particles were found to be strongly dependent on their sizes. The fractional population of Sc's showed an increase with increasing size, while a reversal in trend was observed in the case of Dh MTP's, i.e., a decrease in population with an increase in size (Figure 4.8). These results implied extensive reconfiguration of the particles during growth, and one such example is the pentagonal single crystal shown in Figure 4.9. The only plausible explanation for its appearance, since a pentagon is a non-equilibrium morphology for a Sc particle, is the transformation of a Dh MTP via grain-boundary migration. Further, all the Sc's in the study had a rectangular shape with edges that were aligned along the (110) planes of the Si substrate and also showed increasing aspect ratios with increase in size. This trend can be observed by measuring the variation of the aspect ratio as a function of the area occupied by a typical Sc, as shown in Figure 4.10. Finally, it should also be noted that no particle fluctuations were ever observed during the course of the experiment.

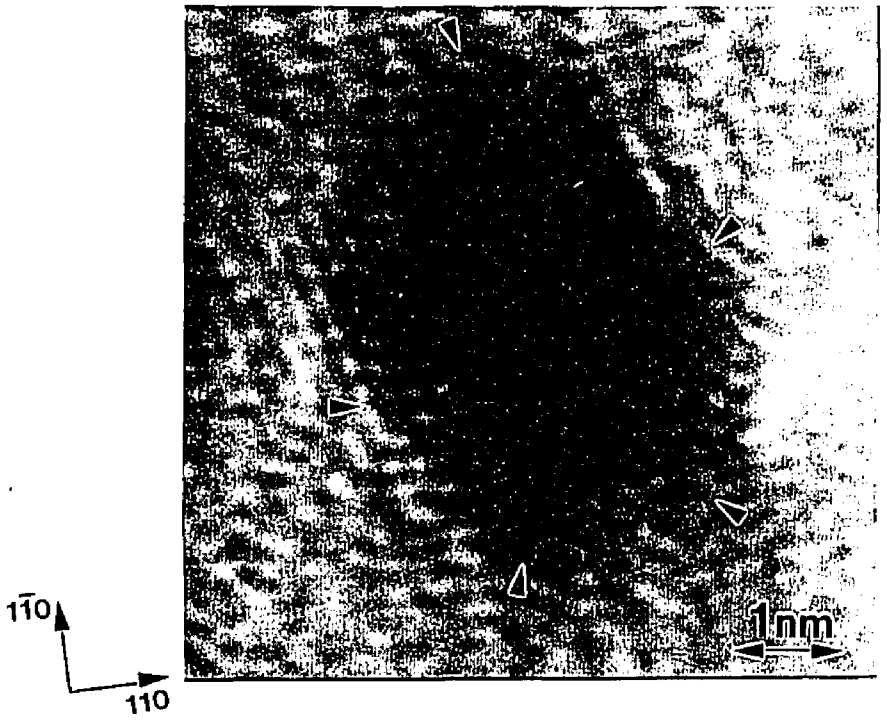

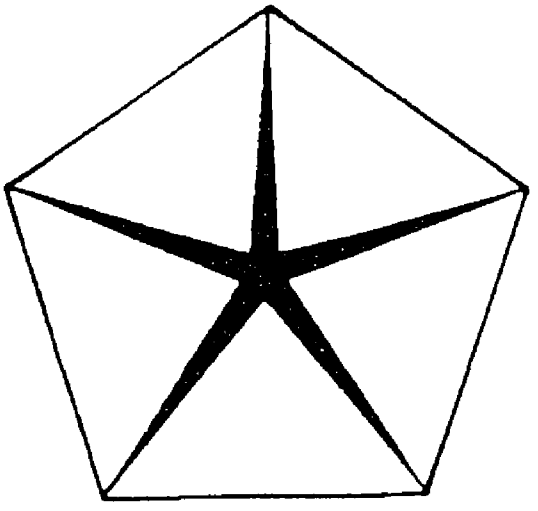

<110>

Figure 4.5. (a) A <110> oriented decahedral multiply twinned particle (Dh MTP) particle of Ag on a Si(001)-2x1 substrate with arrows indicating the five twins separating the {111} facets. (b) A schematic of a Dh MTP in the <110> orientation (adapted from Ajayan, P. M.; Marks, L. D. *Phase Trans.* **1990**, *24*, 229).

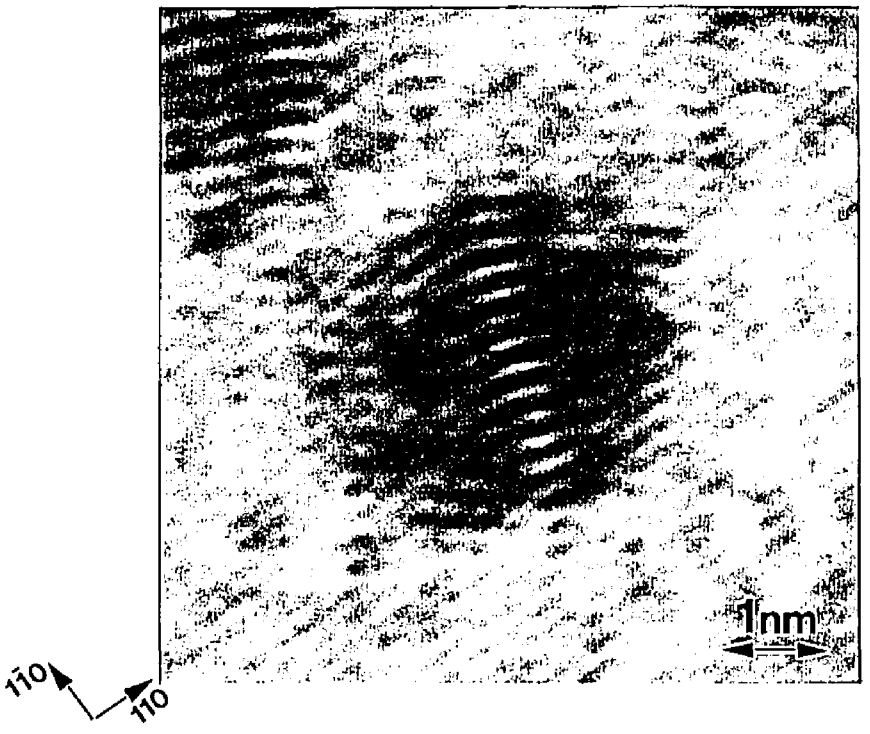

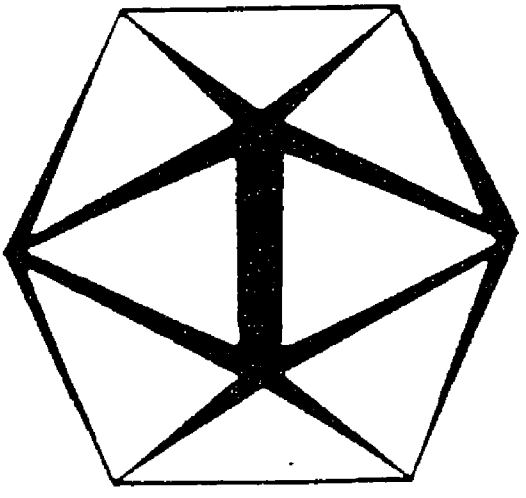

<112>

Figure 4.6. (a) A <112> oriented icosahedral multiply twinned (Ic MTP) particle of Ag on a Si(001)-2x1 substrate. (b) A schematic of an Ic MTP in the <112> orientation (adapted from Ajayan, P. M.; Marks, L. D. *Phase Trans.* **1990**, *24*, 229).

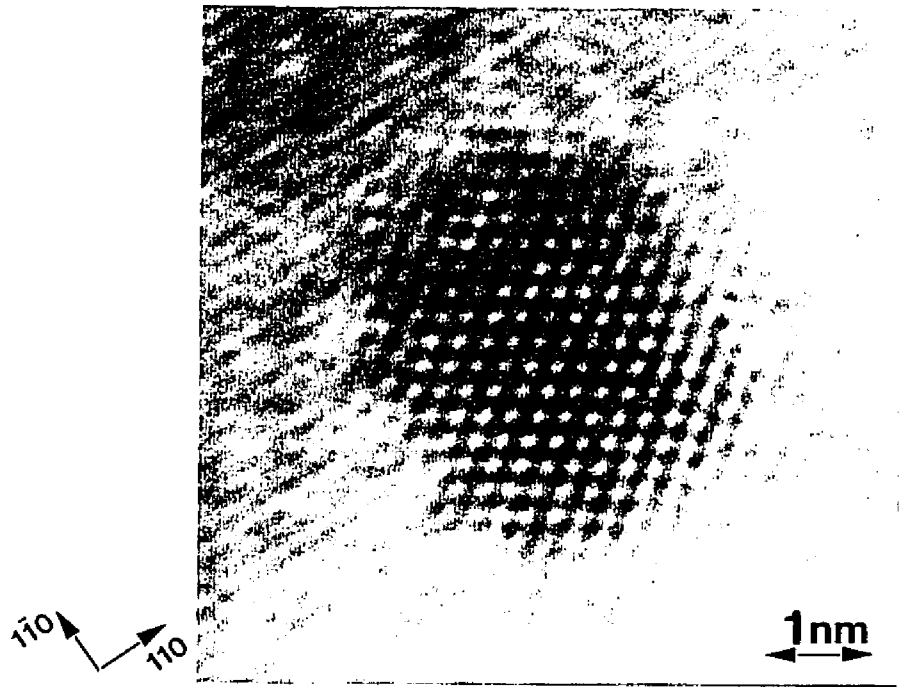

Figure 4.7. A <110> oriented single crystal particle of Ag on a Si(001)-2x1 surface; the (220) fringes of the substrate and (111) fringes of the particle are clearly seen.

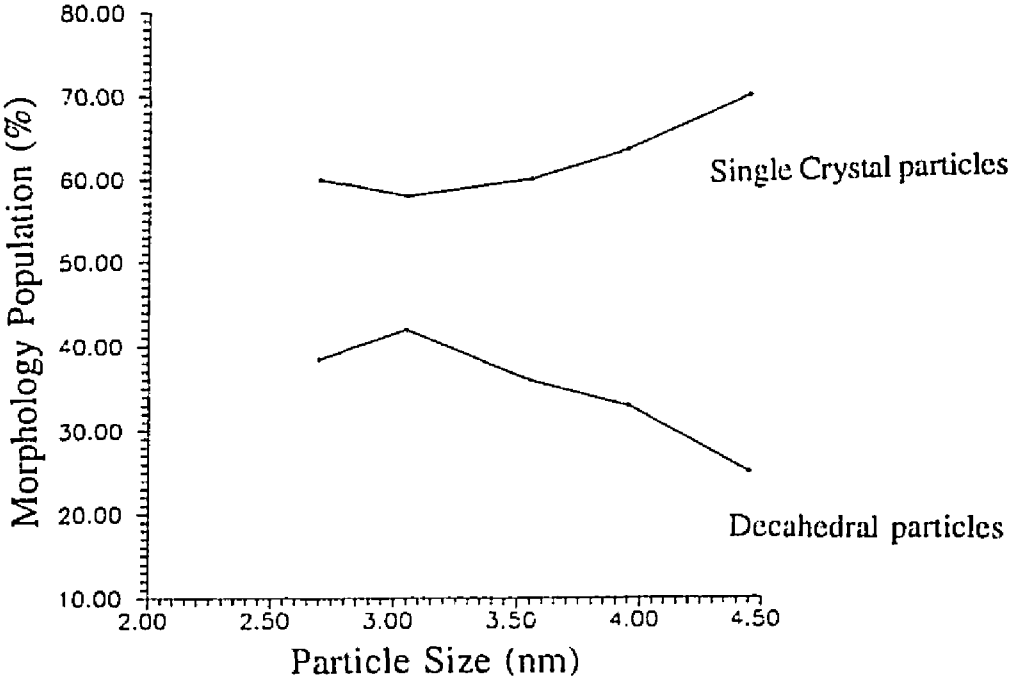

Figure 4.8. Plot of the population density of the decahedral and single crystal morphologies as a function of particle size showing a strong size-morphology inter-dependence.

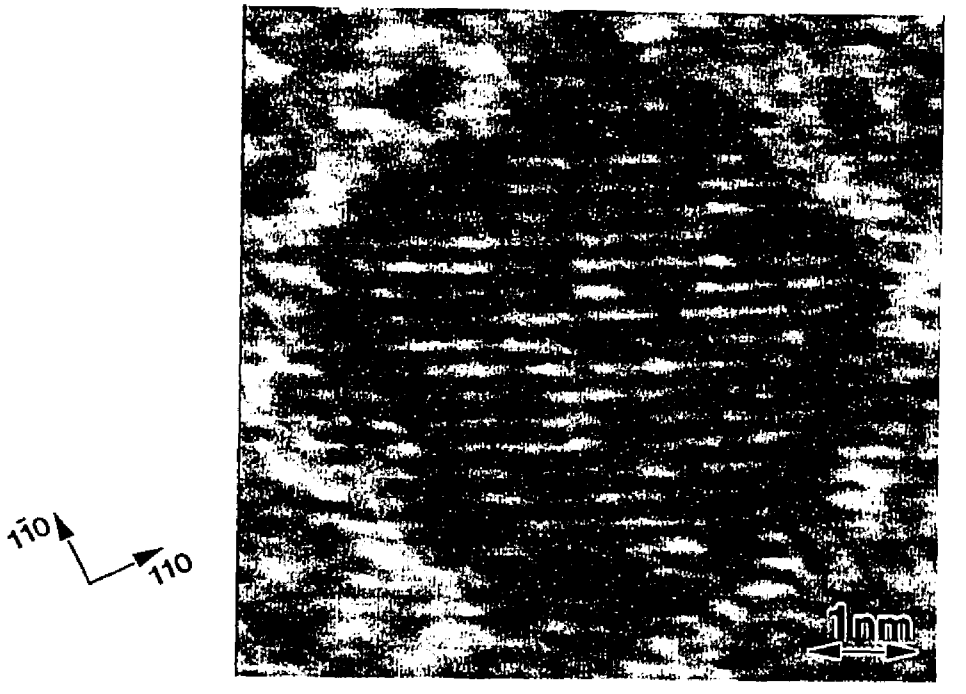

Figure 4.9. An atypical pentagonal single crystal Ag particle on a Si(001)-2x1 surface indicating inter-morphology conversion via grain boundary migration.

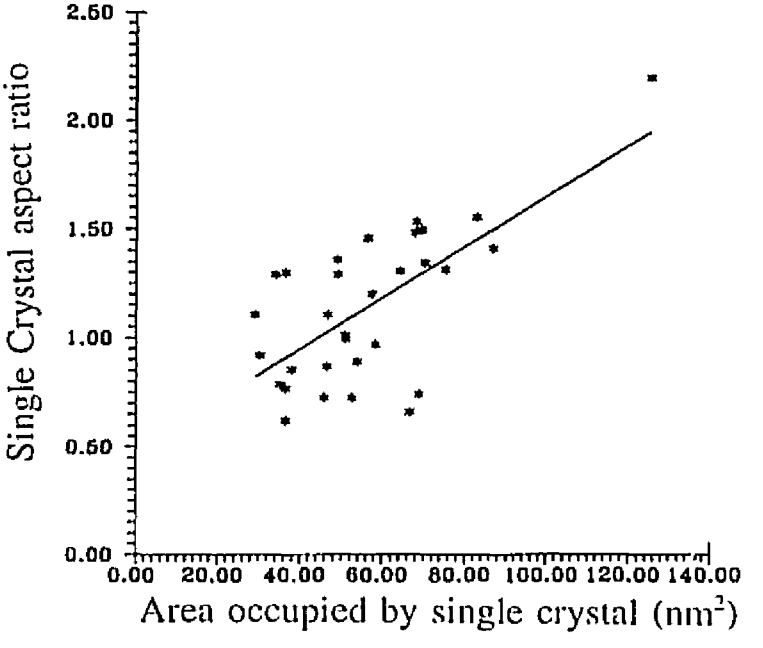

Figure 4.10. Plot of the aspect ratio of the rectangular single crystal particles of Ag on a Si(001)-2x1 substrate, as a function of the occupied area, showing an increase in the aspect ratios with size.

4.2.4 *Discussion*

The observations conclusively demonstrate that, rather than being simple flat single crystals (as suggested without proof in earlier studies), the 3D Ag islands show a classic mixed morphology growth mode, very similar to that found in fcc metals deposited on oxides and alkali halides[165,166,170,171], i.e., a combination of Sc's and MTP's with different orientations relative to the substrate. This could possibly explain the different epitaxies reported by earlier studies. Numerous experimental studies[165,172,173] on small particles have shown that MTP's occur in small particles, under both UHV and non-UHV conditions. Theoretical models[174-178] have also clearly demonstrated that MTP's are the thermodynamically stable entities at the sizes seen in this investigation; in fact, similar results in terms of the relative probabilities of occurrence of Sc's, and the Ic and Dh MTP's have been reported in a recent experimental study[168].

Almost all of these studies place the Ic MTP's as the most favorable morphology at such small sizes (< 10nm). The Ag/Si(001)2x1 system, however, differs from these other systems exhibiting mixed morphology growth (and the theoretical predictions) since there is an unusual lack of these particles. A possible reason is that all theoretical analyses to date (except the early work of Ino[174]) have ignored the effect of the substrate on the final morphology of a small particle, as first suggested by Winterbottom[179]. Since there is no simple way for an Ic particle to adopt a <110> epitaxy, it can be hypothesized that the deposit/substrate interaction effect, i.e., the interface, inhibits their formation. This hypothesis about the effect of the interface on the properties of the system is

supported by a number of different observations:

a) Ino[174] showed that the critical diameter for the Ic MTP stability decreased for systems with strong interfacial forces. The absence of Ag particle fluctuations under the electron beam is a good demonstration of such operative forces in the system (since dynamic fluctuations are reported for Ag particles on other amorphous and crystalline substrates[168,180]). This interfacial force thus probably explains the dominance of Sc and Dh MTP's at sizes where the Ic MTP's are reported to be thermodynamically more stable.
b) Further, the fraction of Ic MTP's increased on exposure to air (although the Ag particles still continued to exhibit a mixed morphology of Sc's and MTP's). This can be attributed to the effect of the gas environment on both the interface between the particles and the substrate (resulting in an oxide layer at the interface), and on the Ag particles' surface free energies[175,176]. In fact, the modification of the interfacial energy due to the presence of such an oxide layer[164] is reported to yield films with better epitaxy.

The grain boundary transformation phenomenon resulting in the pentagonal Sc in this system has also been observed in case of alumina particles[181], while the morphology-size interdependence reported in the study was first documented by Yagi *et al.*[180] during growth of Au and Ag on MoS_2 and MgO under UHV conditions. Other *in situ* TEM observations on the evolution of MTP's during growth[164,182-184] showed that these MTP's either just grew in size while retaining their original morphology/profile or coalesced with neighboring particles (single crystals or MTP's). In case of the latter, the final morphology would consist of either particles of irregular shape, MTP's, simple Sc's, or

other more complicated structures, e.g., lamellar-twinned particles (LTP's) and polyparticles[185]. These compound structures would deteriorate the orientation of the final epitaxial film, in comparison to the one that would result if the initial morphology were dominated by the single crystals. The MTP's evolving out of such coalescence processes are in some instances found to be remarkably stable at larger sizes (where they are predicted to be thermodynamically unstable relative to Sc's), e.g., Haluska *et al*[186] report MTP's in fullerite crystals of sizes up to a few mm; thus stressing the need for proper characterization of the film morphology in the initial stages of growth.

On the basis of these HREM data, it is now possible to interpret the features in the TED patterns accurately. The different epitaxies of the MTP's and the Sc's seen in this study coupled with the strain internal to the MTP's (the assembly of Sc tetrahedral units is not space filling and inhomogeneous strain or bond length distortions are required to produce a space filling MTP entity[173]) will give rise to the rotational disorder which, in turn, would be responsible for the arcs[165,166] in Figure 4.2.

Finally, the rectangular shape of the Sc particles (with edges parallel to the (110) planes of the Si substrate), can possibly be attributed to the structure of the 2D layer. STM studies[139,150,152,162] show that the Ag adatoms are preferentially adsorbed either on the cave or bridge[154] sites between two Si dimer rows. Higher coverages were observed to lead to either long Ag adatom chains[150] or rectangular single-layer 2D islands[154], aligned along these two fold bridge sites. Further, a cluster model study[187] of Ag bonding and migration on these clean Si(001) substrates compared the different adsorption sites and found that the Ag adatoms strongly favor migration between Si dimer

rows and perpendicular to them; this adsorption behavior is directly related to the inherent anisotropy of the clean dimerized surface (tensile stresses operate parallel to the dimer rows with compressive stresses in the orthogonal direction[188]). It is this strong substrate stress effect which probably explains the nature of the Sc islands; this remains a hypothesis, however, since HREM data do not directly confirm the presence of either the linear rows or rectangular 2D islands (and therefore, its influence on the final morphology of the 3D Sc islands).

In conclusion, a phase map of the morphology of Ag deposits on clean Si(001) surfaces at room temperature can be constructed by collating the data acquired from this study with those reported by other authors; this is shown in Figure 4.11. After the saturation 2D layer coverage, the 3D islands nucleating on such surfaces are dominated by Sc's (over the MTP's) from the smallest sizes observed in the study with the dominance becoming stronger at larger sizes.

The highlights of the study can be summed up as follows:

a) The investigation demonstrates that one of the most fundamental questions about the growth mode of Ag on clean Si(001), i.e., the particle structure, has escaped more than a decade of study. The pitfall of interpretation based solely on diffraction data is also revealed.

b) The small fraction of Ic particles raises some fundamental scientific questions on the variation in types of island morphologies with environment conditions, and merits further investigation. Further, the changes in the fraction of Ic particles on exposure to air underlines the importance of observation under UHV conditions.

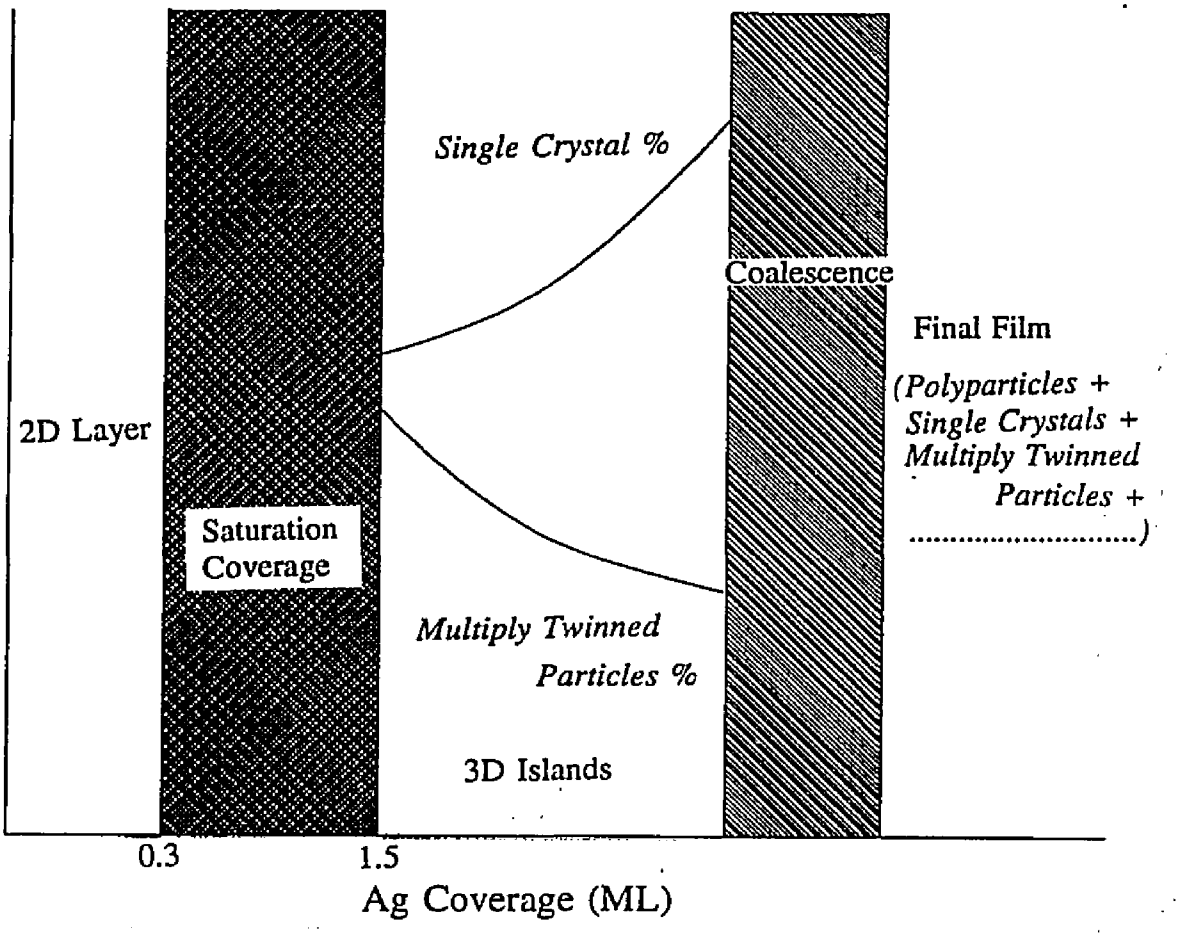

Figure 4.11. A schematic phase map for the structure evolution (from earlier reports and current study, see text) of Ag deposits on Si(001)-2x1 substrates at room temperature as a function of Ag coverage.

4.3 Au-Si(001)

4.3.1 *Background*

In contrast to the Ag/Si(001) system, room temperature studies of the Au/Si(001) interface are mainly concerned with the formation of an alloy, the critical thickness of Au required to initiate this reaction, and the mechanism by which such a reaction proceeds. It is now generally agreed upon that Au deposition on clean Si(001)-2x1 surfaces results in the formation of an alloy above a certain critical thickness[141-144]. There is little agreement, however, over this value; in fact, values span the submonolayer, e.g., 0.33 ML[141] or 0.5 ML[142] to a few monolayer, e.g., about 2-4 ML[143,144]. Low energy electron diffraction (LEED) studies[142,145-147] also report that in the very initial stages of Au deposition, the Si(001)-2x1 spots weaken in intensity and finally disappear, leaving behind a 1x1 surface. Real-space STM[189] measurements reveal regions to be locally ordered to a coverage of 1 ML: Au atoms are reported to form dimers and grow as 2D layers in a local 2x2 structure with further Au deposition resulting in the appearance of the 1x1 structure as reported by LEED. At much higher coverages, i.e., 3nm, a weak diffuse ring of gold-silicide, which sharpened into spots on increased deposition, has also been observed[146].

The annealing behavior of the system has been studied primarily using LEED[145-149]. These studies reveal a variety of surface reconstructions for the system, depending on the Au coverage and annealing temperature. For example, a 5x1 structure[148], and a c(8x2) type pattern that transforms to a $\sqrt{26}$x1 (alongwith 1/3 order streaks) or a $\sqrt{26}$x3

(alongwith 1/2 order streaks) structure[145,146] have all been reported. In fact, a schematic phase map for the appearance of the different reconstructions as a function of these two parameters was even proposed in one of these studies[146]. One of the drawbacks, however, of interpreting real space structure from the periodicities in diffraction patterns is that the latter are averaged over the region of the probe.

In fact, using STM-LEED, Lin *et al.*[149] showed that the $\sqrt{26}$x3 structure reported by these earlier LEED investigations actually corresponds to a mixture of 5x3 and $\sqrt{26}$x3 units in real-space (this is the only real-space investigation on the interface, to the author's knowledge). A schematic of the structure proposed by the study is reproduced in Figure 4.12 and its main features are highlighted below.

Structure Model from STM

Both the 5x3 and $\sqrt{26}$x3 units comprised *stripes* running along the <110> directions with an inter-stripe spacing of 5α, where α represents the spacing between the (110) planes in bulk silicon. Each stripe in turn contained four parallel rows with atomic scale features of two different sizes called A and B, while others had in addition a lower density of some very bright features called C. These stripes were labelled type(i) and (ii) respectively. Every fifth row on the surface was missing, resulting in a *trench* separating adjacent stripes. Features of the same type were spaced 3α apart in the direction parallel to the stripe and the arrangement of the stripes determined either a 5 or a $\sqrt{26}$ periodicity in the orthogonal direction, i.e., the 5x3 unit resulted from adjacent type (i) stripes, while a phase slip of 1α due to the presence of a type (ii) stripe between two type (i) stripes

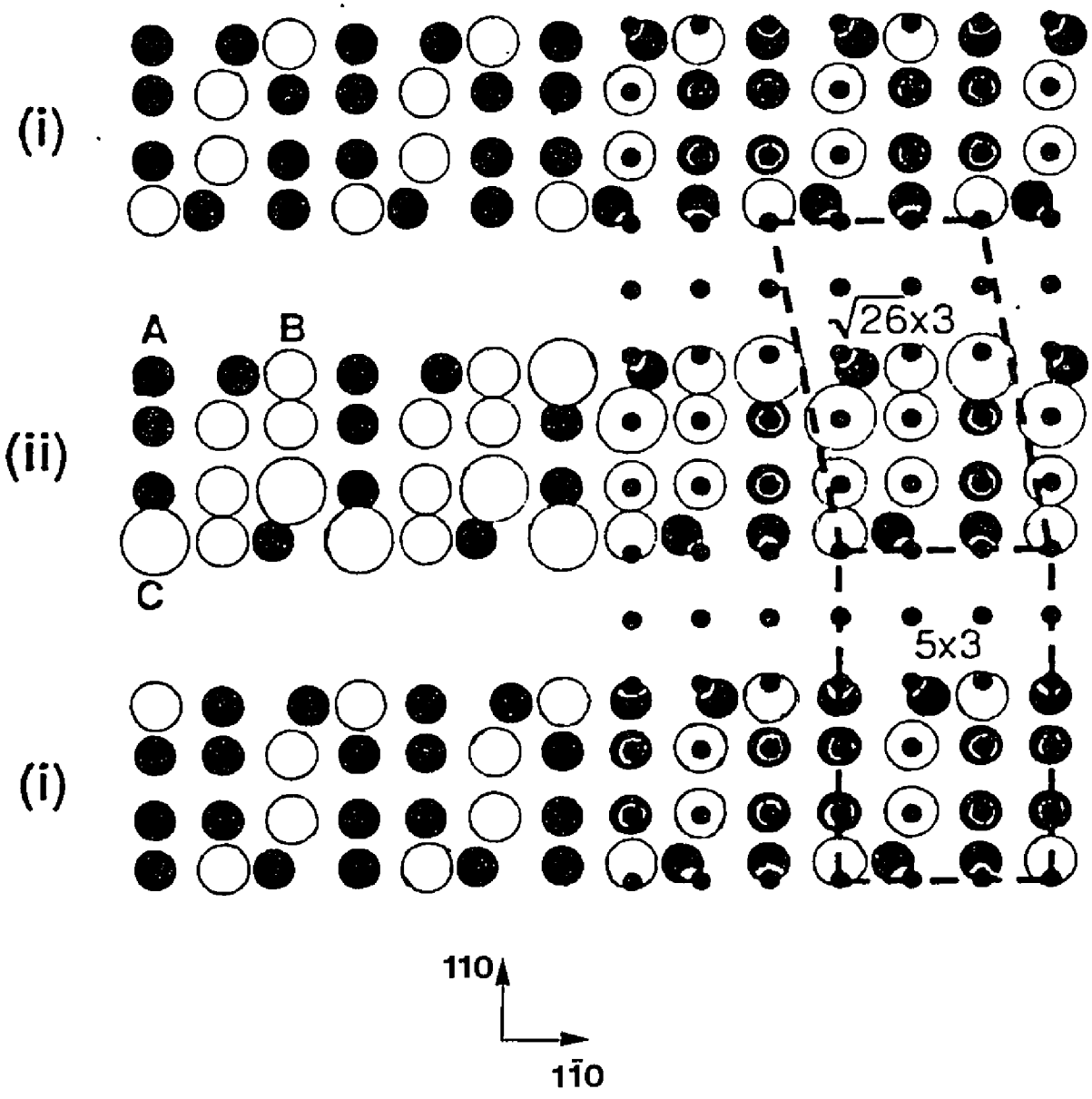

Figure 4.12. STM structure schematic showing the arrangement of stripe types (i) and (ii) resulting in the 5x3 and √26x3 cells of the annealed Au-Si(001) interface. Features A, B, and C, of different sizes on the stripes are shown with the small black circles in the right half of the figure denoting the 1x1 bulk locations. Note the compression of the outer rows of the stripes (adapted from Lin, X. F.; Wan, K. J.; Glueckstein, J. C.; Nogami, J. *Phys. Rev.* B **1993**, *47*, 3671).

caused the $\sqrt{26}$x3 structure. The outermost rows on the stripes were also reported to move in towards the center with the inner two rows staying in bulk locations, resulting in a 17% compression; this phenomenon was believed to be similar to the dimerization of the clean surface. Although the images were unable to reveal conclusively the chemical identity of the features on the stripes or inside the trenches (i.e., Au or Si), using X-ray photoelectron spectroscopy (XPS), a maximum limit of 0.7 ML was suggested for Au that could remain in the first four layers[149] in a 5x3 structure. This is in disagreement with Rutherford backscattering spectroscopy data[148] which placed the value at 1.7 ML for a 5x1 surface.

This lack of understanding about the chemical distribution of the species in real-space and actual origin of the compression of the surface layer provided the main motivations to study the annealed Au-Si(001) interface.

4.3.2 *Experimental Results*

TED Data

TED patterns following room temperature deposition showed features consistent with those reported by earlier diffraction studies[142,145-147]. At the initial stages of deposition, only a decrease in the intensity of the Si surface spots was observed. These spots disappeared leaving behind a 1x1 surface and an extremely diffuse ring, which sharpened as the coverage was increased to roughly 3 ML, where 1 ML of Si on a (001) surface corresponds to a density of 6.8×10^{14} atoms/cm^2; these features are shown in

Figure 4.13. Although the ring spacing suggested formation of a gold-silicide compound, lack of surface spectroscopy data precludes any further comments on this issue.

Figure 4.14 shows a TED pattern obtained on annealing this surface (with ~3 ML Au). One-fifth order spots and weak one-half order streaks, were seen along the two <110> directions. Strong intensity of the eight sets of spot pairs (the origin will be discussed later) and the 1,6/5 type spots are the other noticeable features in the patterns; one such spot pair and a 1,6/5 spot are labelled as **A** and **B** respectively in the figure. These spot pairs did not always co-exist with the reconstruction spots, and were found to vary in intensity as a function of processing conditions. While numerous hypotheses can be advanced to explain the origin of these features in the TED patterns, a better understanding can be obtained from real space HREM data, as will be explained below.

HREM Imaging Data Processing

A series of through-focal HREM images were collected, digitized using the Optronics P1000 microdensitometer, and analyzed using SEMPER software. Although the images were recorded in both the on-zone and off-zone modes the latter were used primarily in the analyses, for reasons described earlier. (Results presented here were obtained from analyses of a 14 member through-focal series.) Under such conditions, as described earlier in Chapter 2, intensity at each point is given by equation 2.18, i.e.,

$$I(r) = 1 + \sigma t \int [\{A(u)\cos\chi(u) + B(u)\sin\chi(u)\}E(u) + \eta(u)]\exp(2\pi i u.r)\, du \quad (4.1)$$

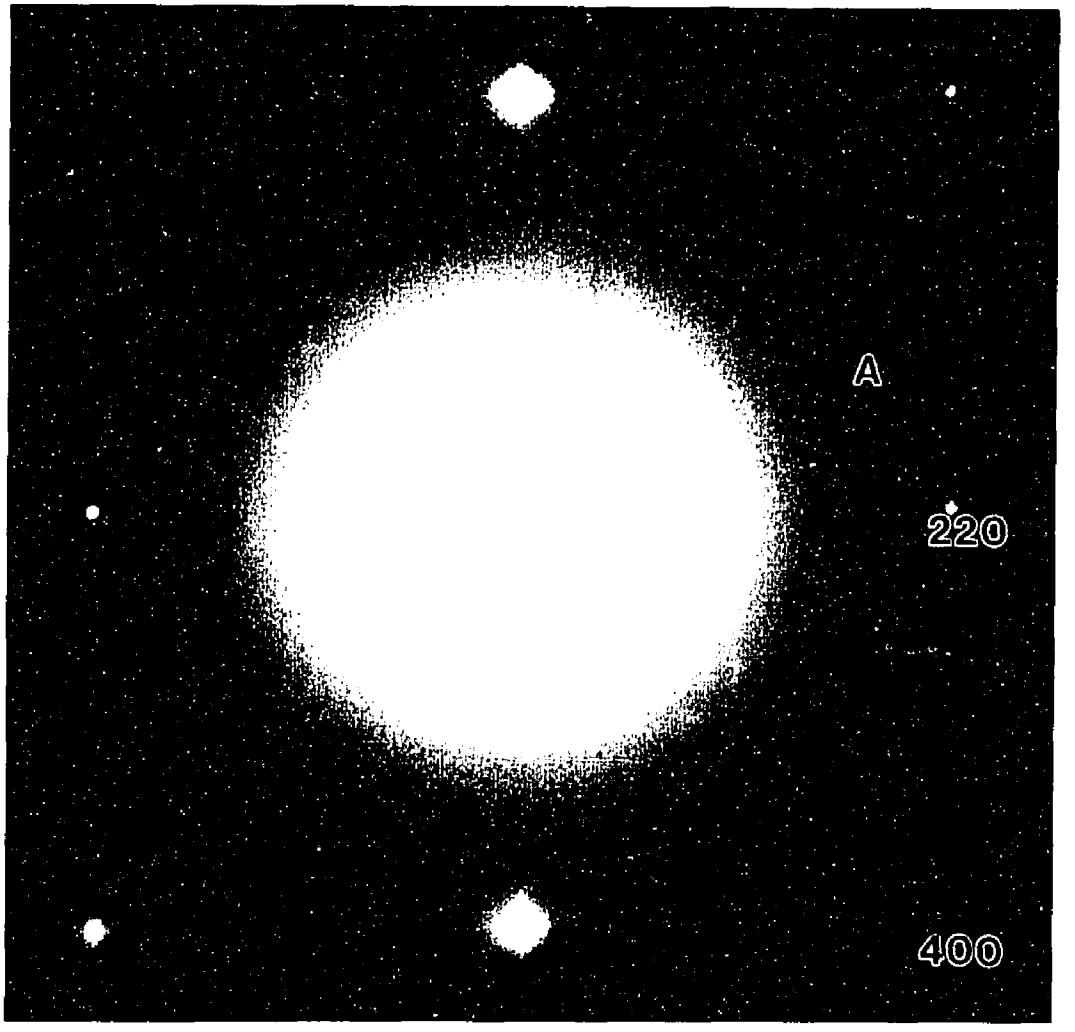

Figure 4.13. A TED pattern following deposition of 3ML of Au on Si(001)-2x1 surface at room temperature; substrate reconstruction spots are absent and a weak, diffuse polycrystalline ring of gold or gold silicide is denoted by A.

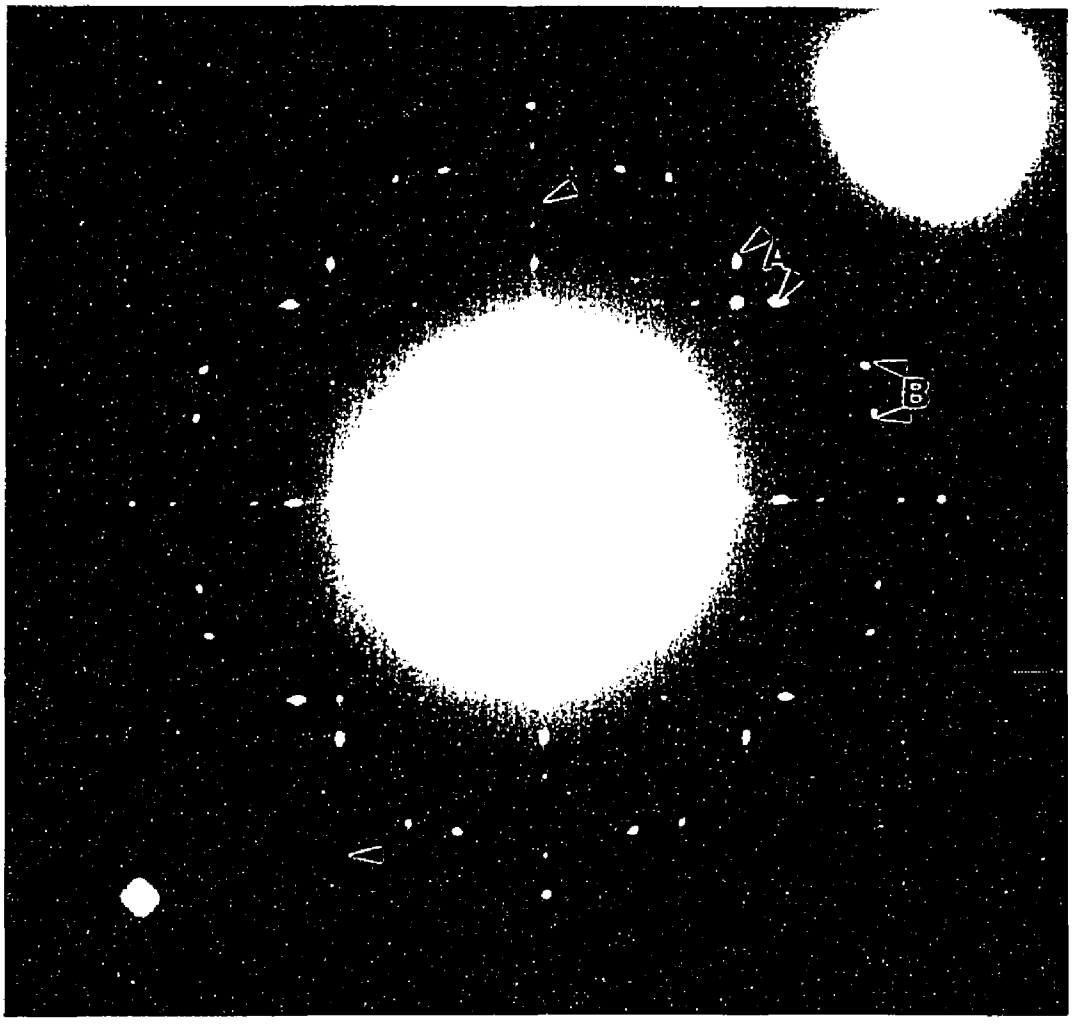

Figure 4.14. A TED pattern following annealing of the Au-Si(001) interface in Figure 4.13. One-fifth order spots and weak one-half order streaks along the <110> directions are arrowed. **A** and **B** denote a 1,6/5 spot and a spot pair respectively; these features are stronger in intensity than the basic reconstruction spots.

To faithfully reconstruct the wave exiting the sample, the parameters E(u) and η(u) have to be estimated and the envelope term removed out from the images (to avoid singularity effects in the reconstruction process). One of the problems with gathering data in the off-zone condition is that the signal is small and so, noise becomes very important. As the first step therefore, the images were enhanced by reducing the noise using a parametric Wiener filter[167], similar to that used in the Ag/Si(001) system. Figure 4.15 demonstrates the result: a montage of the same region in a HREM image, prior to, and after application of the filter. Signal to noise enhancement by a factor of about 6 is typically obtained[167]. This noise-filtered image clearly shows the appearance of stripes with a periodicity of nearly 1.92 nm, which corresponds to five times the spacing between the (110) planes in bulk silicon.

Envelope Calculation

Calculation of the terms, χ(u) and E(u), involved estimation of the spherical aberration coefficient, defocus, convergence, and focal spread terms (from equations 2.15 and 2.18). These parameters were calculated for the series of through-focal images obtained from the annealed surface. (Artifacts that might appear at a particular defocus are eliminated by recording such through-focal series.)

The spherical aberration coefficient C_s calibration for the UHV-H9000 microscope was carried out using a well-documented procedure[58], and a value of 1.6mm for an operating voltage of 300kV was obtained. Calibration of the defocus step was carried

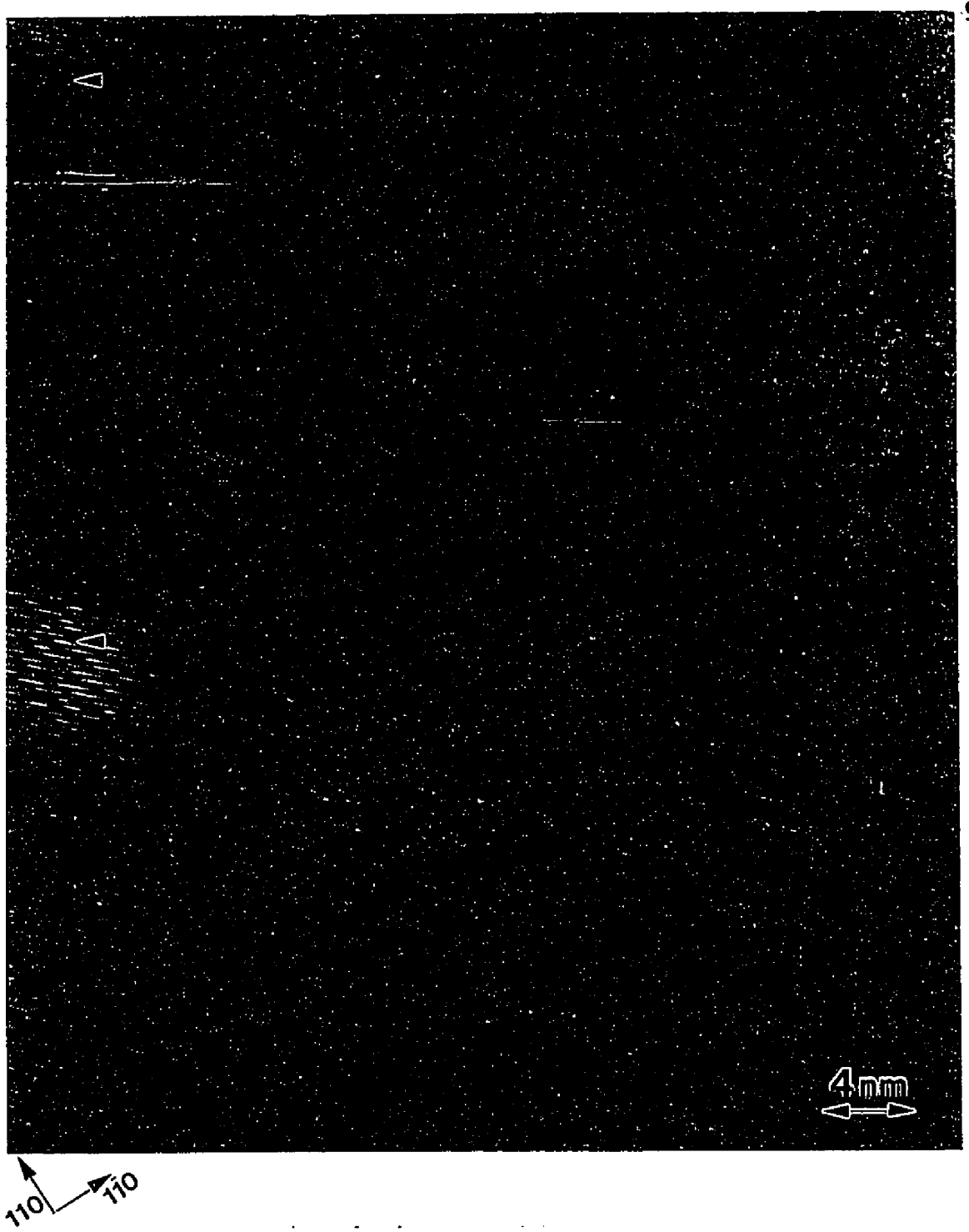

Figure 4.15. Demonstration of noise removal from HREM images using a parametric Wiener filter[167]. The pre-filtered image with a particle arrowed for reference is shown on the top, while the noise-filtered image with the same arrowed particle is shown at the bottom. Stripes in the filtered image are spaced 1.92nm apart.

using a particle feature in the images as a marker; this ensured that exactly the same region was analyzed in the different images. Using the values of C_s, focal spread, and convergence (the convergence angle in mrad is defined by the ratio of the width of a diffraction disc to the corresponding inter-planar spacing), it was established that the actual defocus step between successive members of a through focal series was 14nm, when the defocus knob was set to step by 30nm. (This was calculated by matching optical diffractograms of experimental images against simulated ones.) Also, beam flutter seen during image recording was incorporated in the form of an anisotropy in beam convergence. From these parameters, the actual defocus value for each member of the series was established, the envelope term calculated, and eventually filtered out of the images.

This envelope removal from the noise corrected images was performed using an envelope-weighted parametric Wiener filter[190]. Figure 4.16 shows one such image at a defocus of 94nm (where Schertzer defocus is 56nm), corrected for both the envelope and noise contributions, and demonstrates the inhomogeneities in the stripe periodicity (would give rise to the streaks in the diffraction patterns). Heavy directionality is also seen in the images in the form of line features running at 45° to the rows; the origin of which shall be described later.

Power spectra of such noise- and envelope-corrected images were subjected to a least squares minimization process[190] to approximately invert for the crystal exit wave. Figure 4.17 shows the imaginary component of the exit wave reconstructed using this

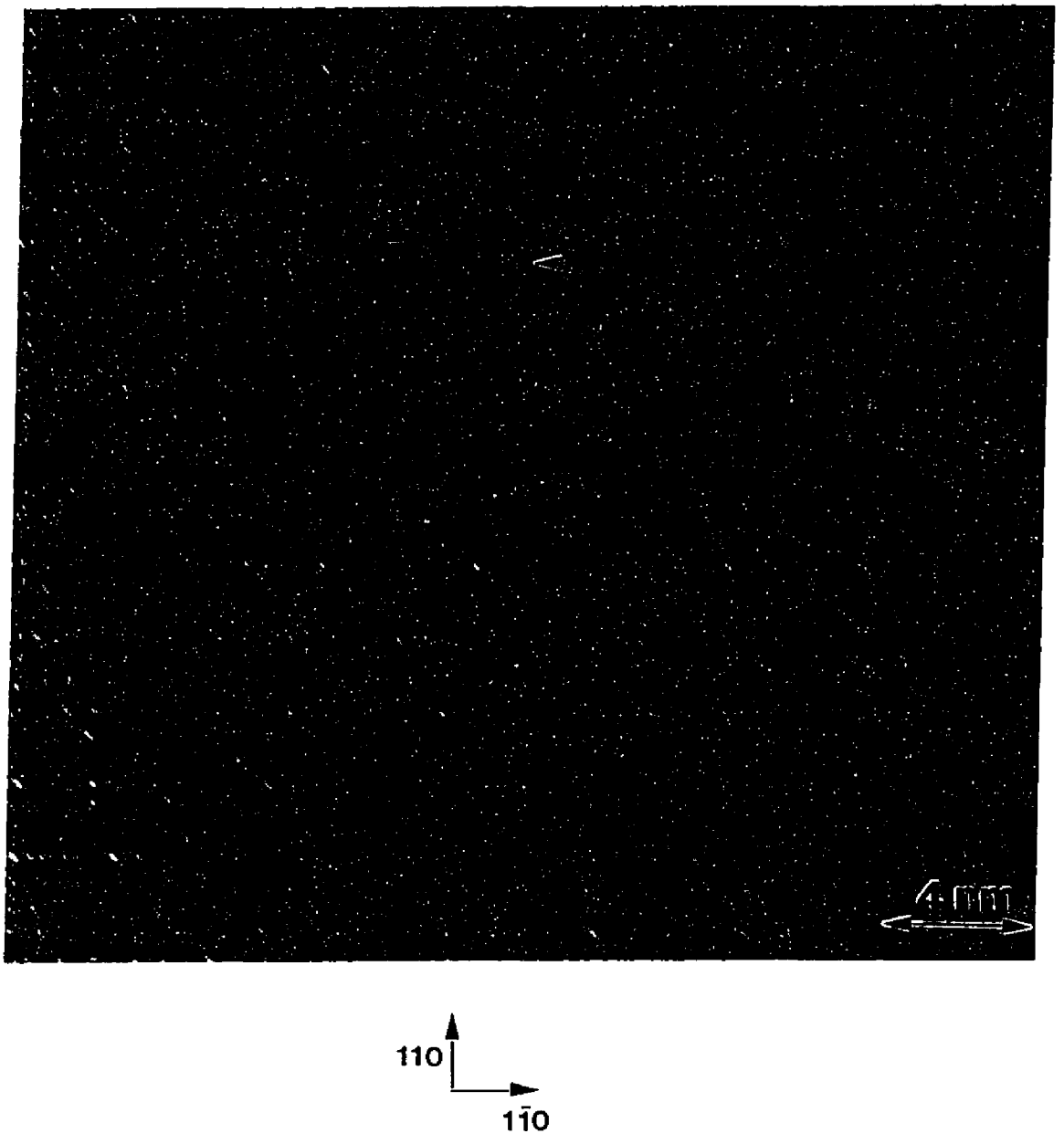

Figure 4.16. Envelope-correction of an image recorded at a defocus of 94nm. The arrow shows the inhomogeneities in the reconstruction periodicity.

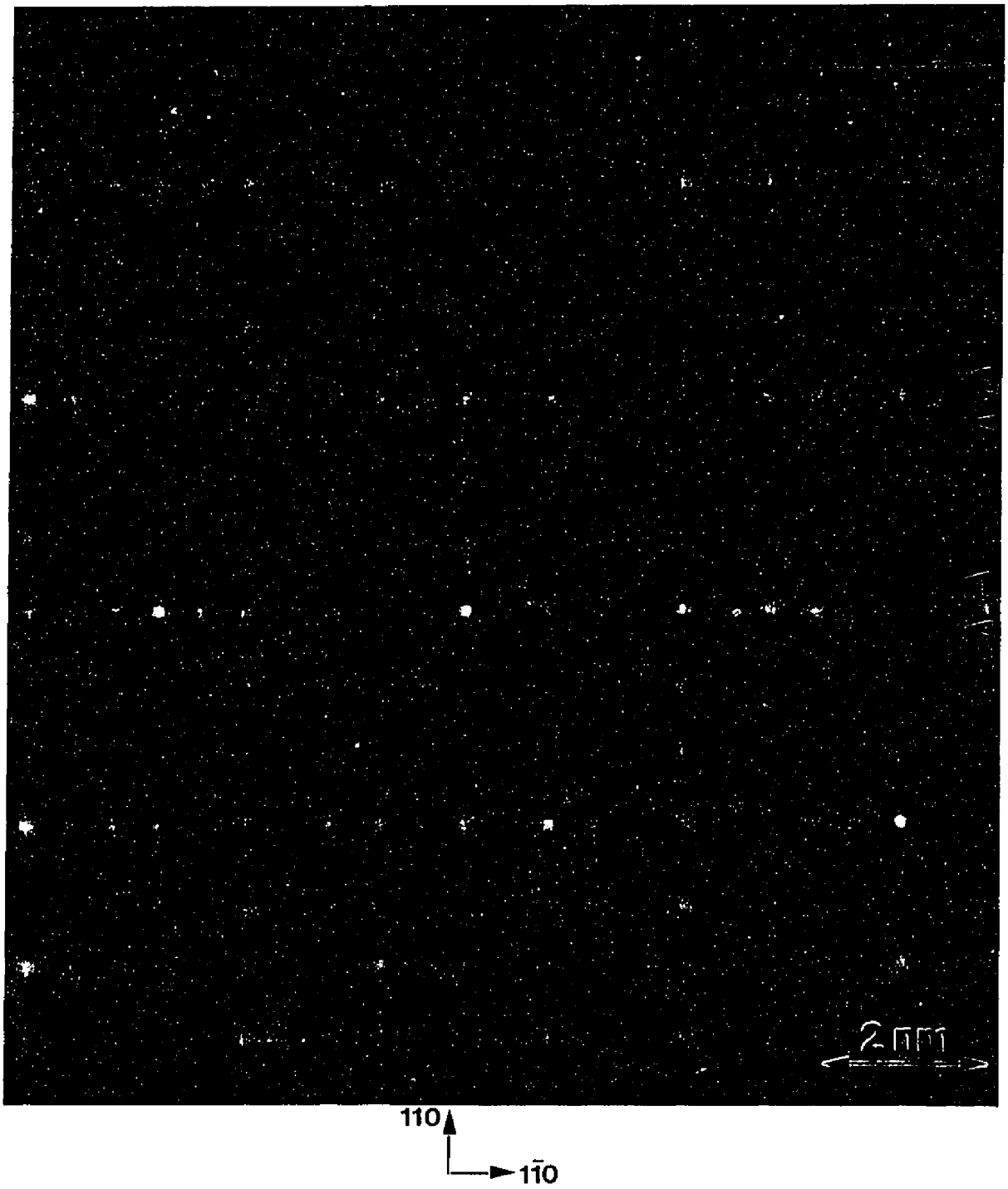

Figure 4.17. The imaginary component of the exit wave reconstructed for an image recorded at a defocus of 118nm. Pairs of high contrast rows shown by the arrows spaced 0.576nm apart are lined with Au-atoms, and constitute the trench in the STM study[149].

approach, for an image recorded at a defocus of 118nm.

4.3.3 *Data Analysis*

Using the TED and HREM data described in the previous section and the published STM results[149], numerical simulations were carried out and a structure model developed. The correct atomic model must satisfactorily explain the features seen in the TED patterns and also be consistent with HREM data. Starting with the HREM data in Figure 4.17, there are pairs of higher contrast rows with an inter-row spacing of 0.576nm, i.e., 1.5α. These can be directly identified as arising due to Au, which scatters much more strongly than Si. The next issue is to register these atoms in the STM structure of *stripes* and *trenches.*

Since the inter-row spacing in the images, which incidentally corresponds to twice the spacing between the (110) planes of pure Au, is higher than that between the (110) planes in bulk Si these rows cannot form part of the stripe (where compression is reported), and would instead line the trench. The Au rows would therefore sit in sub-surface layers, i.e., either the second, third, or fourth layer, where the outer surface is defined as the first layer.

The Trench

The missing surface row in the STM structure model implies that the row directly bonded to it, i.e., in the second layer, could either be present or is also missing (this row

is termed MSSL for missing surface-second layer). This MSSL row along with the two second layer rows directly bonded to the outer rows of the stripe (termed ORSL for outer row-second layer) constitute the two available locations for the Au atoms in this layer in the trench. Similarly, the third layer rows bonded to the MSSL and one of the ORSL rows, and the fourth layer rows bonded to these third layer rows constitute the only possible sites for Au atoms in the trench in the respective layers.

Au atoms were allowed to sit in substitutional sites in these layers and the surface stripe was assumed to comprise purely silicon with the outer rows displaced towards the center, following the STM study[149]. (This compression is also consistent with the structure model obtained from this study, as will be discussed later.) Diffraction patterns were calculated for these four models of the trench, and the stripe using a pseudo-kinematical approach, i.e., for no tilt, and for a single unit cell thickness along the beam direction. Only a single domain of the reconstruction was used.

Visual fitting of these patterns against the experimentally recorded ones revealed that the second row positions could be completely ruled out since the 1,6/5 spots were extremely weak in comparison to the other reconstruction spots. (The 1,6/5 spots were used to test out the different models since they were consistently very strong.) On the other hand, patterns simulated for models with Au in the third or fourth layer positions described above, resulted in intensities several orders of magnitude higher in these spots. However, the intensities were similar for both the third and fourth layer Au models. Further, in contrast to the experimental patterns the intensity value of these spots was identical to that of the 1,7/5 spots.

A partial structure for the trench was thus obtained at this stage with two Au rows in the third or fourth layers. There were, however, other details in the HREM images as well as those observed in STM that needed to be explained, i.e., the *stripes* in the latter.

The Stripe

Since the STM study reports a periodic arrangement of A and B type features on the stripe in a 5x3 cell, Au atoms were assumed to sit in substitutional sites corresponding to these (following the STM schematic, Au substituting for the A-type features were displaced parallel to the stripe; non-displaced positions were also tested).

Starting off with the purely substitutional positions for Au atoms on both the stripes and the trenches, many different permutations of these locations were tested. The main two are:

a) Au atoms (irrespective of their position along the beam direction) substitute for Si directly, sit atop a bulk Si atom, or sit at interstitial locations.

b) The spacing between the Si rows directly bonded to the Au atoms in the trench could either be the bulk silicon separation value, i.e., 1α, or the value of the Au inter-row separation in the trench, i.e., 1.5α.

The 5x3 Cell

On testing these stripe-trench combinations, it became apparent that the intensity of the 1,6/5 spots was highly sensitive to both the concentration and arrangement of the

Au atoms, e.g., putting in Au atoms on the stripe resulted in a dramatic increase in the intensity of the 1,6/5 type spots (relative to the 1,7/5 and other reconstruction spots) as compared to the ones which had the Au atoms only in the trenches, as described in the earlier section. Further, it emerged that for either structure on the stripe (i.e., Au for A or B-type features), the trench with Au atoms substituting for Si sites in the third layer and fourth layer Si atoms staying in bulk positions best explained the experimental data.

This is demonstrated in Figure 4.18 which shows a montage of the TED patterns simulated for the two different locations for Au atoms along the beam direction, i.e., third and fourth layer substitutional sites (Au atoms substitute for the B-type features on the stripe), against Figure 4.14. Figure 4.19 shows the real space structure corresponding to the diffraction pattern in Figure 4.18(a). If the Au atoms were to substitute for the A-type features in Figure 4.19 instead, only an increase in the intensity of the 1,6/5 spots would be observed. In conclusion, a 5x3 cell alone cannot explain the strong intensity of the A-type spot pairs in Figure 4.14.

The √26x3 Cell

Using the √26x3 surface cell instead, the spot pairs were seen to lie on the reciprocal mesh corresponding to the four domains of this cell in real space. Figures 4.20 (a) and b) show two of these domains, labelled A and B respectively. A 90° rotation of these domains, e.g., across a single layer high step boundary, would result in the other two, which we label as C and D respectively. Figure 4.21 is a schematic of Figure 4.14, with letters A-D identifying the √26x3 reconstruction domains described above.

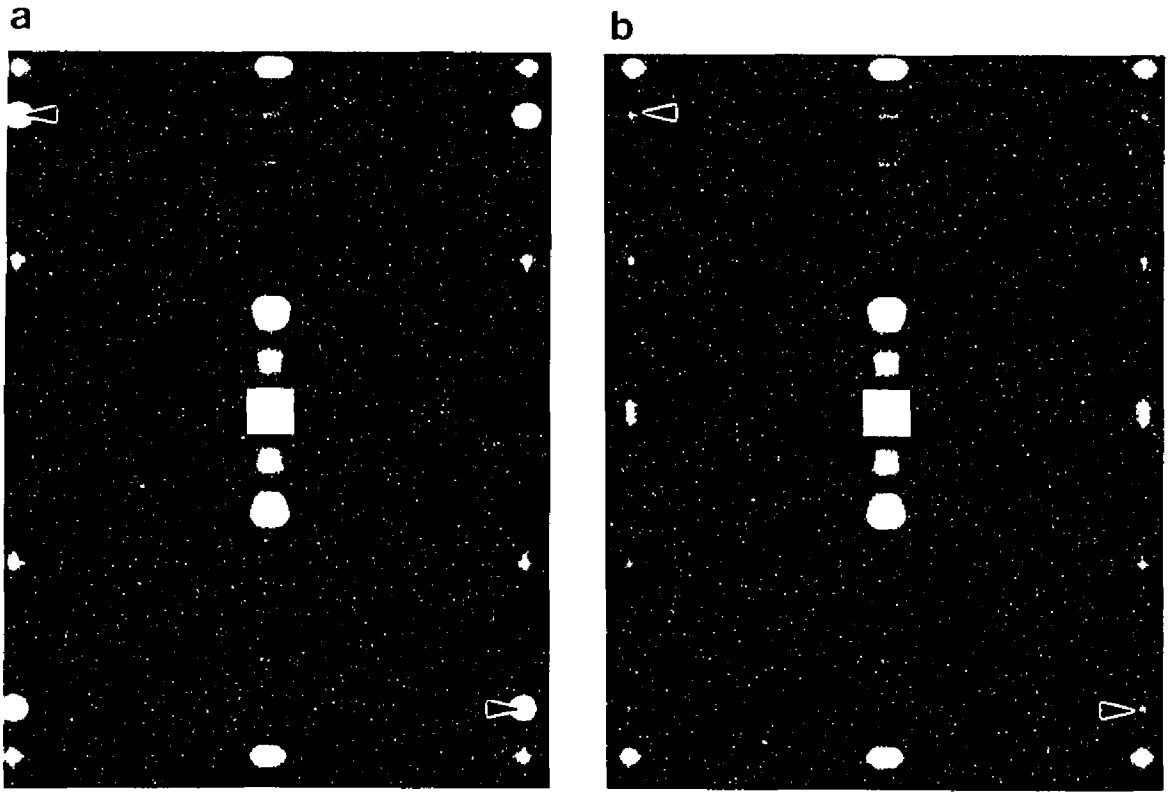

Figure 4.18. Montage of diffraction patterns simulated for Au atoms sitting in substitutional sites in a) the third layer and b) the fourth layer in the bulk. Au atoms on the surface replace the B-type features in the schematic of the 5x3 cell reported by the STM study[149]. The 1,6/5 type spots in the patterns are arrowed for comparison.

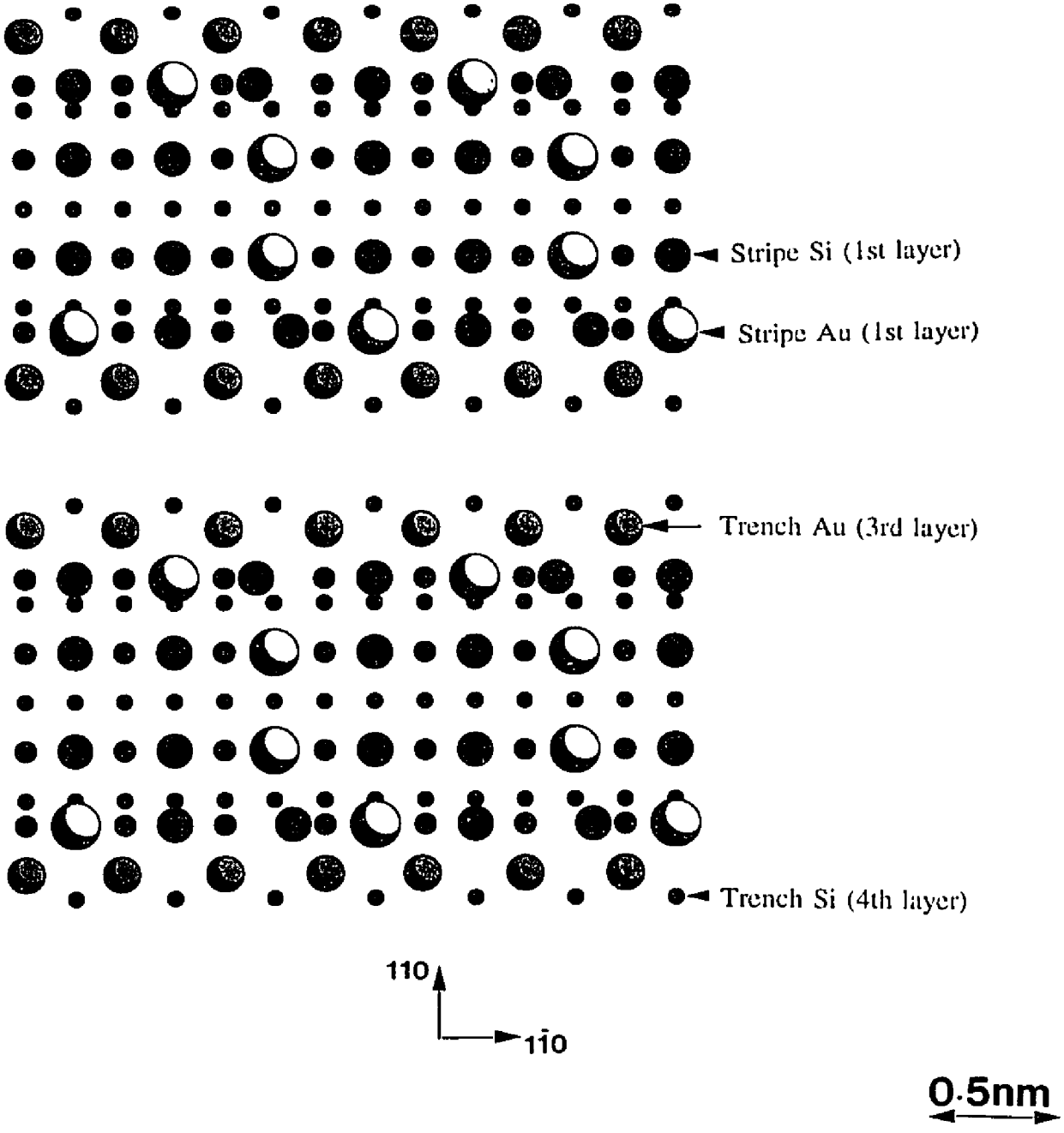

Figure 4.19. Top view schematic of the 5x3 cell used in simulation of the diffraction pattern in Figure 4.18(a). Pairs of Au rows spaced 0.576nm apart line the trench and four Au atoms sit in locations of the B-type features of the STM schematic[149]; note the surface layer compression of 16.7%.

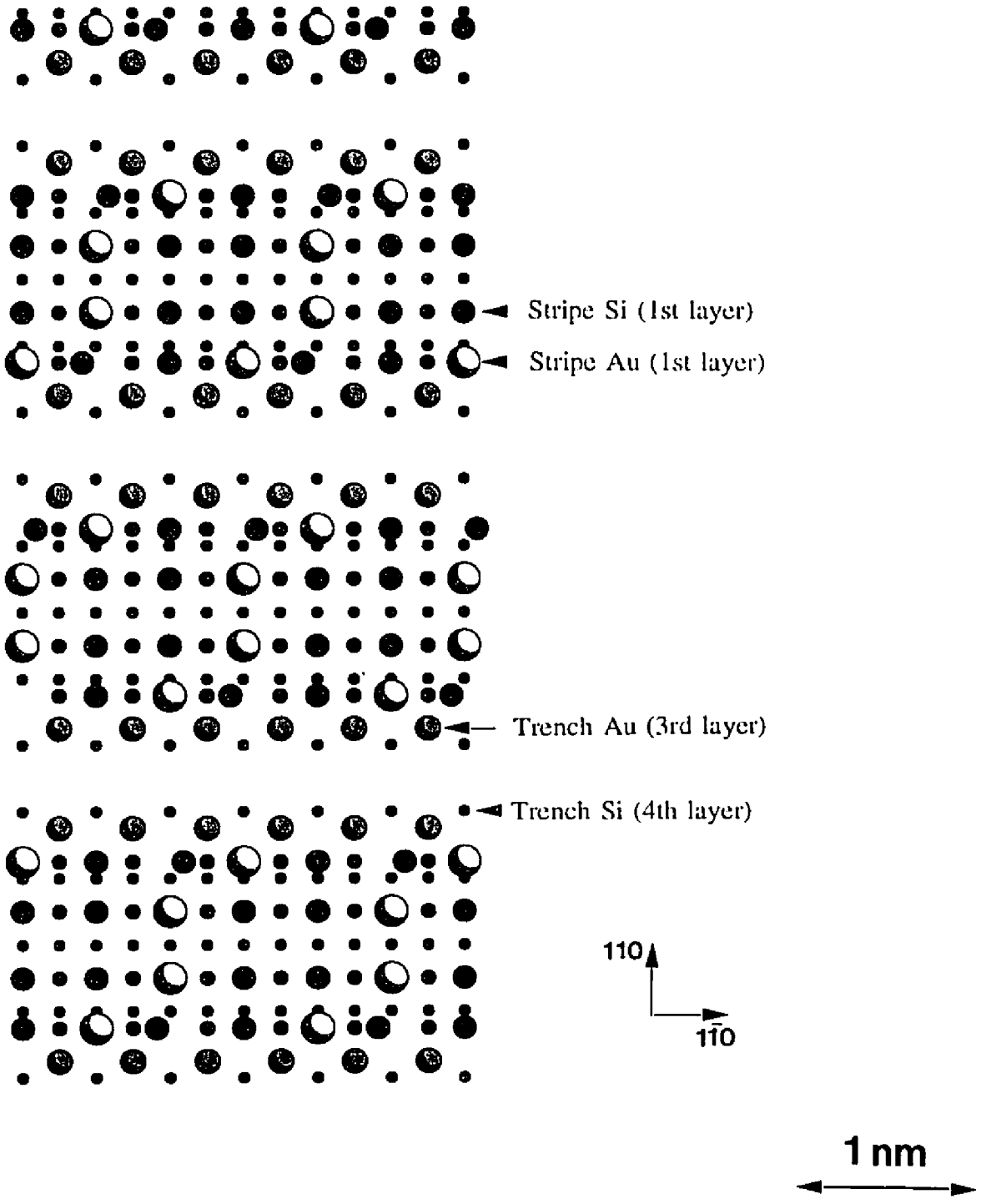

Figure 4.20. (a) Schematic of the top view of the A type domain of the $\sqrt{26}$x3 surface cell. Note the phase slip between adjacent stripes; Au rows line the trench and also substitute for B-type features in the STM schematic[149].

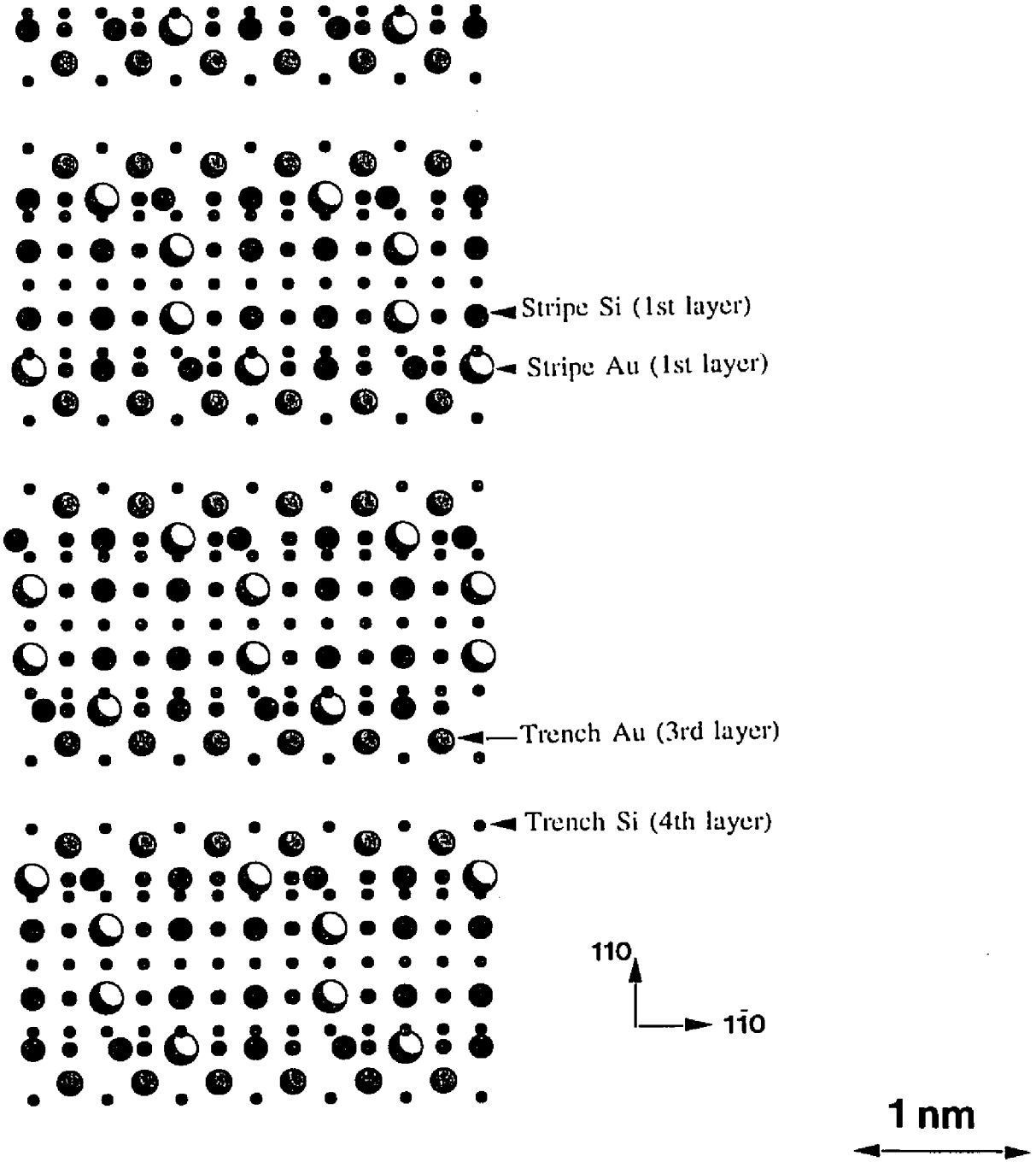

Figure 4.20. (b) Schematic of the top view of the B type domain of the √26x3 surface cell. This domain is related to the domain in Figure 4.20 (a) by a mirror reflection. Note the phase slip between adjacent stripes: Au rows line the trench and also substitute for B-type features in the STM schematic[149].

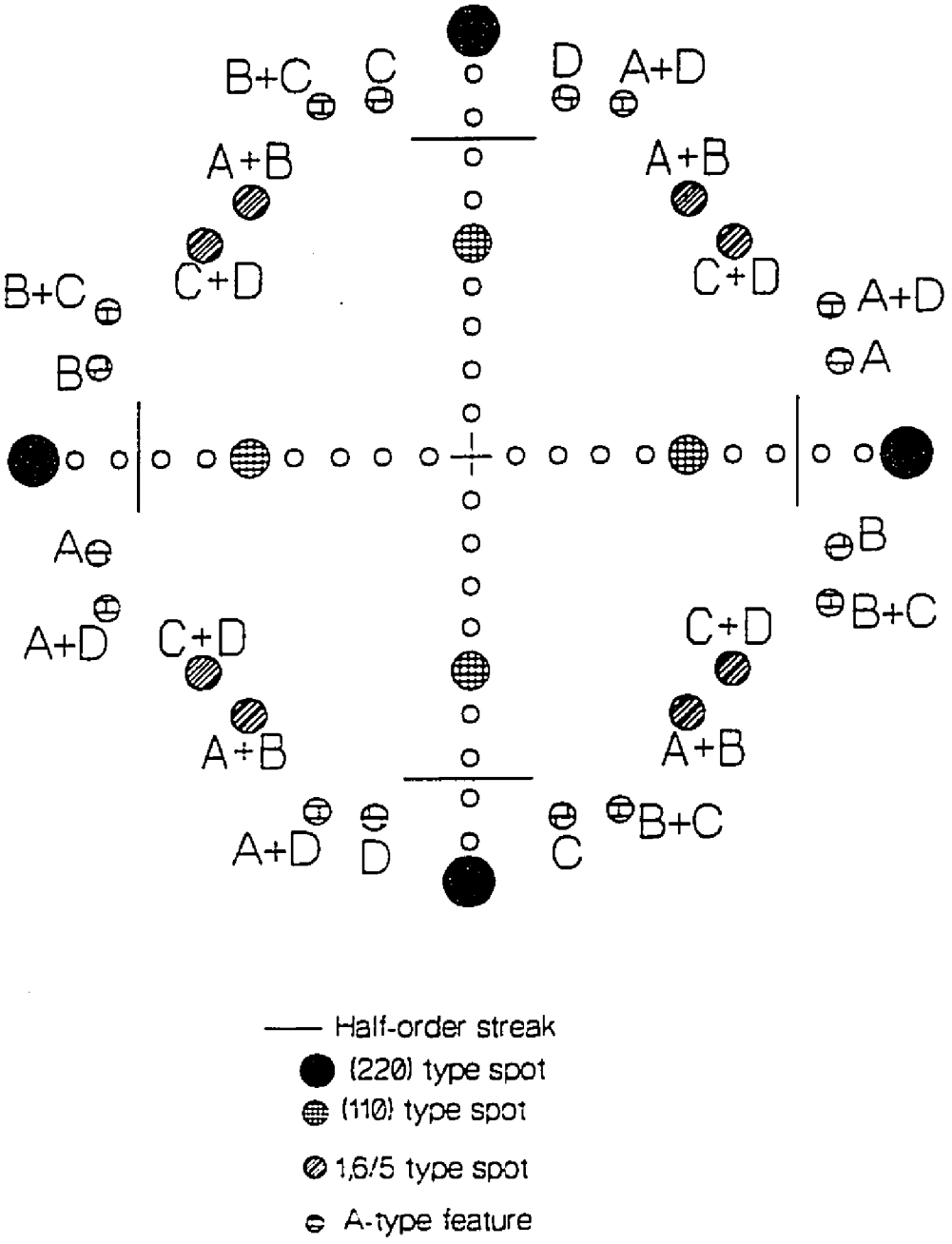

Figure 4.21. Schematic of the diffraction pattern in Figure 4.14, with the letters A and B indicating the contribution of the corresponding domains in Figure 4.20; C and D represent domains obtained by rotating the A and B type domains shown in Figure 4.20 by 90° (across a single layer high step).

It should be noted that both the 5x3 or $\sqrt{26}$x3 geometries gave similar intensities for the 1,6/5 type spots implying that a mixed surface phase of the two structures as suggested by the STM study is possible. Since the models have to satisfactorily explain HREM data, the latter were used as a means to check the consistency.

The Consistency Check

Forward calculation of the HREM images was carried out for each of these models and the simulated images were compared against the envelope-corrected images for the corresponding defocus settings (e.g., Figure 4.16). Such image comparisons clearly revealed a preference for the model of the stripe in which Au atoms substituted for the four B-type features and Si atoms for the other eight A-type features, for the following reasons:

a) Interchanging the number of Au and Si atoms resulted in very strong contrast in the simulated images, which did not agree well with experimental data. Figure 4.22 shows images simulated for the two cases to illustrate this point (the anisotropy in beam convergence, due to beam drift during the imaging process, results in the directionality at 45° to the Au-rows).

b) A total of ten Au atoms in the surface cell (four in the surface layer and six in the two rows in the third layer in the trench) would result in a fractional coverage of 0.67 ML per surface unit, in good agreement with the value of 0.7ML predicted by XPS[149].

It should be noted that an inherent assumption in the analyses is that the outermost rows move towards the center of the stripe based on STM data. The inter-Au row

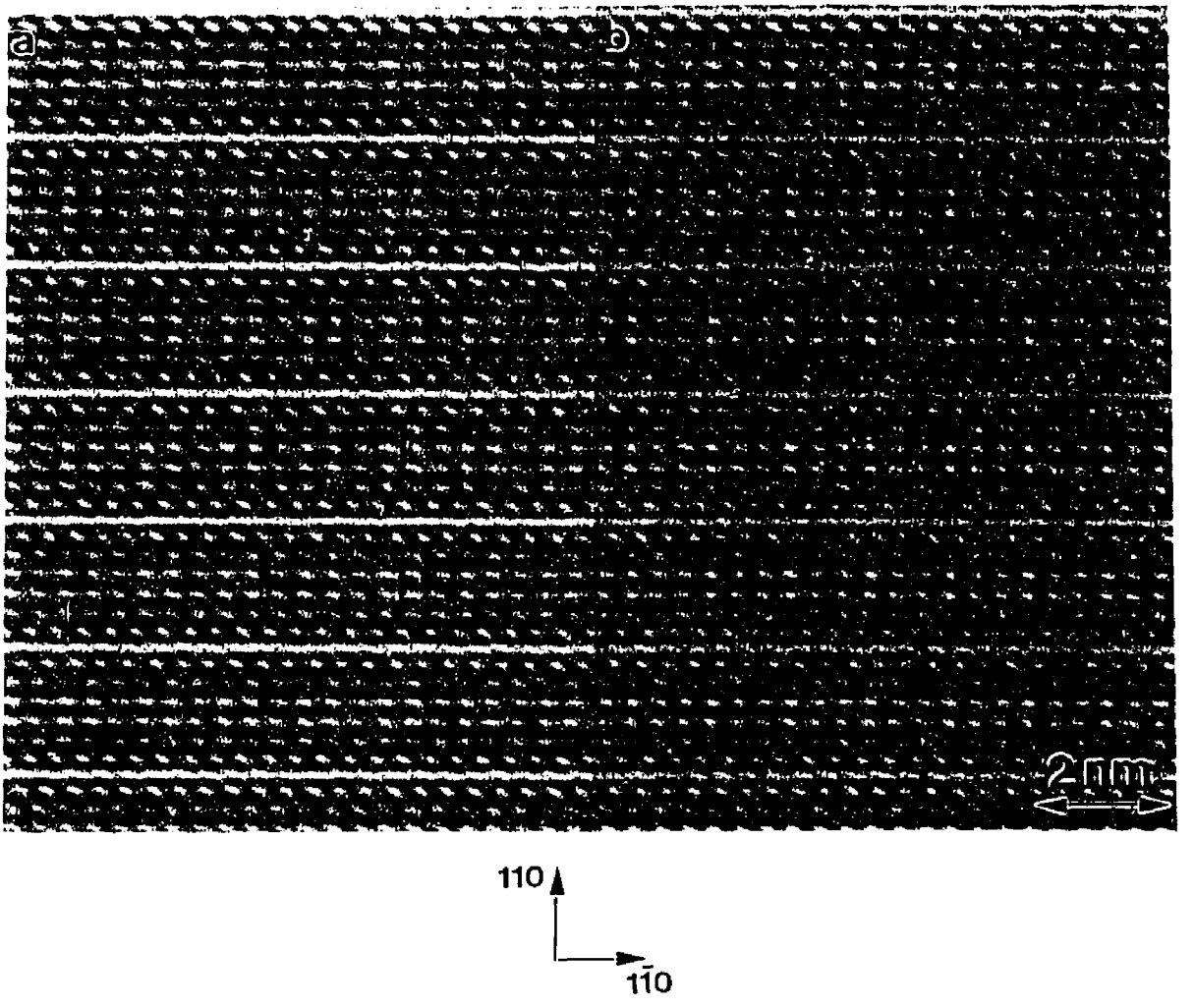

Figure 4.22. Montage of HREM images simulated for the 5x3 cell, (a) with Au distribution on the stripe as in Figure 4.19 and (b) with Au and Si interchanging stripe positions shown in Figure 4.19. The directionality in the images arise due to anisotropy in the beam convergence in the simulations.

spacing of 1.5α represents an expansion relative to the bulk Si positions. Translating this to the outer rows on the surface, the resultant spacing between the four Si surface rows would be 2.5α rather than 3α. The associated surface layer compression of 16.7% is in good agreement with the 17% value reported in the STM study[149].

4.3.4 *Discussion*

The behavior of Au on clean Si(001) surfaces, both at room temperature and on annealing, can be explained on the basis of a stress-relief mediated mechanism. This behavior is directly related to the inherent nature of the clean Si(001)-2x1 surface. It is well known that the Si(001)-2x1 surface is under a strong tensile stress parallel to the dimer bond[188]. (The tensile stress results because the dimerization favors compressive substrate strain parallel to the dimer bond; however, a rigid bulk lattice places the surface under a strong tensile stress[191]), and each atom involved in the dimerization still has an unsaturated dangling bond.

Au deposition at room temperature results in the transition of the clean 2x1 structure back to the ideal bulk-like 1x1 structure and can be attributed to the saturation of this dangling bond by a deposit Au atom (rather similar to the results on Ag deposition). The STM study[189] revealed the saturation coverage for this surface to be 1 ML of Au (and reported a layer by layer growth for values up to 3 ML). However, the phase map[146] suggests that the (1x1) surface structure continues to exist at coverages exceeding this value; in fact, a weak silicide ring is reported to be detectable only at 3nm

Au deposit thickness. The excess Au (above the saturation value) could thus be accommodated either on the surface itself or in the bulk. In case of accommodation in the Si bulk lattice, the bulk material would be strained in the Au-containing region due to the differences in the radii of the two species.

Annealing the system would provide a mechanism for the release of this strain via rearrangement of atoms, both on the surface and in the bulk. The final surface structure resulting from this process, i.e., the Si(001)-Au-5x3 phase, is thermodynamically favored based on both the phase map[146] and other studies[145,149], and can be completely described on the basis of the surface stripe, the sub-surface trench, and the single missing row of atoms, see Figures 4.19 and 4.20. This missing surface row can be visualized as a "surface dislocation". The term was first defined to describe the formation process for the Si(111)-7x7 surface[192], and was recently invoked to explain the structure model for the Si(111)-Au-5x2 structure[193].

While the current investigation does not provide data on the actual origin of the dislocation, the latter has to be directly related to the sub-surface Au-row expansion. Such an expansion would place a compressive stress on the surrounding silicon layers in the rigid bulk lattice. Translation of this stress to the surface layer would result in the compression of the outer two rows on the stripe, of magnitude equal to that of the expansion of the sub-surface rows.

A few points of caution about the model:

1) The structure models proposed in the study (i.e., 5x3 and $\sqrt{26}$x3) assume an ordered arrangement of pure Au and Si atoms. The presence of a gold-silicide compound can

however not be ruled out, and in fact, small amounts might even be present, although their contribution to the features in the TED patterns is unknown.

2) Further, since transmission data are highly sensitive to positions in the plane orthogonal to the incident beam, the intensity of the 1,6/5 spot changes with small displacements in the x-y plane. The current structure results therefore, are intended to only serve as a qualitative description of the atom distribution. More rigorous quantitative calculations (involving R-factor and χ^2 tests) would be required to predict the exact atomic structure.

3) Finally, the relative insensitivity of these data to the positions along the beam direction (z) implies that techniques such as X-ray standing wave and LEED would therefore be better suited for determining these locations.

5. THE GaAs(001) SYSTEM

Following their success in yielding a Si(001)-2x1 surface, the *in situ* techniques were employed in the GaAs(001) system for surface structure and metal-deposition studies; surface preparation via MBE was also recently attempted in the SPEAR. Although neither route resulted in a clean GaAs(001) surface to date, a brief literature review of the current understanding in this regard is presented below for sake of completeness.

5.1 Background

5.1.1 *Clean Surface Structure*

The primary driving force governing the reconstruction of GaAs(001) surfaces is identical to the one operating in the Si(001) case, i.e., saturation of the surface dangling bonds, and minimization of the surface and subsurface strain associated with this process. The notation used in describing the surfaces, however, is dependent on the identity of the terminating species. For example, the Ga-terminated surface is designated the (001)-Ga surface, while the As-terminated surface would be indicated by the bar notation[3], i.e., the (001)-As surface.

Also, similar to the Si(001) system a variety of surface structures have been observed on both the Ga- and As-terminated (001) surfaces depending on the processing history of the surface[194,195]. Among these are the (1x6), (4x6), and c(8x2) type

reconstructions for the Ga-terminated surface, and the c(4x4) and c(2x8) structures for the As-terminated surface[196-199]; the commonality in these cases is the dimerization of the surface atoms. A complicating factor in these studies is that for many of the surfaces, the actual surface coverage is not precisely known[194,200,201].

5.1.2 *Au-GaAs(001)*

Most studies to date on the Au-GaAs(001) system have focussed on the chemical characteristics of the interface (structurally, films are polycrystalline) as a function of substrate temperature, deposition conditions, etc. While no reaction, i.e., an abrupt interface, is reported on Au deposition at room temperature[202-204], a different study[205] reports intermixing resulting in the formation of a 50/50 Au-Ga mixture on the surface of the deposited Au film. A possible explanation is the cleanliness of the substrate surface, e.g., an atom probe study has shown that Au deposited on clean GaAs(001) surfaces intermixes with the substrate, while no such reaction occurs on an oxide-layer coated surface[206].

Annealing the system results in two morphological changes: better texture and alloy formation; the latter from an increase in the rate of dissolution of Ga and As through the contact metallization. Depending on factors such as annealing temperature, coverage, etc. alloys of differing compositions are observed, e.g., Au_7Ga_2[202,207-209], Au_2Ga[203], Au_3Ga[204] and α-(Au-Ga)[203,204,208,209]. Further, these compounds have specific orientation relationships with the substrate, e.g., rectangular protrusions and pits with

edges aligned along the <110> directions of the GaAs substrate are reported[203,209,210].

The two HREM[203,204] studies on this system suffer from the drawbacks associated with conventional investigations as described in Chapter 2, i.e., Au deposition on the GaAs(001) substrates in both cases was *ex situ*, and transfer into the TEM was under non-UHV conditions; the influence of transfer environment on the final observations was thus unknown. The importance of UHV conditions (as emphasized from the Ag-Si(001) study) is underlined from results of a study on the Au-GaAs(110) system[211]. Annealing Au deposited on air-exposed substrates resulted in large metallic protrusions extending several tens of nanometers into the interface, while flat abrupt interfaces were seen on annealing Au deposited on clean substrates.

An attempt was therefore made to characterize the structural aspects of the interface created by deposition of a few monolayer of Au, both at room temperature and on annealing, as a function of substrate "cleanliness"; in the process, the success of the preparation routes in yielding reconstructed GaAs(001) surfaces was evaluated.

5.2 Experimental Results

5.2.1 *Surface Preparation*

Samples were prepared in the *ex situ* stage of the experiment by etching in either one of the three different solutions described earlier in section 2.5.1. Of the three, the one containing bromine etched the fastest but was also the least desirable from the point of research safety. Instead, the one containing sulfuric acid proved to be the most

effective since samples prepared via this route showed the least hydrocarbon contamination; a small amount was, however, still present in these cases. These samples are therefore termed "dirty", while ones subjected to *in situ* ion mill-anneal cycles inside the UHV-SSC (till no carbon or oxygen peaks were detected in the PEELS data) are termed "clean" in the remainder of the chapter.

5.2.2 *The GaAs(001) Surface*

A bright field image of a dirty sample is shown in Figure 5.1(a); the morphology is relatively featureless. On the other hand, numerous 3D islands were observed in the clean samples, as shown in the (220) type dark field image in Figure 5.1(b).

Based solely on these images, it is not possible to comment conclusively on their identity. However, in light of the surface treatment it can be hypothesized that the islands are of gallium. Arsenic loss could result either due to preferential sputtering or from sublimation, the latter due to annealing in vacuum. Even in cases where the annealing was conducted in a backpressure of arsenic, as for bulk samples in the MBE chamber of the SPEAR, 3D islands resulted possibly due to some combination of excessively high temperature and insufficient arsenic backpressure. A SEM image of these islands (larger in size than those seen on the TEM samples) is shown in Figure 5.2(a) and the AES data from the islands, and the regions in between, in Figures 5.2(b) and (c) respectively. The spectra confirmed the hypothesis that Ga islands dominate the surface morphology of the "clean" samples; results from Au deposition on to these surfaces are presented below.

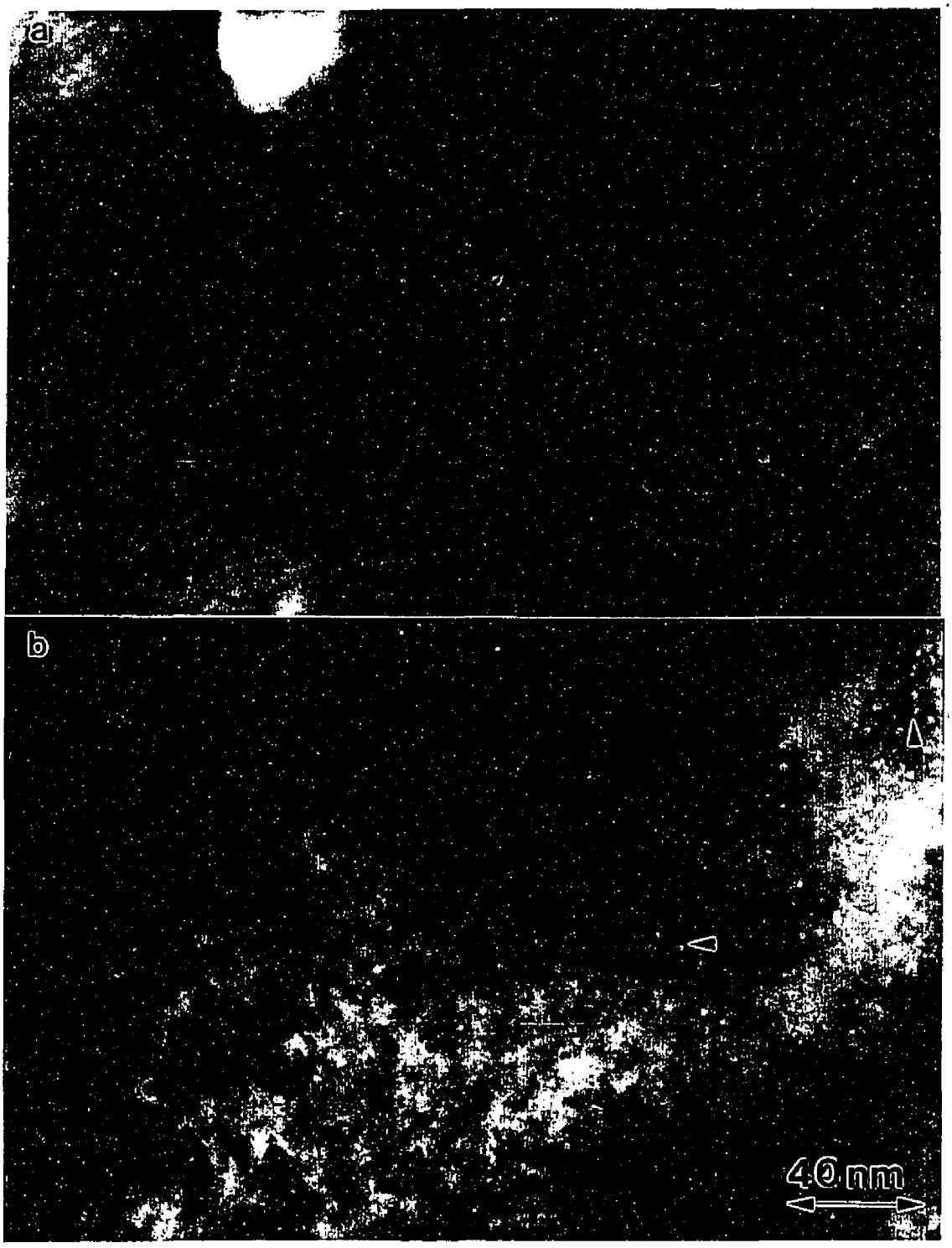

Figure 5.1. (a) Bright field image of the dirty GaAs(001) sample showing a relatively featureless morphology. (b) A (220) type dark field image of the "clean" GaAs(001) sample showing 3D islands of possibly gallium (arrowed).

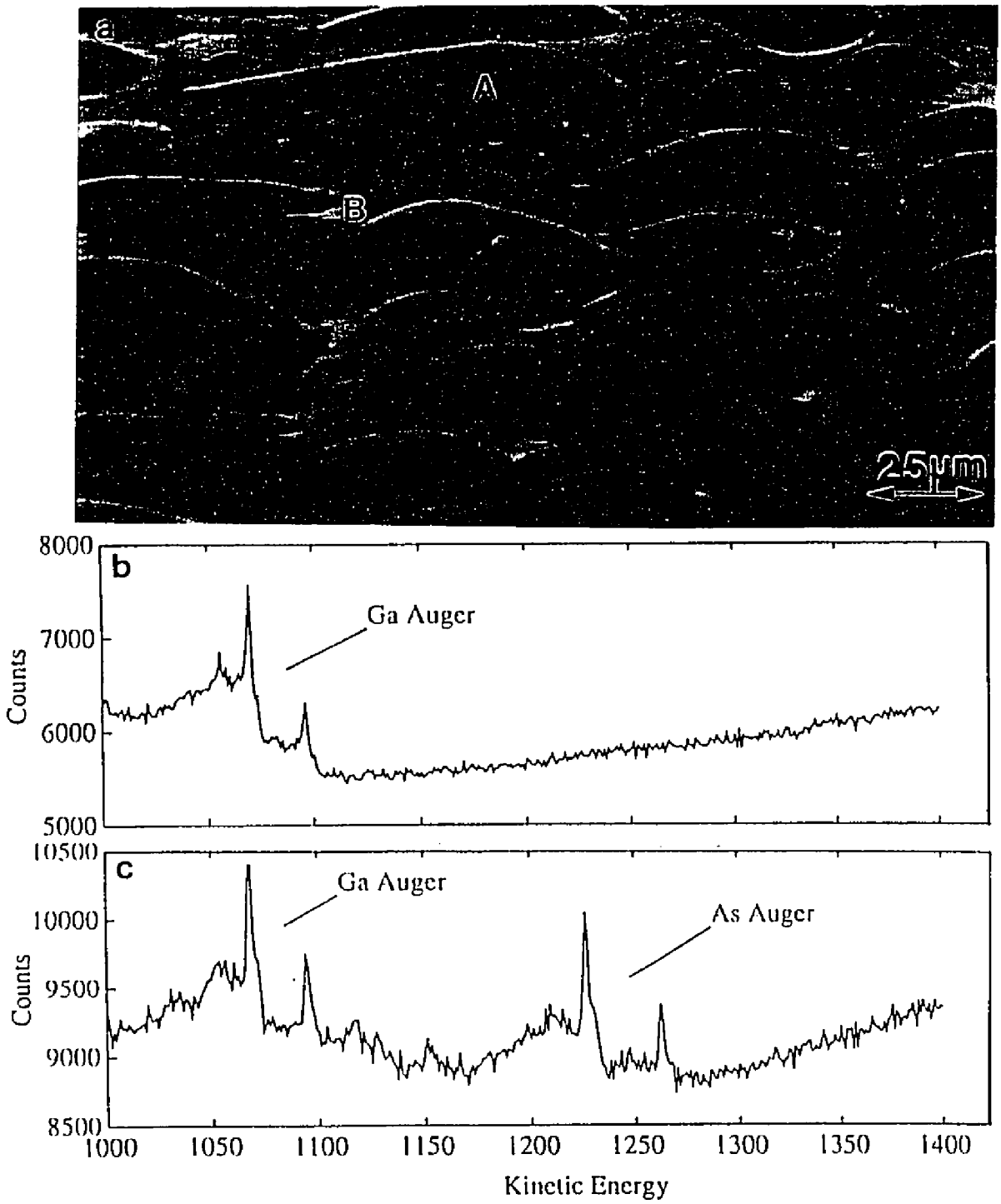

Figure 5.2. Morphology of a bulk sample subjected to an excessive temperature anneal in insufficient arsenic backpressure. (a) SEM image shows 3D islands on the surface. AES collected from an island (marked **A** in (a)) and the regions in between (marked **B** in (a)) are shown in (b) and (c) respectively. The islands are seen to be of gallium.

5.2.3 *Au on "clean" GaAs(001)*

Room Temperature Behavior

TED patterns recorded following a few monolayer of Au deposition on to the "clean" sample at room temperature showed a sharp polycrystalline ring with a spacing corresponding to that of Au(111). This suggested that the Au growth was highly textured, and also, that the interface was abrupt in nature. One such pattern is shown in Figure 5.3.

A XPS spectrum, collected following Au deposition on the bulk sample in Figure 5.2(a) is shown in Figure 5.4(a), and confirmed the hypothesis made on the basis of TED data, i.e., that Au had not reacted with GaAs. On increased deposition, each Au peak was seen to split into two peaks: one which stayed at the same location, and the other that was shifted by ~1.2eV in binding energy to the left of the pure Au peak (i.e., towards higher binding energies), as shown in Figure 5.4(b). This splitting suggested that intermixing of the deposit-substrate components occurred at room temperature itself (above a certain coverage). Having established that the reaction commences at room temperature itself, the next step was to study its evolution as a function of temperature.

Annealing Behavior

Figure 5.4(c) is a XPS spectrum collected from the annealed bulk sample; and showed only two peaks, in contrast to the four peaks in (b); each of these was shifted by ~1.2eV to the left of the pure Au peaks in Figure 5.4(a) suggesting that the alloying mechanism, which had started at room temperature, was now complete.

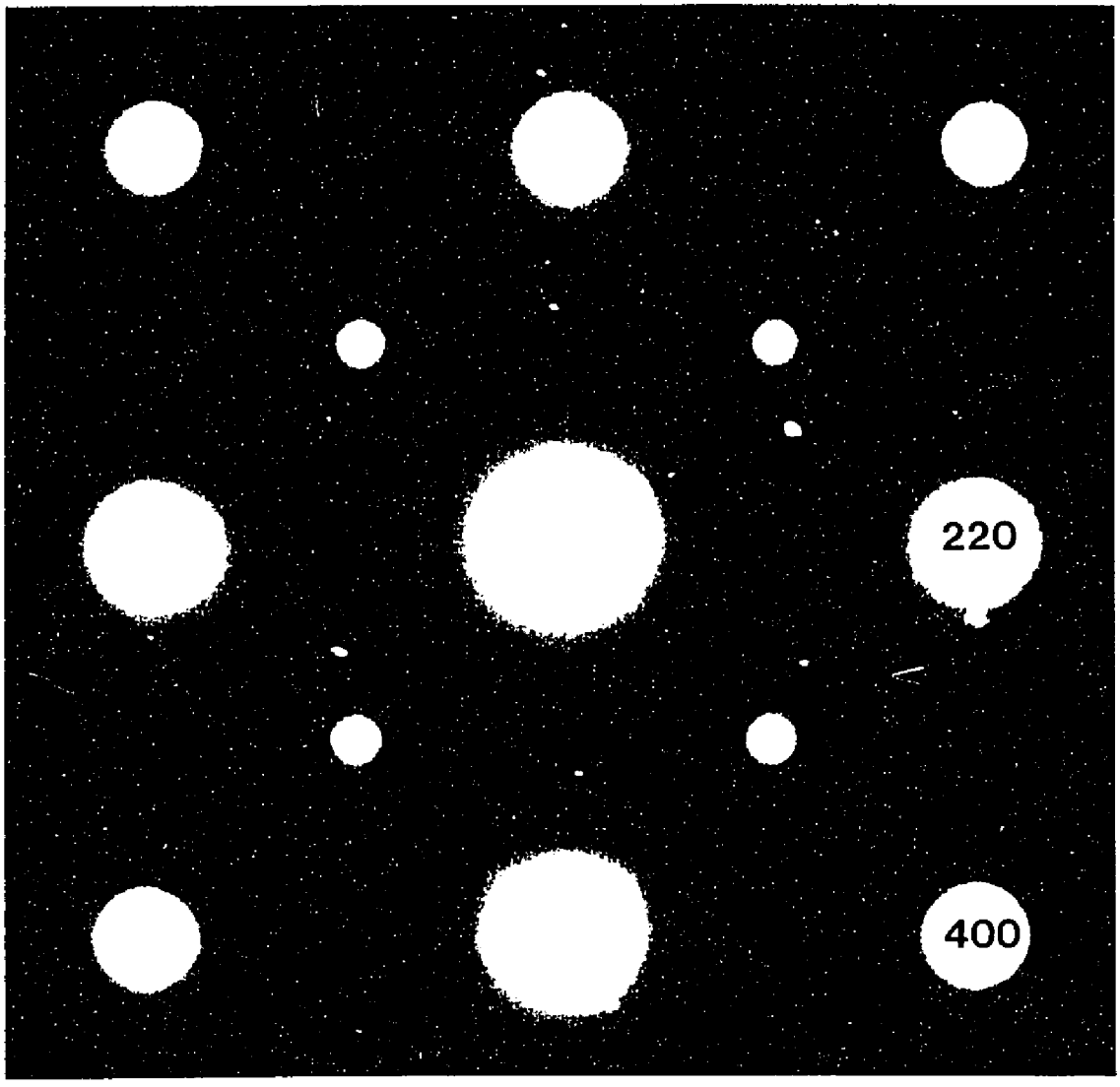

Figure 5.3. A TED pattern following room temperature Au-deposition on to the GaAs(001) surface in Figure 5.1(b). The sharp (111) ring of Au, arrowed, suggests the textured growth of the deposit and the abruptness of the interface; bulk GaAs reflections are indexed for reference.

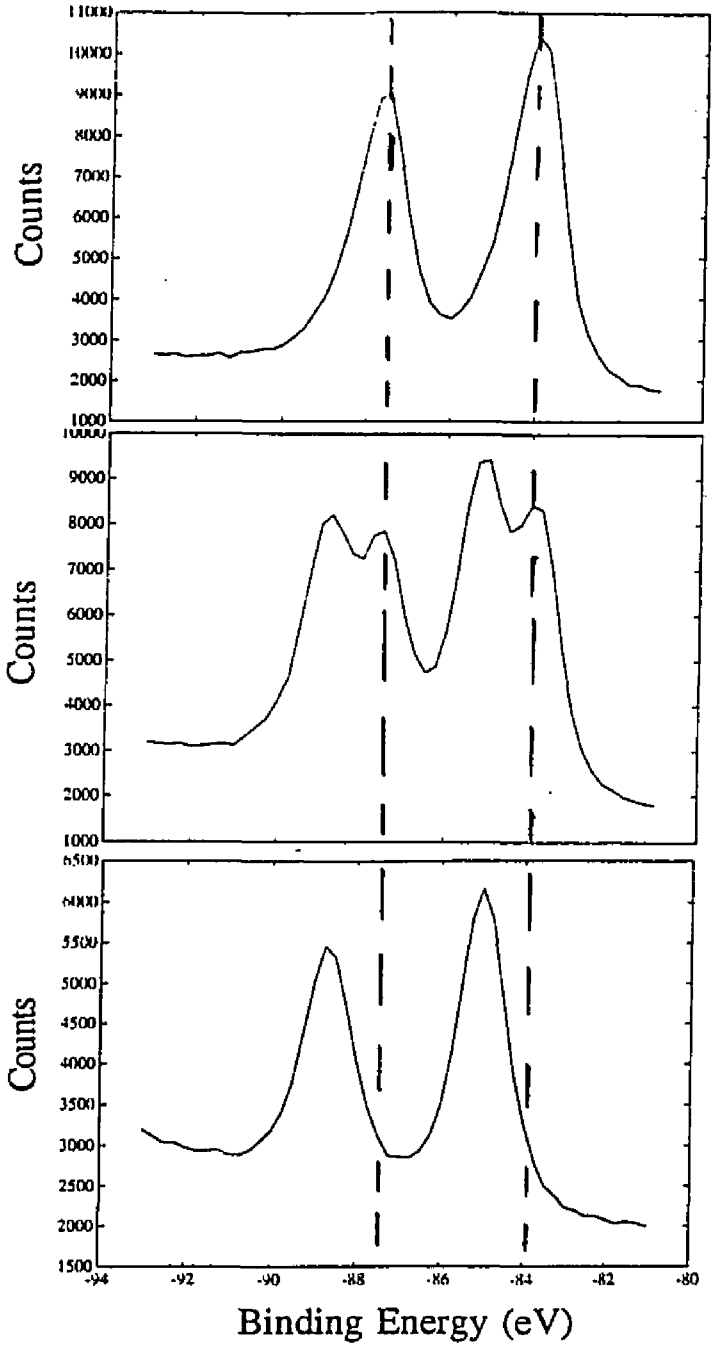

Figure 5.4. (a) XPS data from Au deposited on to the surface in Figure 5.2(a) reveals the abrupt nature of the interface. (b) XPS data collected following additional Au deposition on to the surface in (a) shows splitting of the pure Au peaks, suggestive of intermixing at the interface at room temperature beyond a critical thickness and (c) XPS data following annealing of the surface in (b), indicating completion of alloy formation at the interface. The common vertical line passes through the pure Au peaks, for reference.

TED patterns and images recorded from samples following similar anneal treatments revealed some very interesting characteristics. The polycrystalline ring seen following room temperature deposition had disappeared, and instead, sharp "satellite" spots appeared around the GaAs bulk reflections. These features are readily apparent in the TED pattern shown in Figure 5.5(a). The geometry of the spots shows that the phase responsible for their origin has a cube-cube epitaxy with the GaAs(001) substrate. Using the satellite spots that were the strongest in intensity as the basis, this phase was identified as $AuGa_2$; the alloy has a face-centered cubic structure and a lattice parameter of 0.607 nm. Figure 5.5(b) is a schematic construct of the TED pattern in Figure 5.5(a) showing only the bulk GaAs and the primary $AuGa_2$ reflections. The other extra spots in (a) arise from double diffraction. The phase identification was also confirmed from the results of an earlier XPS study: the binding energy of $AuGa_2$ was reported[212] to be higher than that of pure Au by 1.3eV.

The corresponding morphology of the alloyed material was revealed from bright-field, dark-field images and one such pair is shown in Figure 5.6. Both rectangular and square islands with edges parallel to the <110> directions of the substrate were clearly seen with the rectangular islands dominating the morphology. The islands in Figure 5.6(a) showed moiré fringes arising from the interference between the transmitted beam and the alloy reflections around it inside the objective aperture; in addition, some strain /thickness contrast could also be discerned in these particles. To understand the 3D structure of these particles in greater detail, dark field images were recorded using weakly excited Bragg reflections; Figure 5.6(b) is a (220) type dark field image recorded under

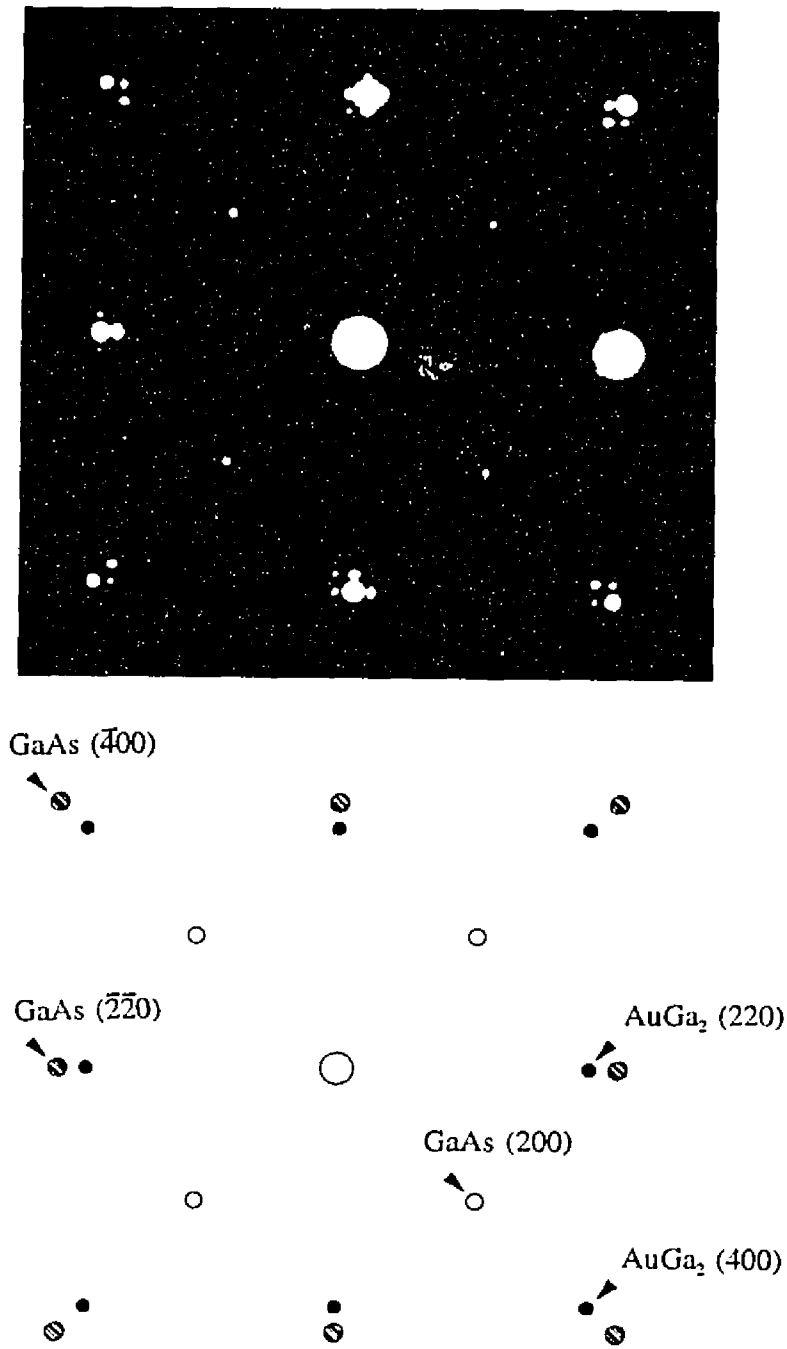

Figure 5.5. (a) A typical TED pattern after annealing the sample in Figure 5.1(b). Note the satellite spots around the bulk GaAs reflections. (b) A schematic of the TED pattern in (a), with the satellite spots indexed (arising due to $AuGa_2$).

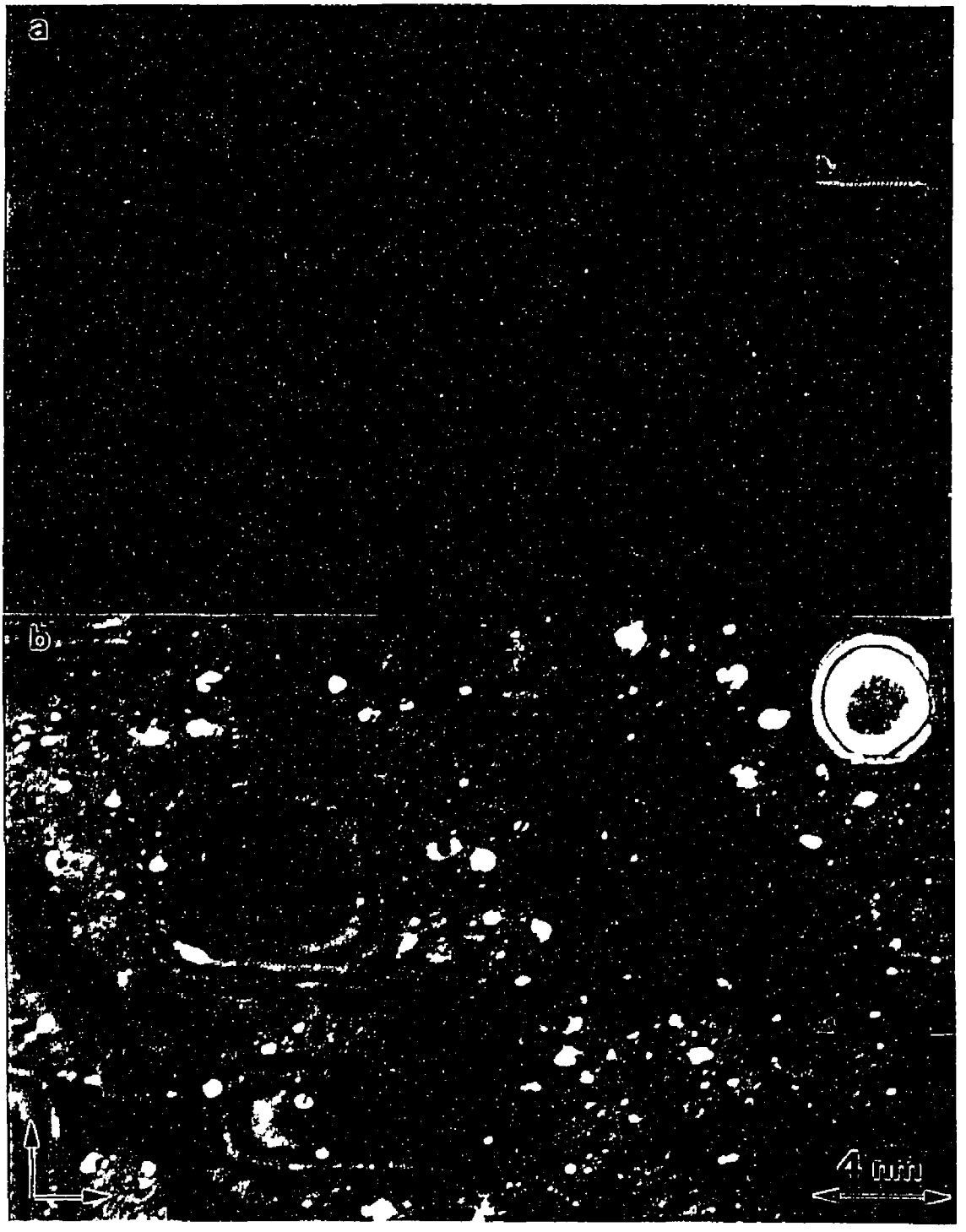

Figure 5.6. (a) Bright field image of the region from which the TED pattern shown in Figure 5.5(a) was recorded. The rectangular shape of the $AuGa_2$ islands and the moiré fringes in them are apparent. (b) A (220) type dark field image reveal the pyramidal morphology of the 3D islands. Arrows in the left corner denote the <110> directions.

these conditions and reveals equi-thickness fringes (contrast arising from inhomogeneous strain[166]), which indicate a square pyramidal morphology.

5.2.4 *Au on "dirty" GaAs(001)*

Room Temperature Behavior

The behavior of a few monolayer of Au deposited on to the dirty sample at room temperature was identical to that on the "clean" substrates, i.e., TED patterns showed a polycrystalline Au(111) ring.

XPS data recorded from similar deposition on to dirty surfaces of the bulk samples also showed peaks of pure Au, confirming the absence of any reaction at room temperature in the initial stages of deposition. Unlike the behavior on "clean" surfaces, however, no peak splitting or shifting was ever observed on increased deposition suggesting that the interface remained abrupt in nature.

Annealing Behavior

The microstructure of the deposits following anneal cycles, as revealed by bright field - dark field images, was very similar to that shown in Figure 5.6, i.e., mainly rectangular islands with edges parallel to the <110> directions of the substrate. No extra spots were seen in the corresponding TED patterns, thus suggesting the absence of a reaction with the substrate. XPS data recorded following annealing of Au deposited on to dirty bulk samples supported this observation.

5.3 Discussion

The failure of the *in situ* ion mill-anneal cycles in an UHV environment in clean surface preparation is not surprising since clean GaAs(001) surfaces are typically prepared by annealing the sample in a backpressure of arsenic[196-199]. However, TEM samples subject to such treatments inside the MBE chamber of SPEAR also failed, to date, to show any reconstruction; possible reasons are the non-uniformity in heating and insufficient arsenic backpressure. In fact, these samples had a dull lustre (in contrast to the shiny surfaces prior to treatment), rather similar to the bulk wafers subjected to an identical treatment (which resulted in islands of Ga).

These factors in combination suggest that the only possible route to preparing clean GaAs(001) surfaces is via heating in an arsenic atmosphere under proper time-temperature-arsenic backpressure boundaries. Further, the rate limiting step to preparing clean GaAs(001) surfaces (which also holds true for other systems) is the sample cleanliness following the chemical etch. This is very crucial since XPS and AES data collected from the as-etched sample surfaces always reveal carbon and oxygen. While oxygen leaves the surface as arsenic oxide (when the sample is annealed in the arsenic backpressure), carbon removal always requires milling of some form (which might preferentially sputter the components, aside from increasing the defect density in the material). Surface carbon contamination can be reduced by using doubly distilled water to clean the beakers used for the chemical etch, and also, to prepare the etchant solution.

The main conclusions arising from this study about Au behavior, in both the room-

temperature and high-temperature regimes are:

1) The existence of a critical thickness value above which Au starts to react with the contaminant-free substrate at room temperature; rather similar to its behavior on clean Si(001)-2x1 surfaces at room temperature[141-144]. Such a reaction results in a partial conversion of Au to $AuGa_2$, as revealed by the XPS peak splitting. The absolute value for this critical coverage cannot be commented on, however, due to lack of quantifiable deposition data. On annealing, any remnant Au also transforms into the face centered cubic $AuGa_2$ phase. The specific alloy formation in the two temperature regimes can be explained on the basis of the phase diagram reported in an earlier study[208] (and reproduced in Figure 5.7). Since $AuGa_2$ is the terminal gallium-rich solid solution, it can be expected to form considering the Ga-island surface morphology of the substrate prior to Au deposition (this also explains the reason why the critical thickness issue has not been commented on in the literature). This implies that the appearance of this alloy can be used to gauge the initial stoichiometry of the substrate surface.

2) The lack of alloy formation in case of Au deposited on to carbon and oxygen covered GaAs(001) surfaces either at room temperature or following high temperature anneal treatments suggests that the contaminant layer blocks the intermixing between the substrate and deposit components. In combination with (1), the results are in good agreement with the predictions of the atom probe study[206].

3) Rectangular islands of either Au or $AuGa_2$ result in these cases with preferred orientations relative to the substrate; the following epitaxial relationships were observed:

$AuGa_2$ (001) // GaAs (001) and $AuGa_2$ <110> // GaAs <110>

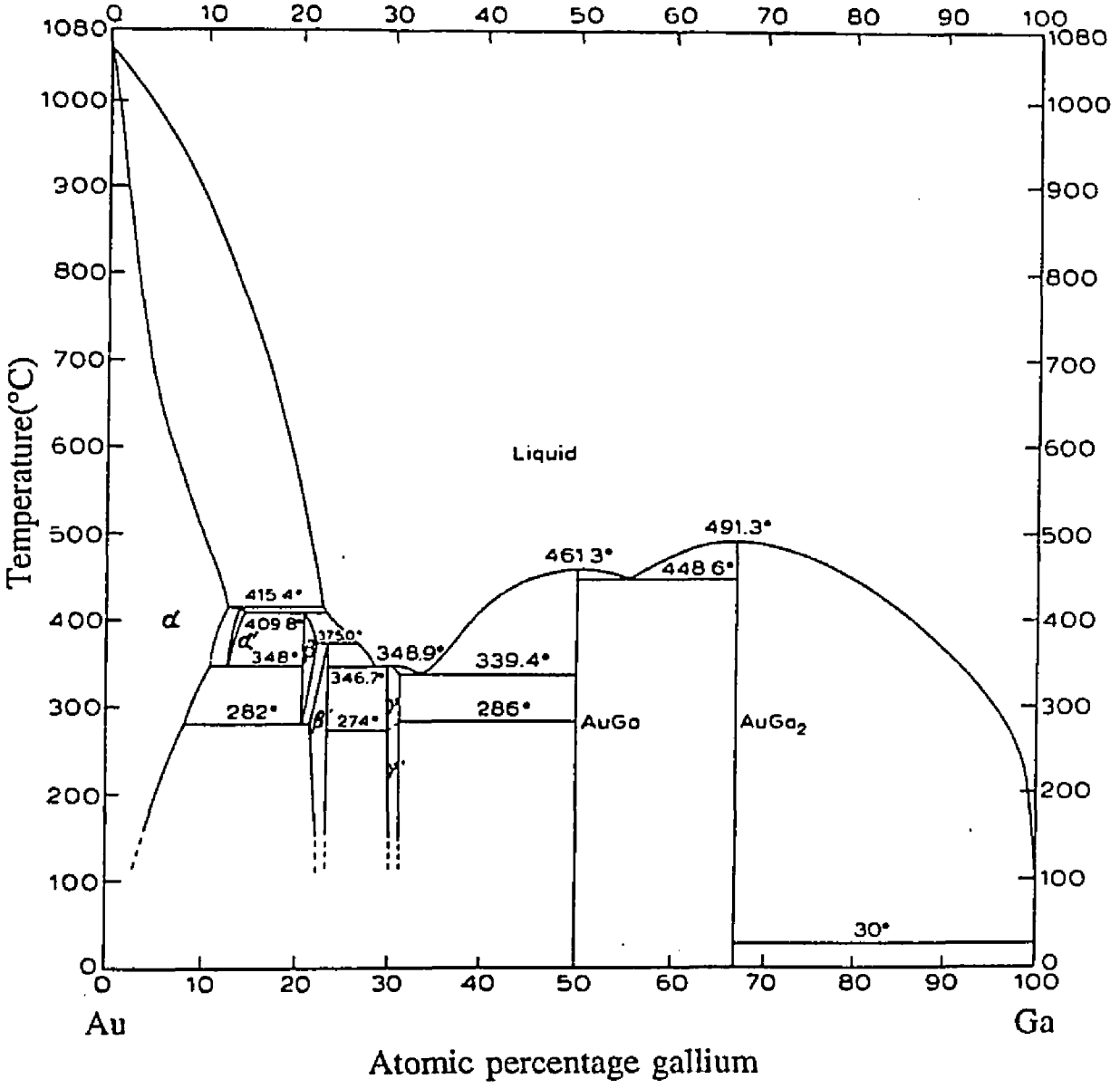

Figure 5.7. Phase diagram for the Au-Ga system (adapted from Beam, E.; Chung, D. D. L. *Thin Solid Films* **1985**, *128*, 321).

Au(001) // GaAs (001) and Au<110> // GaAs <110>

This final morphology evolved following numerous annealing cycles under UHV conditions with an increase in island size paralleling any temperature increase between successive sequences. Also, the aspect ratio for these rectangular islands was higher on an average along one of the substrate <110> directions. Since a similar behavior has been observed for rectangular patches and holes by earlier SEM studies[203,209,210], the morphology is probably linked to the differing reactivity of the substrate component planes due to the polar nature of the GaAs(001) surface.

6 MoS_2 THIN FILMS

6.1 Introduction

Lubricants are used in most surface science instrumentation (including the UHV-TEM, UHV-SSC, and SPEAR) to ensure that moving components do not suffer from mechanical seizure, especially due to repeated bake-outs. The two main criteria for lubricant selection for these vacuum applications are high temperature insensitivity and low vapor pressure; the latter to minimize outgassing under operating conditions[213]. In general, solid lubricants meet both these criteria better (and also have lower friction coefficients, on average, in vacuum) than the liquid and grease alternatives. Lamellar solids in particular, for example, disulfides of Mo, W, etc. are prime candidates for these applications by virtue of their crystal structure and the associated bonding[213,214]. Of these, molybdenum disulfide is the one that is most commonly used in both terrestrial and space vacuum applications.

The lubricating action of MoS_2 is due to its low shear strength, which enables the material to deform plastically more readily than the solid surfaces between which it is placed. This macroscopic quality (i.e., the shear strength) is linked on the atomic scale to the material's anisotropic crystal structure and bonding. MoS_2 is hexagonally packed and consists of a layer of Mo bounded on either side by a layer of S as shown in the schematic in Figure 6.1. Strong covalent bonding exists inside the layer (also called basal plane), while weak Van der Waals forces of attraction bond the adjacent layers. The

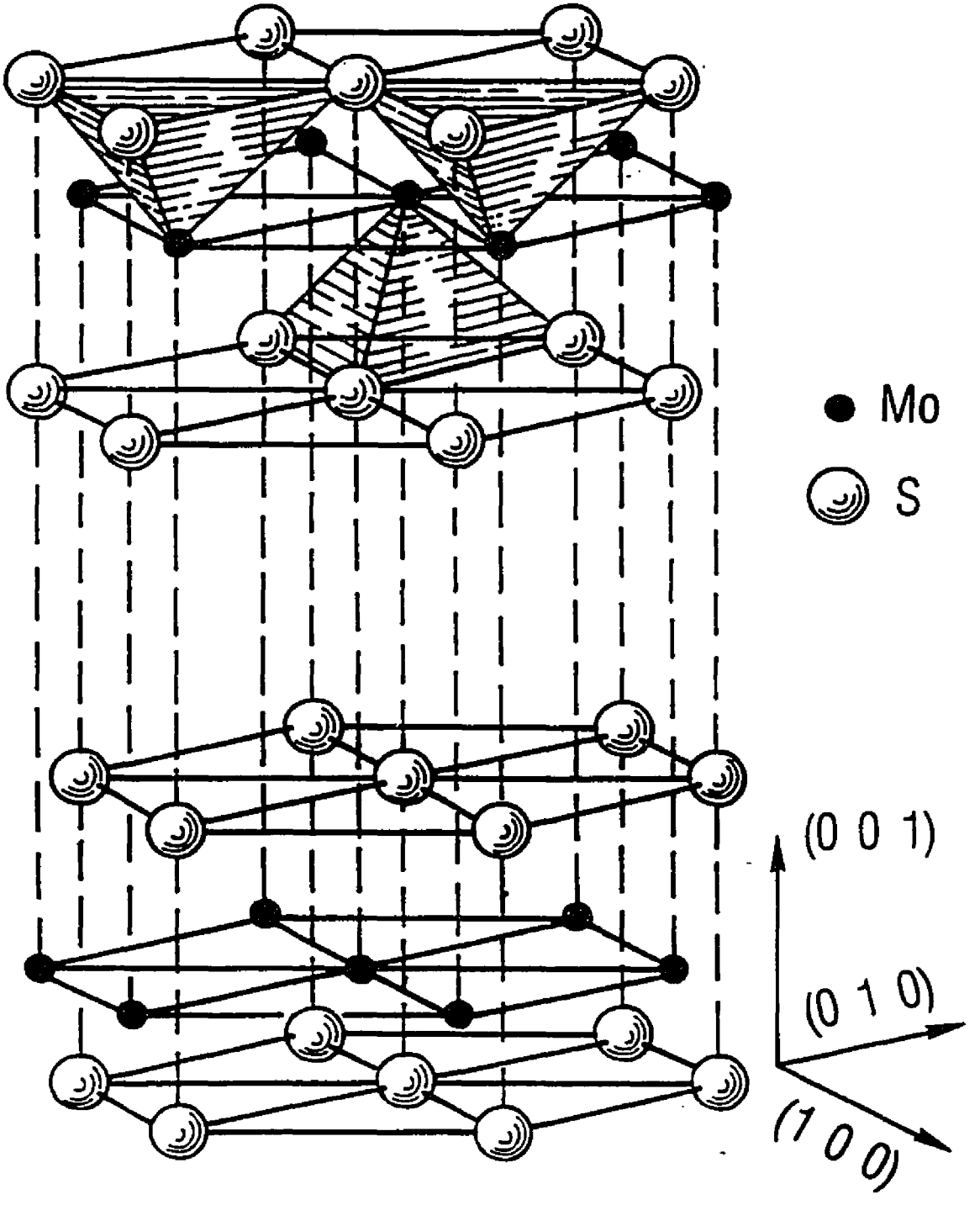

Figure 6.1. Schematic of the crystal structure of MoS_2 (adapted from Hilton, M. R.; Fleischauer, P. D. *J. Mater. Res.* **1990**, *5(2)*, 406)

material can therefore slip rather easily on application of shear across these basal planes resulting in good lubrication properties in this direction. The ideal morphology would therefore consist of these basal planes parallel to the surfaces of contact. Rather analogous to the surface structures described in the earlier chapters, the final microstructure and morphology of the MoS_2 film depend strongly on the film preparation/ deposition conditions.

Conventionally, MoS_2 is deposited either as burnished, bonded, or sputtered films. The need for long-endurance, thin solid lubricant films for precision mechanisms in spacecraft led to the development of the sputter-deposition technique for growth of MoS_2[215] (while bonded films are generally most commonly used, sputter-deposited ones are employed in precision mechanisms aboard spacecraft). The first generation of these films had a microstructure that resulted from competitive nucleation and growth between the basal-plane (i.e., the (001) planes) and edge-plane oriented grains (i.e., the (001) and the (110) planes)[216,217].

In general, pure sputter-deposited MoS_2 films have a porous, columnar plate morphology with an edge-plane preferred orientation parallel to the substrate surface. However, these columnar plates are in the wrong orientation for lubrication, and tend to detach near the film-substrate interface and reorient into lubricating particles early in operation[215,218,219]. It was recently reported that spallation of MoS_2 films occurred over large areas of contact, generating large debris in addition to the smaller debris of the reoriented columnar grains[220-222]. Such spallation occurred early in rolling element bearing tests resulting in unacceptable torque noise[223]. Although it is now accepted that MoS_2

films lubricate by intercrystalline slip[224], the generation of significant film debris early in contact is undesirable. This is because long endurance becomes dependent upon the retention or recirculation of the film particles in the contact zone, rather than on the gradual wearing away of the film. In addition, the edge-plane orientation also enhances the formation of MoO_3 when MoS_2 is stored (or worse, operated) in humid air[225,226]. This oxide has significantly lesser endurance and a higher friction coefficient than MoS_2[227,228]. Experiments have shown that basal-plane orientation and large grain size partially inhibit MoO_3 formation in humid environments[225-228].

The need to minimize early debris generation in rolling contact applications led to the development of a second generation of sputter-deposited MoS_2 films[213]. These films generally have denser morphologies and more basal plane orientation because the growth of edge facets is slowed or suppressed; the latter is accomplished by incorporating dopants (Au-(20%)Pd, Ni, SbO_x) as co-sputtered species or as multilayers[229-231]. Adjusting deposition conditions, i.e., substrate temperature, low pressures, etc. also promote the denser microstructure[232-235]. While the role of these different parameters in controlling the final nanostructure of the film is reasonably well-understood, detailed investigations on this subject are, however, far from complete.

In particular, the morphological distribution of metal dopants in the newer co-sputtered and multilayer films has not been well-characterized, and the relationship of these nanostructures to the tribological performance and humid storage stability is not well understood. Further, an understanding of the relationship between the structural and chemical stability of the films as a function of the initial film microstructure on the

atomic scale is lacking. The following sections present results from studies carried out to resolve these issues. The effect of substrate temperature and metal dopant incorporation during film deposition on the final microstructure of MoS_2 was investigated in great detail. The stability of the films (deposited on substrates held at two different temperatures) on annealing under UHV and oxidizing conditions was also charted, to provide insights into storage and contamination issues. The goal of the UHV experiments was to conduct accelerated oxidation studies to elucidate rates and activation energies; although an atmosphere of water vapor was desirable, oxygen was used instead for ease.

6.2 The Effect of Substrate Temperature

Thin films of MoS_2 (10-20 nm) were deposited by RF-sputtering[213] on substrates of amorphous, evaporated-carbon and SiO (on Cu grids); the latter were used for oxygen annealing experiments. Films were prepared at substrate temperatures of 70°C (designated AT for ambient temperature) and 220°C (designated HT for high temperature), and data were recorded using the UHV-TEM.

6.2.1 *As-deposited films*

The microstructure of the AT and HT films grown on both carbon and SiO substrates (prepared at Northwestern University) was seen to be dominated mainly by the basal islands. The hexagonal pattern of these basal islands can be clearly seen in Figure 6.2, which shows a typical HREM image of an AT film and the corresponding TED pattern as an inset. However, these domains were extremely short-range ordered; in comparison, basal islands in HT films had relatively longer range order, as shown by the arrowed regions in Figure 6.3. The edge island morphology was also seen in small areas of the film--their small percentage was corroborated by weak intensity rings in the TED patterns; thicker films had more edge islands. These edge islands were not straight, i.e., they had an associated curvature. Diffraction and image data collated from different samples indicated that the planar spacings deviated from ideal single crystal values in these films. A contraction in the spacing of the basal island fringes, and an increase in that of the edge island fringes were observed in these instances. These deviations are

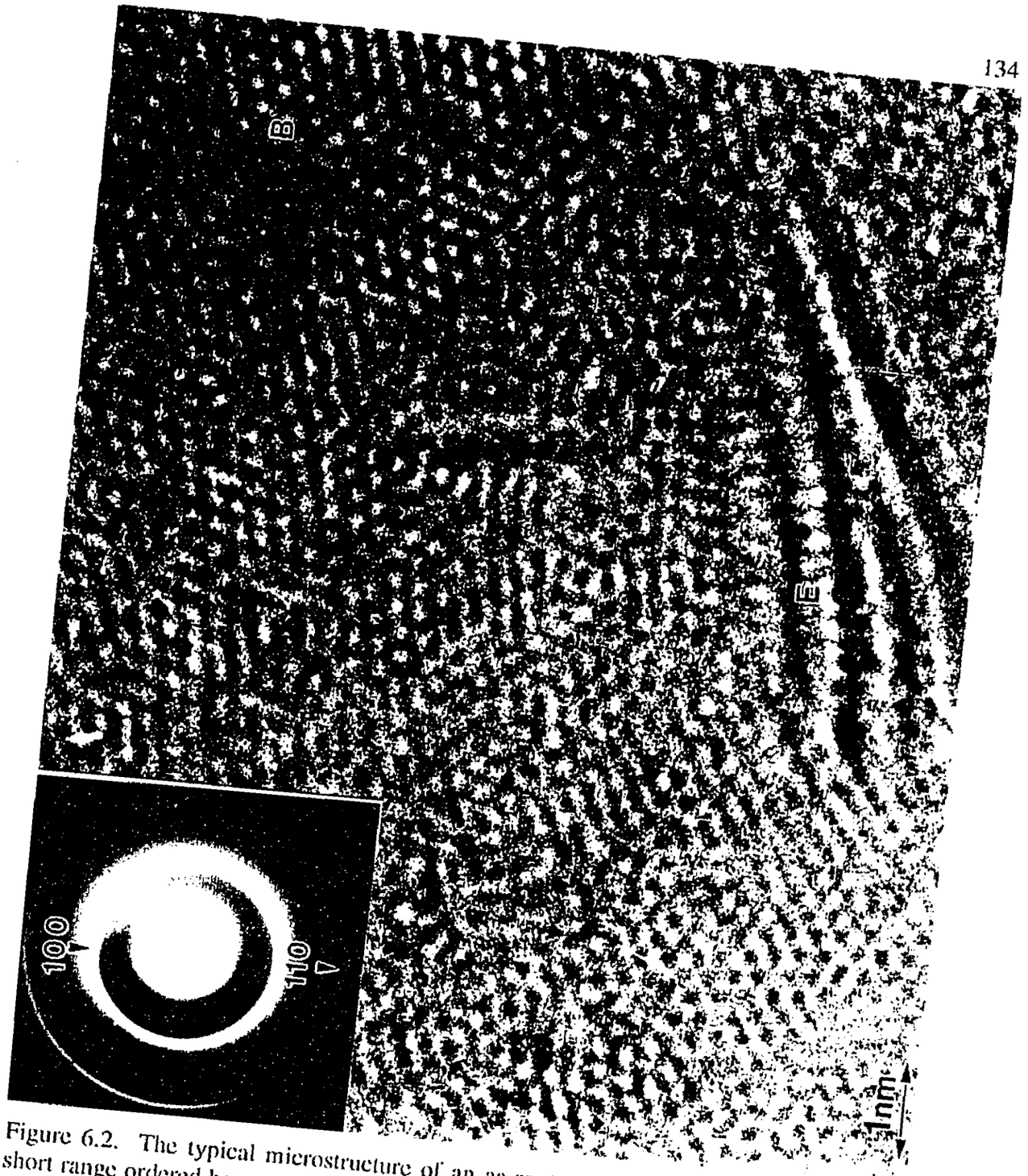

Figure 6.2. The typical microstructure of an as-sputtered AT MoS_2 thin film, i.e., the short range ordered hexagonal pattern of the basal islands (denoted by **B**) is shown in an HREM image while the inset diffraction pattern shows the corresponding (100) and (110) planar spacing rings. The edge island in the figure is denoted by **E**.

Figure 6.3. A typical HREM micrograph of an as-sputtered HT MoS_2 thin film; basal islands with relatively longer range order (contrast to Figure 6.2) are arrowed.

attributed to the formation of $MoS_{2-y}O_y$, which arises from oxygen occupying substitutional sites in the MoS_2 lattice during sample deposition (detected using EXAFS[236]). These structural results are consistent with earlier TEM studies of similar films by other investigators[215,237].

6.2.2 *Annealing Stability*

UHV Environment

The AT and HT films were annealed inside the UHV-TEM using an *in situ* heating holder to temperature cycles in the range of 100-550°C (and held at each temperature for about 10 minutes), in increments of roughly 50°C. To 400°C, no changes in the morphology of either the AT or HT films were evident from the images or the TED patterns. At temperatures just above 400°C, nucleation of small crystallites was seen in the HREM images of AT films. Annealing to 550°C resulted in new spotty polycrystalline rings in the TED patterns; the corresponding HREM images showed particles with (103) and (105) type fringes, as in Figure 6.4. The (100) and (110) fringes still existed in the background (particles showing these fringes were also seen) with a smaller fraction of edge islands, suggesting that the film morphology consisted of a mixture of random polycrystals that had undergone a loss of texture due to heating. The intensity of the rings in the TED patterns suggested that particles showing (103) fringes far exceeded ones showing the (105) type.

In contrast, HT films showed greater stability to such heat treatments. Figure 6.5

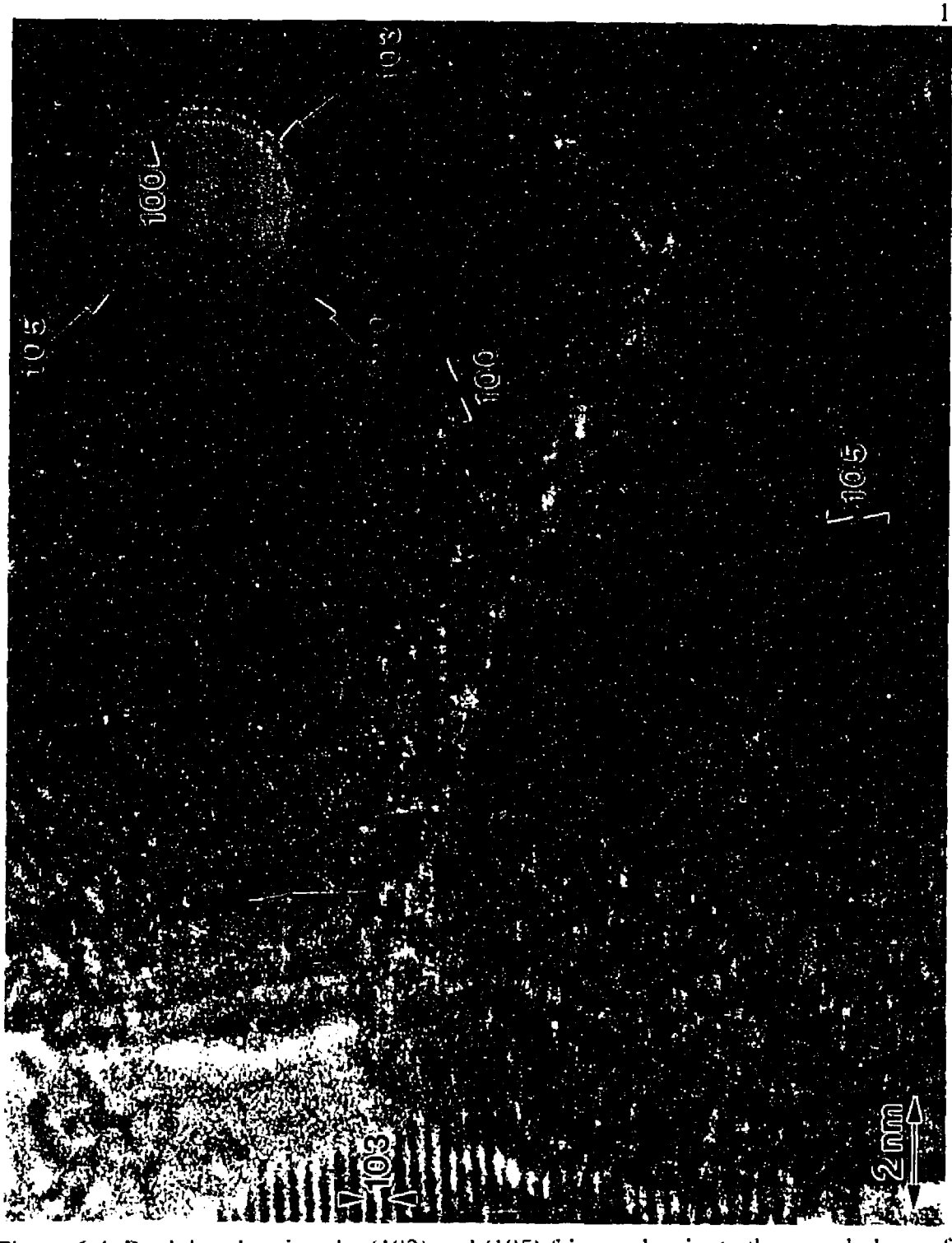

Figure 6.4. Particles showing the (103) and (105) fringes dominate the morphology of an AT film annealed to 500-550°C in an UHV environment; the relative intensities of the corresponding rings in the inset diffraction pattern are proportional to their population density.

Figure 6.5. The microstructure of an HT film annealed to 500-550°C in an UHV environment is identical to that in Figure 6.2 with one very subtle change, i.e., the arrowed darker contrast regions which represent nucleation of very small domains similar to those seen in AT films annealed to 400°C.

shows a HT film heated to 550°C: the initial nucleation of very small domains, arrowed in the figure, are observed (similar to the behavior of AT films on heating to 400°C), suggesting that further heat treatment was required before domains of the size seen in the AT films heated to 550°C could be seen. The small size of the domains in the HT film could also be inferred from the TED patterns (no new polycrystalline rings were seen).

Oxygen Atmosphere

On further annealing the AT film at 550°C for 5 minutes in a partial pressure of oxygen of approximately $1x10^{-5}$ Pa, no change in the morphology was observed, i.e., particles showing (103) and (105) fringes still existed in the images. Annealing at the same temperature for 10 minutes in a higher partial pressure of oxygen, i.e., $1x10^{-4}$ Pa, resulted in the appearance of a few particles of MoO_3. This suggested that inhomogeneous oxidation had occurred; further, the absence of any corresponding ring in the TED patterns indicated their small population.

That the particles were indeed MoO_3 (as opposed to MoO_2) was confirmed during a two hour time sequence under the electron beam, which showed that these particles underwent radiation damage (MoO_3 as the maximum valent transition metal oxide radiation damages, while MoO_2 does not[238]). Figures 6.6 a) and b) show one such particle at the early stages of observation and following the two hour exposure to the electron beam respectively. From Figure 6.6 b), it is apparent that the particle had amorphized and further, reduced to Mo metal at the edges which later crystallized under the electron beam. Figures 6.7 a)-d) show a low magnification view of the region during

Figure 6.6. (a) Inhomogeneous oxidation resulting in MoO_3 particles when AT films are annealed to 500-550°C in $1x10^{-4}$ Pa O_2. A reference particle is shown at the very initial stages of observation and demonstrates the early stages of radiation damage under the electron beam.

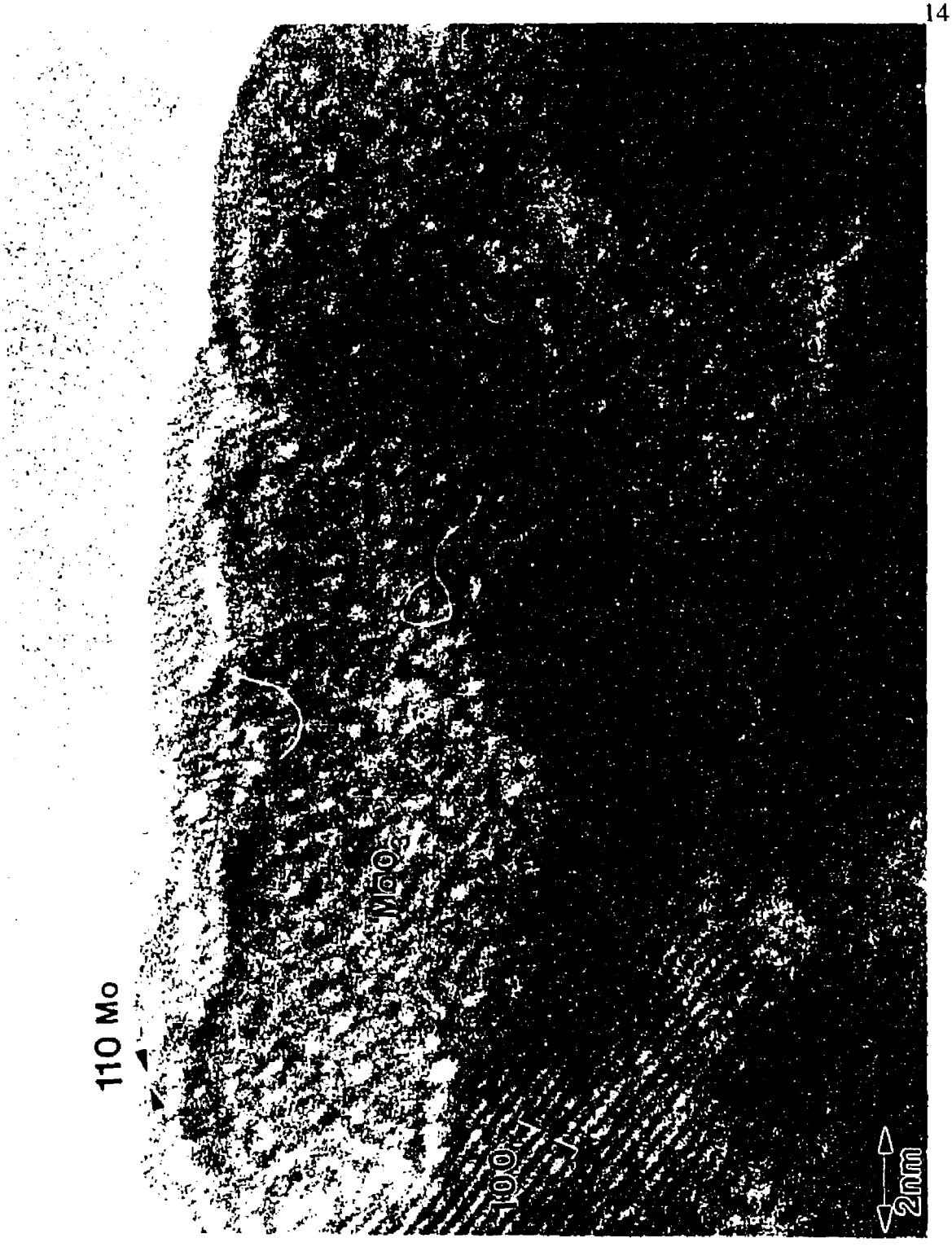

Figure 6.6. (b) The particle in Figure 6.6(a) after a two hour exposure to the microscope electron beam is completely amorphized (confirming that it is MoO_3) and reduced to Mo metal; the crystallization of the latter is seen at the edges of the particle.

Figure 6.7. (a) Low magnification view of the region in Figure 6.6 at the initial stages of observation. The edge island and the MoO_3 particle are clearly seen and are arrowed. (b) Snapshot of the region after a 30 minute exposure to the electron beam; both the particle and the edge island of MoS_2 have started to amorphize.

Figure 6.7. Same region in (a) and (b) following a 60 minute exposure in (c) and a 90 minute exposure in (d) to the electron beam. The amorphization of the MoO_3 particle and the edge island of MoS_2 are complete.

this time and reveal that the edge islands of MoS_2 had also amorphized under the beam; however, the basal islands still remained crystalline during the same period.

As the film was heated to higher temperatures, i.e., between 700 and 800°C under an oxygen partial pressure of $1x10^{-4}$ Pa, significant coarsening occurred, resulting in particles of sizes ranging from 5 to 50 nm as seen in Figure 6.8. While the image provided no information on the particles' orientation or chemistry, the inset TED pattern revealed gross changes in the latter. Rings corresponding to the basal islands had disappeared; instead, spotty rings corresponding to the (300), (310), (410) and (420) spacings of MoO_3 were seen, suggesting that the film had undergone complete oxidation.

6.2.3 *Au Deposition on MoS_2*

Au in the sub- to a few (4-5) monolayer (ML) regime was deposited on to as-deposited AT films and post annealed AT and HT films; the objective of this experiment would become apparent from the discussion in the following paragraphs. Irrespective of the thickness regime, Au growth was always in the form of 3D islands on all types of films (at higher thicknesses, Au islands were larger, i.e., simply grew in size).

Figure 6.9 is a HREM image of the very early stages of growth of Au ($\leq$ 1 ML) on an as-deposited AT film, with the inset TED pattern showing the (111) ring of Au. On further deposition (upto 2 ML), only an increase in the intensity of the (111) ring of Au was observed. The (200) and (220) rings of Au began to appear on subsequent deposition; these were however very weak in intensity in comparison to the (111) ring

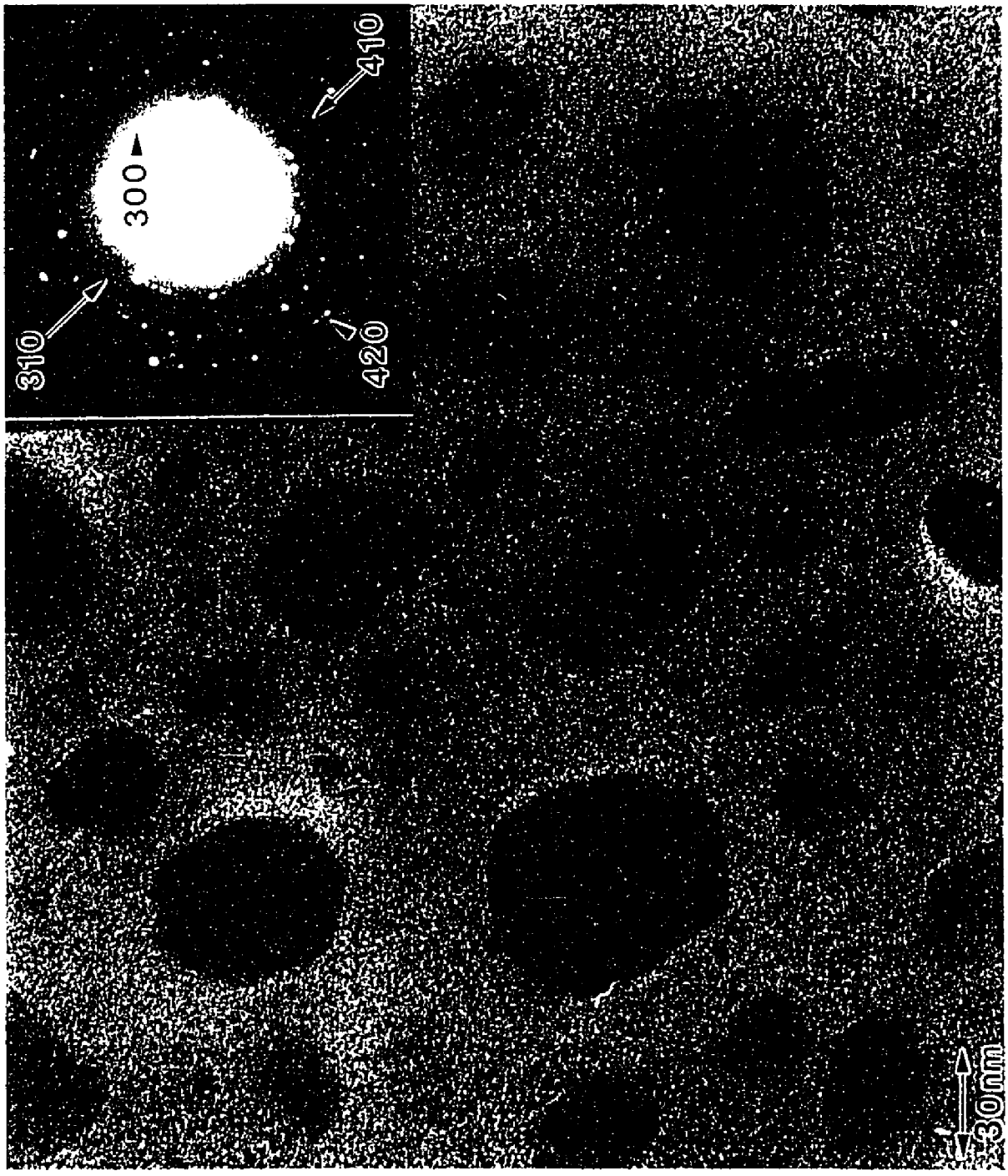

Figure 6.8. Film coarsening yielding 5-50 nm size particles of MoO_3, occurs on annealing AT films to 700-800°C in $1x10^{-4}$ Pa O_2. Spotty polycrystalline rings in the inset diffraction pattern reveal their orientation; the absence of the MoS_2 rings suggests complete oxidation.

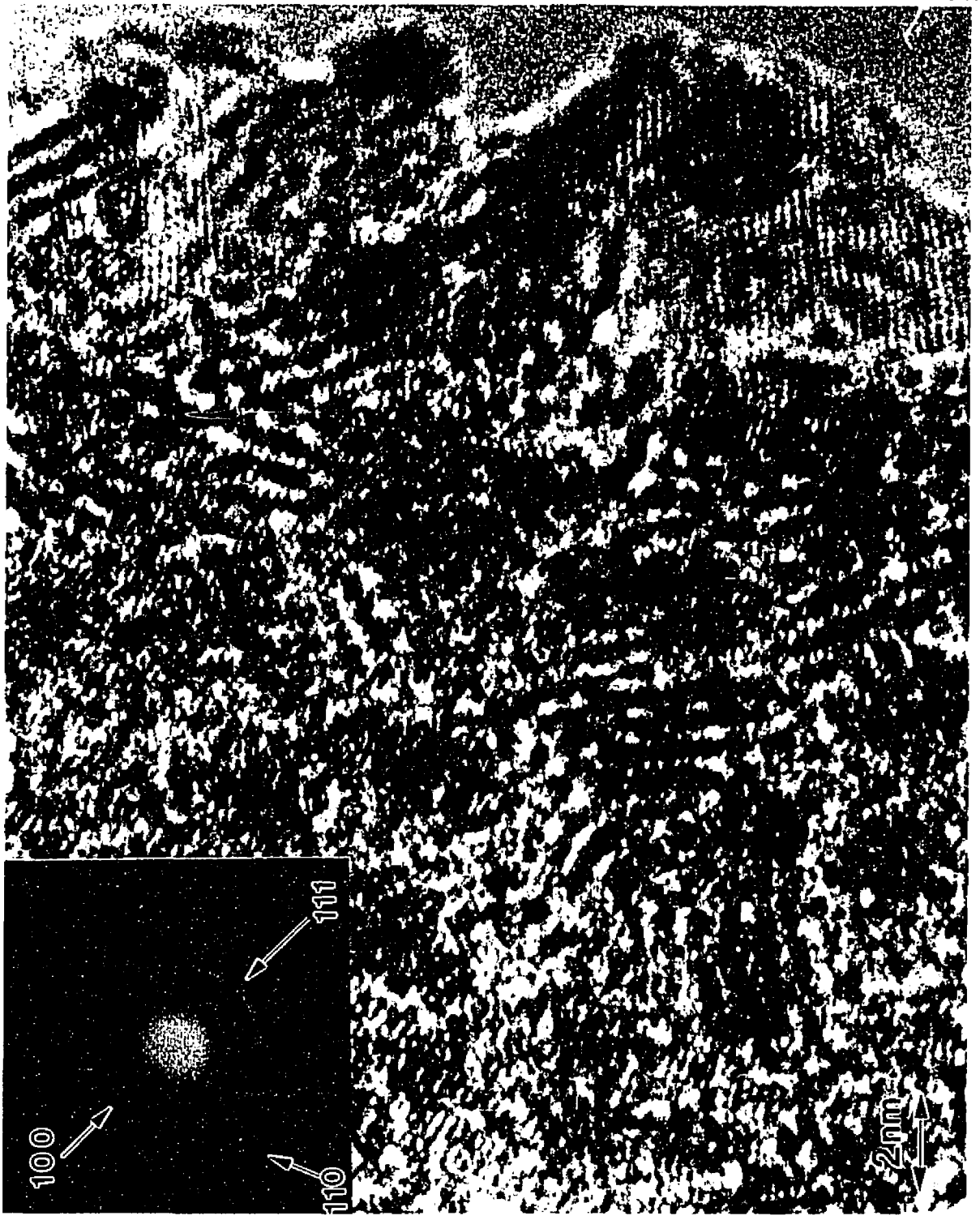

Figure 6.9. Three-dimensional islands of Au seen in the early stages of nucleation and growth on an as-deposited AT film. The (111) ring in the inset diffraction pattern reveals the highly textured nature of this process.

suggesting that Au growth on MoS_2 was highly textured. Also, the HREM images did not demonstrate any preferential site, i.e., basal or edge, for the nucleation and growth of Au on either type of films.

A very surprising result was that in comparison to other substrates, e.g., carbon, SiO, etc. Au had a much higher stability when deposited on MoS_2. Even with high beam flux values, i.e., two orders of magnitude higher than those used in earlier studies of Au on carbon or Au on SiO[168], Au particles on MoS_2 did not fluctuate under the beam suggesting a very strong particle-substrate interaction, rather similar to the behavior of Ag particles on clean Si(001) substrates detailed in Chapter 4.

Armed with this understanding of the morphology and structure of Au (at these low coverages) on MoS_2 films, the evolution of these characteristics as a function of increased thickness, and their influence in the form of multilayer agents on the final morphology of MoS_2 films were studied.

6.3 The role of metal multilayers

6.3.1 *Introduction*

As briefly alluded to earlier, metal incorporation in the form of multilayers in MoS_2 resulted in films having dense microstructures with significant basal plane orientation parallel to the substrate[230]. The presence of multilayers appeared to suppress and/or interrupt the competitive nucleation and growth of edge-plane facets that would lead to the evolution of the porous columnar-plate morphologies; this has a direct effect on the resulting tribological performance of the MoS_2 films. Tests of Au-20%Pd (henceforth referred to as Au-Pd)/MoS_2 multilayer films in sliding contact and in rolling element bearings indicated that these films had better endurance than ones with columnar plate morphologies[224,230]. Also, while multilayers in general inhibit fracture better than the pure films, a brale indentation study[230] revealed differences in the fracture toughness on changing the metal layer periodicity and nominal metal layer thickness in Ni/MoS_2 multilayer films. For these films, fracture around the indentation was reported to be inhibited by decreasing the metal layer periodicity, i.e., for a constant film total thickness, increasing the number of multilayers. Increasing metal layer thickness, particularly above a critical value, also improved fracture resistance.

Based on these early indentation studies, Hopple *et al*[220] investigated the fracture/spallation resistance of Au-Pd/ MoS_2 films as a function of metal layer thickness under indentation and rolling contact. At 10 nm periodicity, films with 5 nm thick metal layers were reported to have better fracture resistance than films with 1.5 nm metal layer

thickness, when the total thickness was held at 400 nm. The 5 nm Au-Pd/ 10 nm films (where the values before and after "/" represent the thickness and periodicity of the metal layers respectively) also performed better than 1.5 nm Au-Pd/ 10 nm films in endurance and torque tests involving angular contact bearings. Although these studies suggest that the respective microstructures are responsible for the variation in the behavior of these films, a detailed understanding of these microstructures is lacking. The current understanding of the structure stems from XRD and SEM data[230] which suggest a simple model that assumes alternating continuous layers of uniform thickness of metal and MoS_2. This hypothesis, however, cannot explain the differing endurance behavior in the films with Au-Pd layers of 1.5 nm and 5 nm periodicities. Such films were therefore characterized using a combination of HREM and TED data collected from the conventional vacuum Hitachi H-9000 microscope operating at 300kV.

6.3.2 *Experimental Results*

Au-Pd/MoS_2 multilayer films were prepared by sequentially depositing Au-Pd and MoS_2 layers using the RF magnetron technique[230] on to carbon films. The following (nominal) compositions were prepared:

a) 1.5 nm Au-Pd + 8.5 nm MoS_2 : Single and double bilayers

b) 5.0 nm Au-Pd + 5.0 nm MoS_2 : Single and double bilayers

A Au-Pd/MoS_2 sequence constitutes a single bilayer, and a repeat of this unit, a double bilayer. In order to attain a better general understanding of the structural

transformations between the single and double bilayers for the low and high Au-Pd compositions, trilayers of the following compositions were also prepared:

c) 1.5 nm Au-Pd + 8.5 nm MoS_2 + 1.5 nm Au-Pd

d) 5.0 nm Au-Pd + 5.0 nm MoS_2 + 5.0 nm Au-Pd

Along the same theme, in order to understand the growth of individual components, and that of Au-Pd on the MoS_2 surface of a complete bilayer film, the following sequences were also studied:

e) 1.5 nm Au-Pd; 5.0 nm Au-Pd; 8.5 nm MoS_2

f) 8.5 nm MoS_2 + 1.5 nm Au-Pd; 5.0 nm MoS_2 + 5.0 nm Au-Pd.

Since the above thickness values were extrapolated from deposition parameters established for thicker films, it is more appropriate to refer to these as either low flux ($\leq$ 1.5 nm Au-Pd) or high flux ($\geq$ 5 nm Au-Pd) films. Prior to delving into the structure of the Au-Pd/MoS_2 films, the nature of the Au-Pd layer was investigated in the two flux regimes.

Structure of the First Layer and Single Bilayer Films

HREM images and TED patterns revealed gross differences in the structure of the Au-Pd films deposited on carbon substrates in the two different flux regimes. Discrete 3D metal islands were seen in the low flux films corresponding to a Volmer-Weber growth mode (very similar to the case of Au deposited on MoS_2, and observed in the UHV-TEM study); these 3D islands had a mixture of single crystals and multiply twinned structures as shown in Figure 6.10 (this mixed morphology growth is similar to that

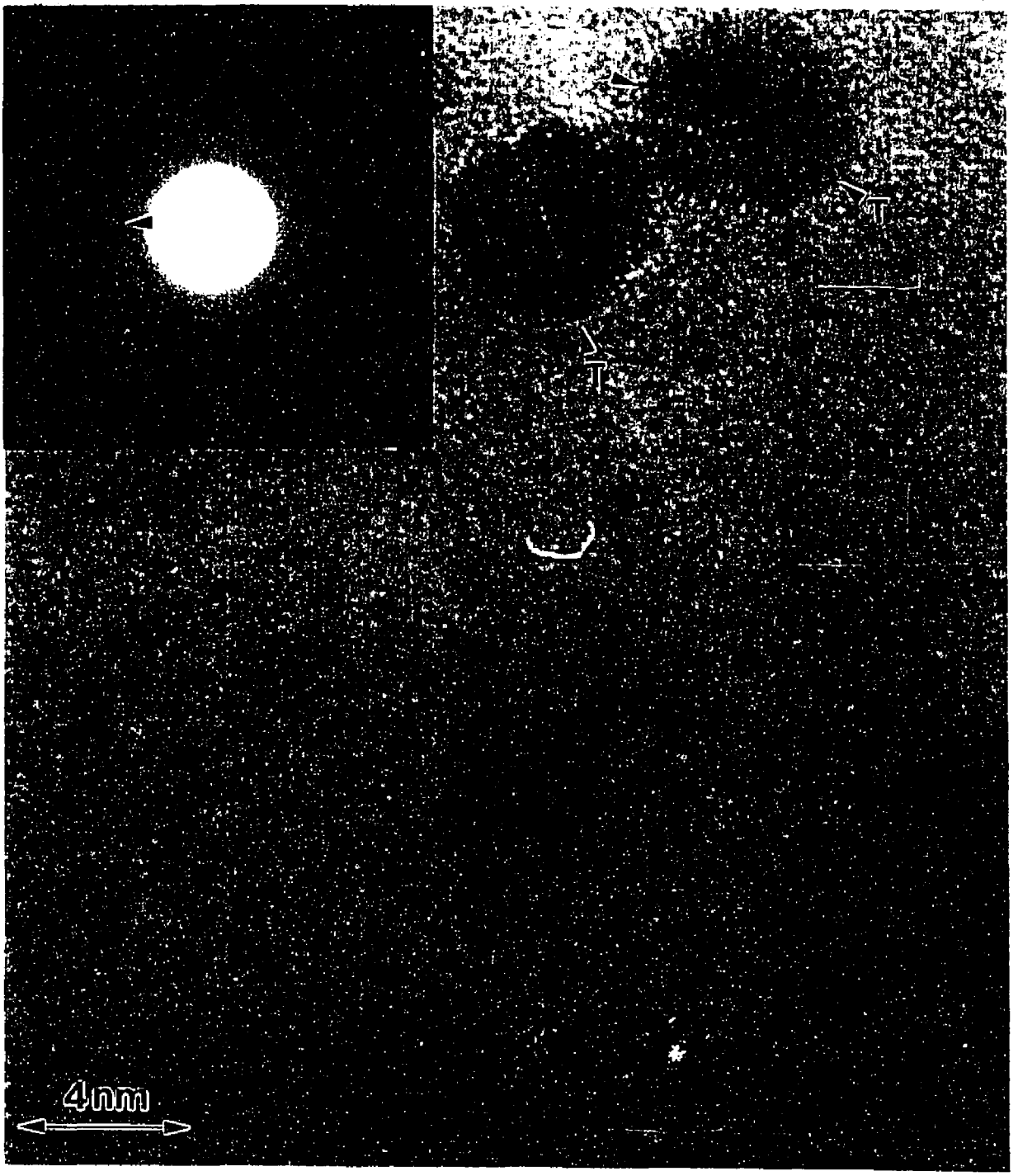

Figure 6.10. The typical microstructure of a low flux Au-20%Pd film deposited on a carbon substrate: 3D islands comprising of single crystals and multiply twinned particles; T denotes twins in the latter. The inset diffraction pattern of the region in the image shows diffuse rings corresponding to the small sizes of these particles; the (111) ring of Au-20%Pd is arrowed for reference.

reported in case of Au and Ag deposited on holey carbon and SiO substrates[165,166], and also in case of Ag deposited on clean Si(001) substrates, see Chapter 4). The islands ranged in size between 2.5 to 5 nm, which explains the diffuse rings seen in the TED pattern inset of Figure 6.10. On the other hand, metal layers in the high flux case were seen to have a quasi-continuous polycrystalline nature, as shown in Figure 6.11, suggestive of coalescence at later stages of growth. Domain sizes ranged between 5 to 10 nm with domains being twin-related in certain regions. The inset TED pattern in Figure 6.11 shows sharp polycrystalline rings with spacings that could all be indexed using pure Au as a reference. The quasi-continuous nature of the film was apparent on tilting the film, which brought off-axis Au-Pd nanometer-size grains into the lattice imaging conditions.

Single bilayer films formed by depositing MoS_2 onto both low and high flux metal films were seen to have a very dense microstructure with extremely small domains of basal islands coexisting with some edge islands (Figure 6.12). This interpretation was confirmed by looking at MoS_2 films deposited directly onto carbon substrates where the same microstructure, i.e., coexistence of small basal island domains and edge islands was observed.

Structure of the Trilayer (TL) and Double Bilayer (DB) Films

Au-Pd deposition on such SB films (resulting in a trilayer film) were studied to characterize the structural differences, if any, in the two compositional cases. TED patterns in both cases showed an increase in the intensity of the rings from the

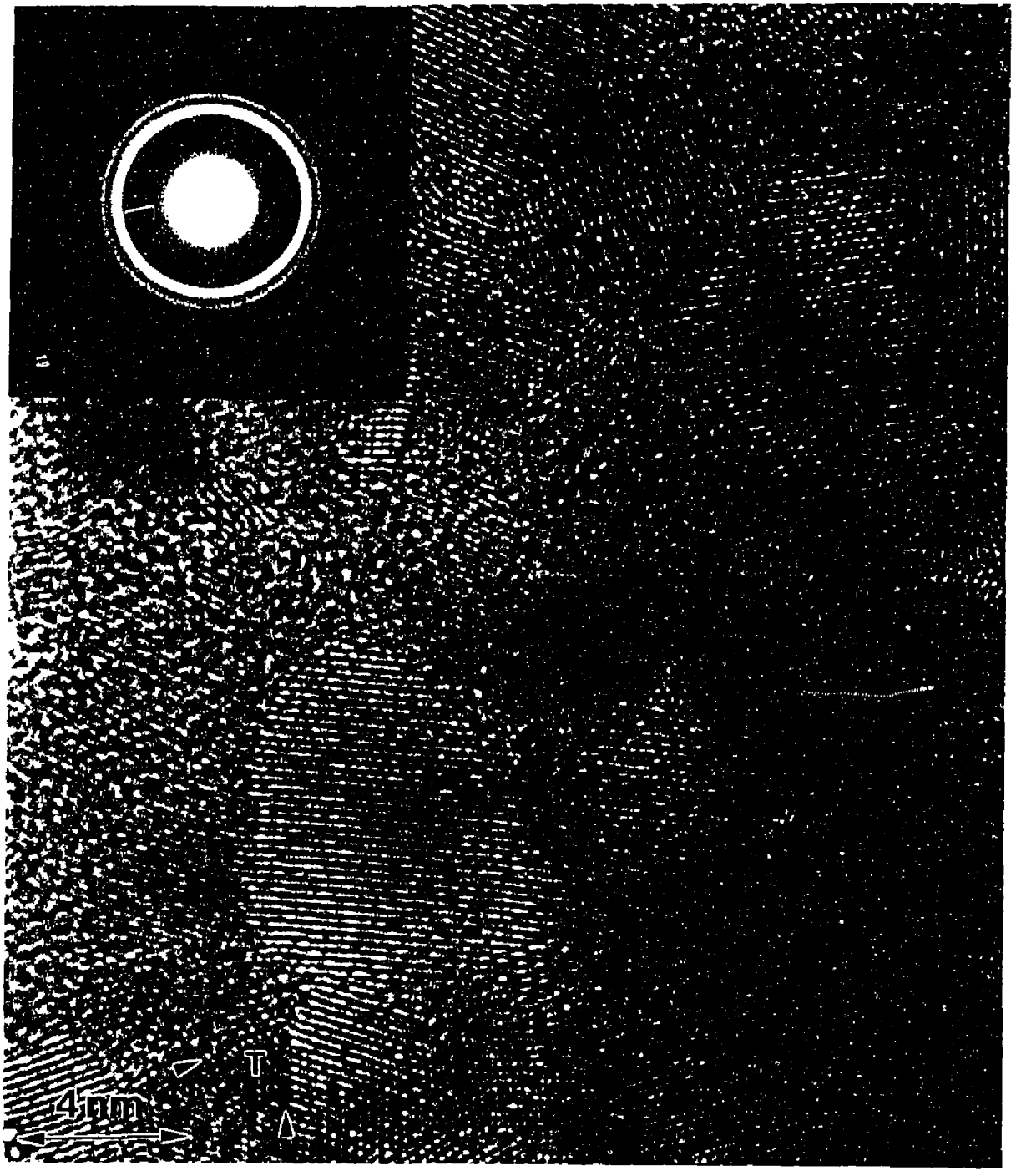

Figure 6.11. The typical microstructure of a high flux Au-20%Pd film deposited on a carbon substrate: the quasi-continuous, polycrystalline nature of the film as opposed to discrete 3D islands in Figure 6.10 is apparent; a twinned particle is arrowed and denoted by **T**. The inset diffraction pattern shows sharp rings of polycrystalline Au-20%Pd domains; note also the stronger intensity of the Au-20%Pd(111) ring (arrowed).

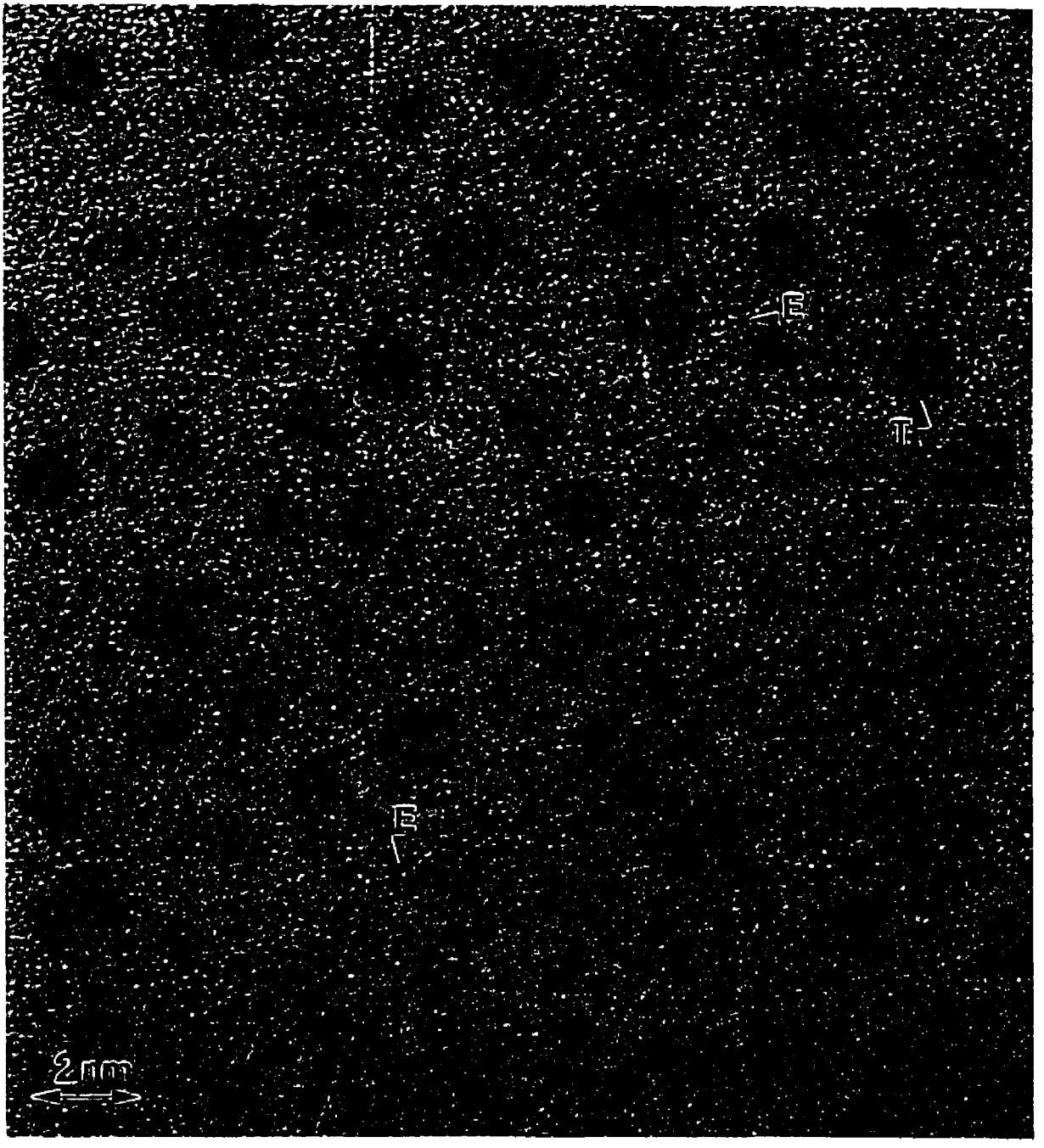

Figure 6.12 (a) The microstructure of a single bilayer film in the low flux case shows 3D metal islands (twinned ones labelled as **T**) co-existing with extremely small domains of basal and edge (labelled as **E**, difficult to see at this defocus) islands of MoS_2.

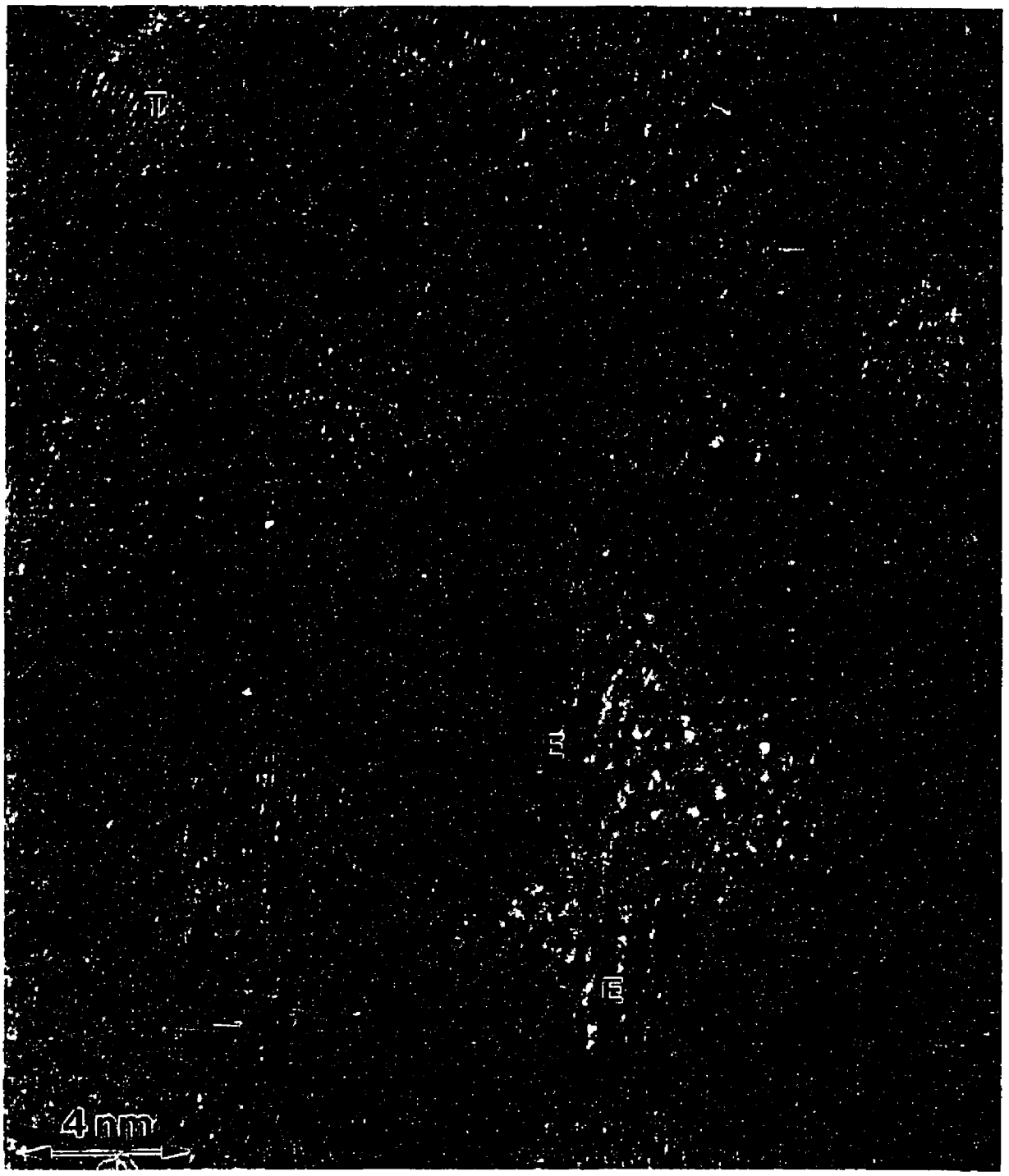

Figure 6.12. (b) The microstructure of a single bilayer film in the high flux case: polycrystalline, quasi-continuous metal film (**T** denotes twinned regions) coexists with basal and edge islands of MoS_2 (denoted by **E**).

corresponding SB cases which would be consistent with an increase in the Au-Pd content. Sharpening of the rings was also seen, especially in the low flux films, suggesting an increase in domain size, as is apparent from Figure 6.13(a). Since, in the low flux films, Au-Pd forms discrete 3D islands on carbon substrates, MoS_2 films deposited on such single layers (forming SB) can be expected to grow primarily on the exposed carbon substrate. Deposition of further Au-Pd on such films (forming TL) would therefore lead to an increase in domain size via coalescence with the existing 3D Au-Pd islands. In the high flux case, shown in Figure 6.13(b), MoS_2 growth would be on a quasi-continuous, polycrystalline Au-Pd underlayer, and further Au-Pd deposition on such bilayers would lead only to an increase in the Au-Pd content. The above explanations would be valid if and only if the growth of Au-Pd on the MoS_2 surface of SB films parallels that on carbon substrates. Therefore, 1.5 and 5 nm thick Au-Pd films deposited onto 8.5 and 5 nm MoS_2 films were also studied. The growth mechanism was in fact found to be identical to that on carbon, i.e., 3D islands and quasi-continuous films of Au-Pd on MoS_2 respectively (Figures 6.14(a) and (b)). Also, similar to observations of Au deposition on MoS_2 under UHV conditions reported in the earlier section, Au-Pd growth was seen to occur on both the edge and basal island sites on the MoS_2 film.

Deposition of MoS_2 on such TL films yielded DB films. The DB films of low and high metal flux compositions are shown in Figures 6.15(a) and (b). In the low flux case, the morphology appeared similar to the SB or TL case, i.e., edge islands and isolated small Au-Pd particles; in contrast, hexagonal basal island domains of MoS_2 are seen in the high flux films (along with edge islands and polycrystalline Au-Pd domains).

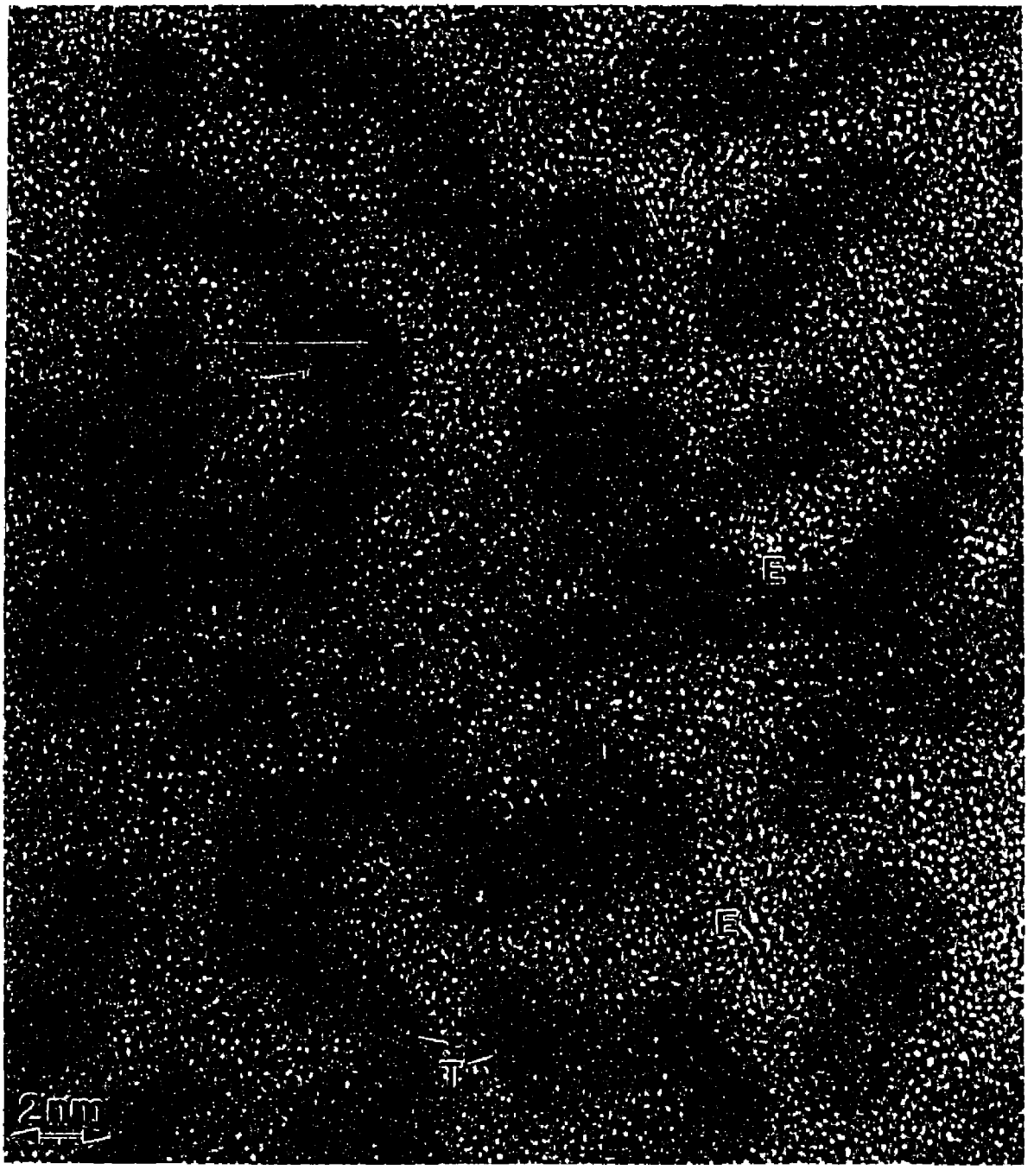

Figure 6.13. (a) The microstructure of trilayer films formed by depositing Au-Pd on a single bilayer film in the low flux case. Note the coalescence of 3D metal islands (compare to Figure 6.10); twinned domains are denoted by **T** and edge islands of MoS_2 by **E**.

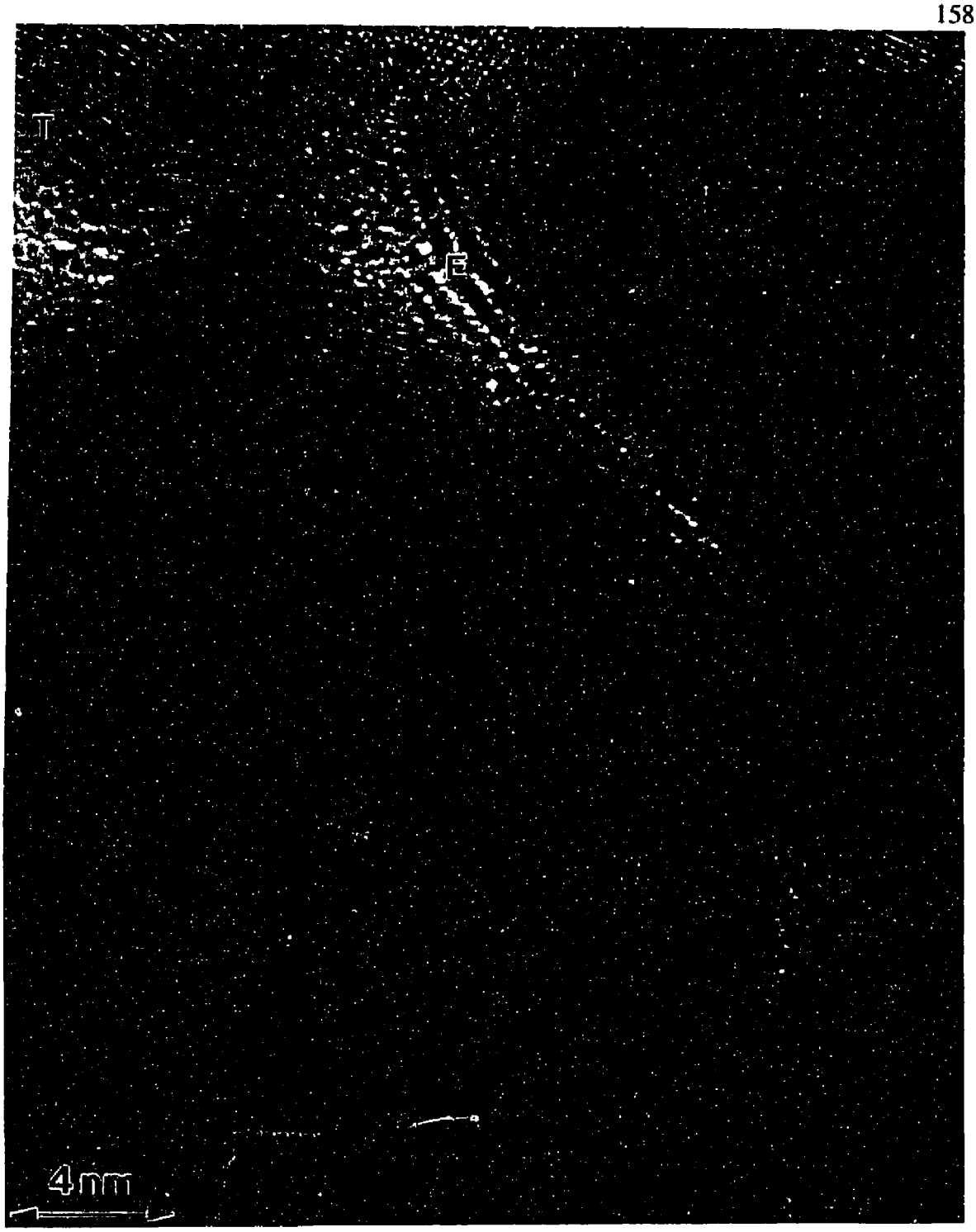

Figure 6.13. (b) The microstructure of trilayer films formed by depositing Au-Pd on a single bilayer film in the high flux case. The microstructure is similar to Figure 6.12(b), i.e., polycrystalline, quasi-continuous metal film with twinned domains denoted by **T** coexisting with basal and edge islands (**E**) of MoS_2.

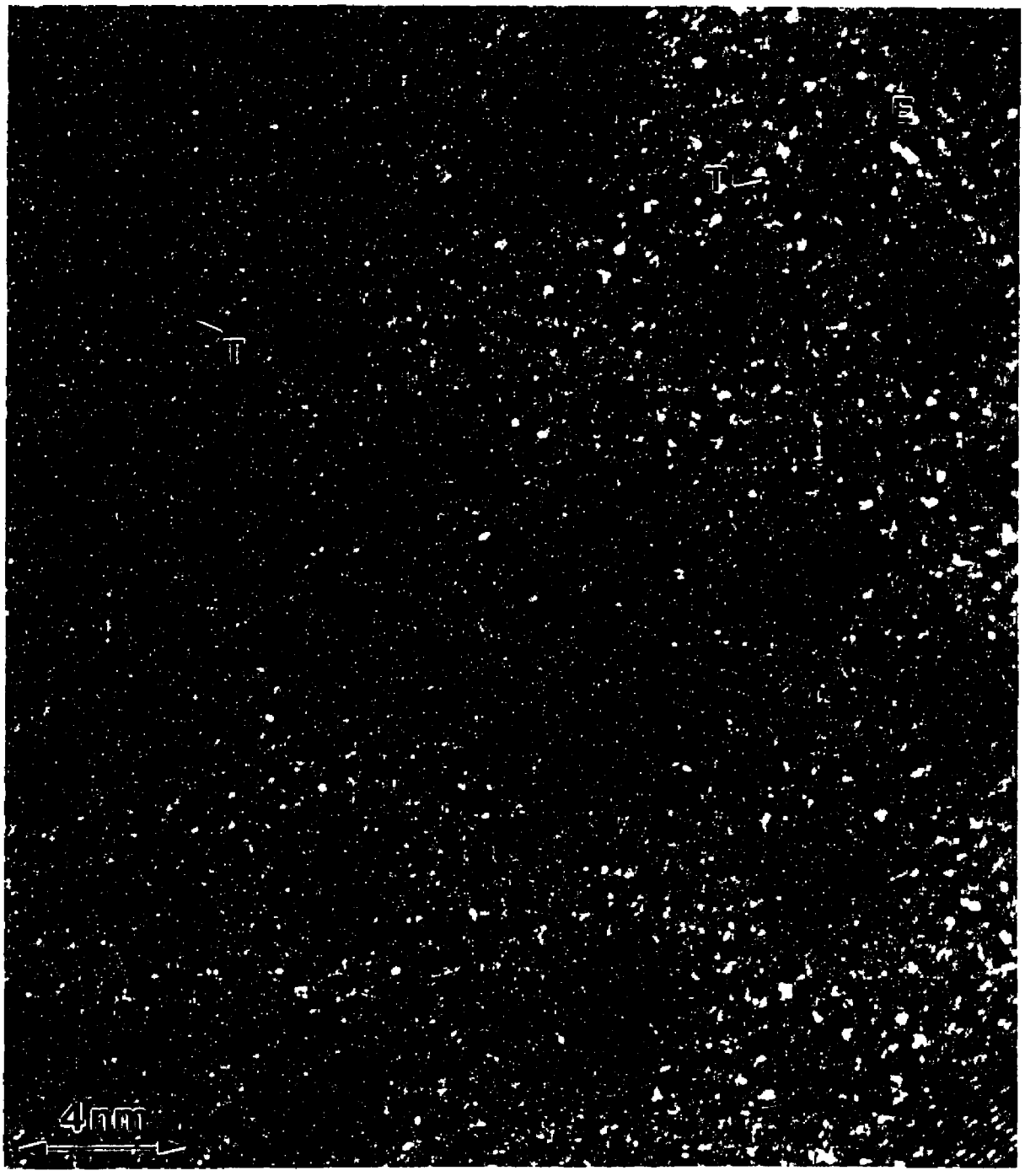

Figure 6.14. (a) Growth morphology of Au-Pd of the low flux composition on MoS_2 substrates. Behavior is similar to that on holey carbon and silicon monoxide substrates. **T** and **E** denote twinned metal domains and edge islands of MoS_2 respectively.

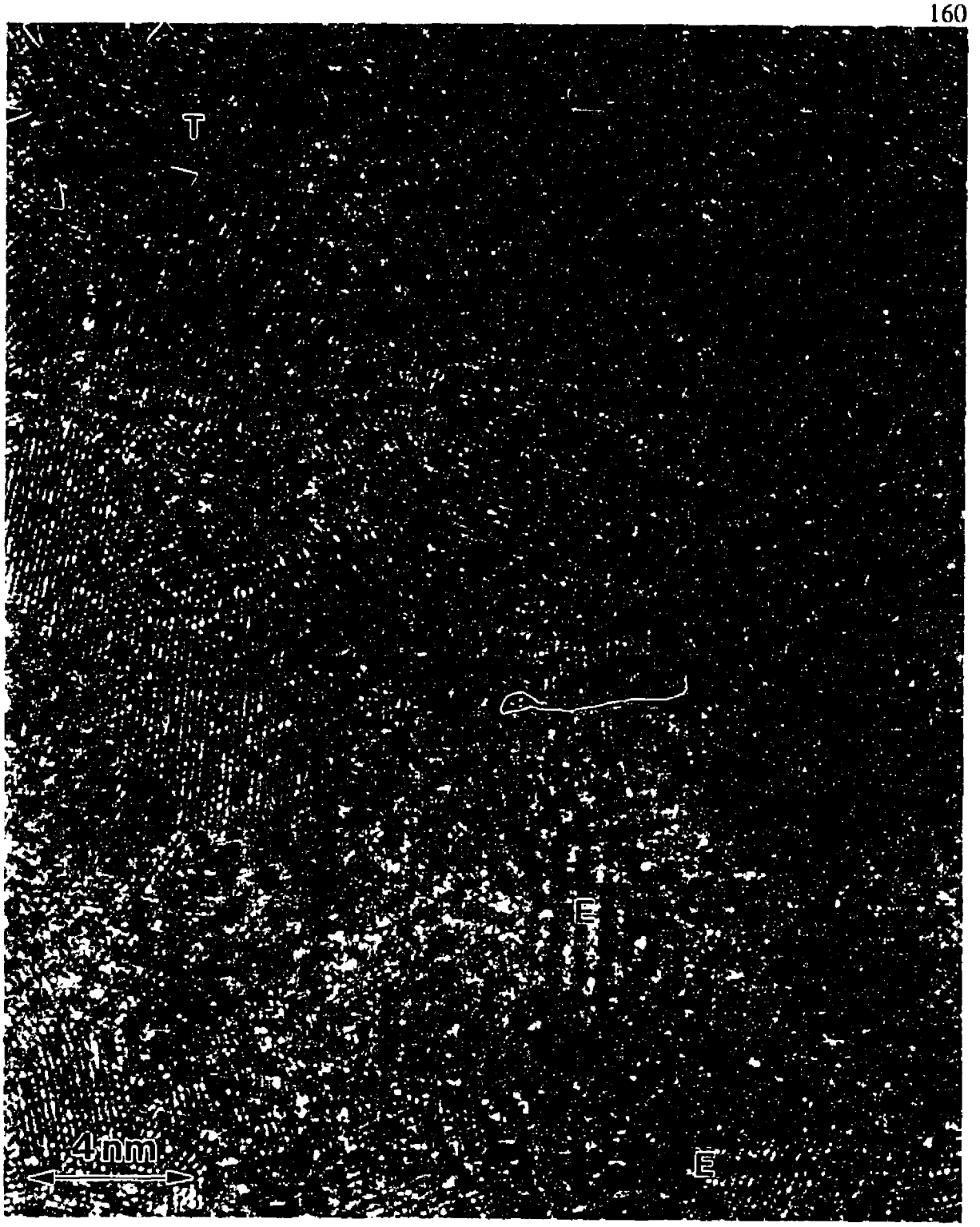

Figure 6.14. (b) Growth morphology of Au-Pd of the high flux composition on MoS_2 substrates. Behavior is similar to that on holey carbon and silicon monoxide substrates. T and E denote twinned metal domains and edge islands of MoS_2 respectively.

Figure 6.15. (a) Morphology of double bilayer films of low flux metal compositions: Twinned metal particles (**T**) and edge islands of MoS_2 (**E**) are seen.

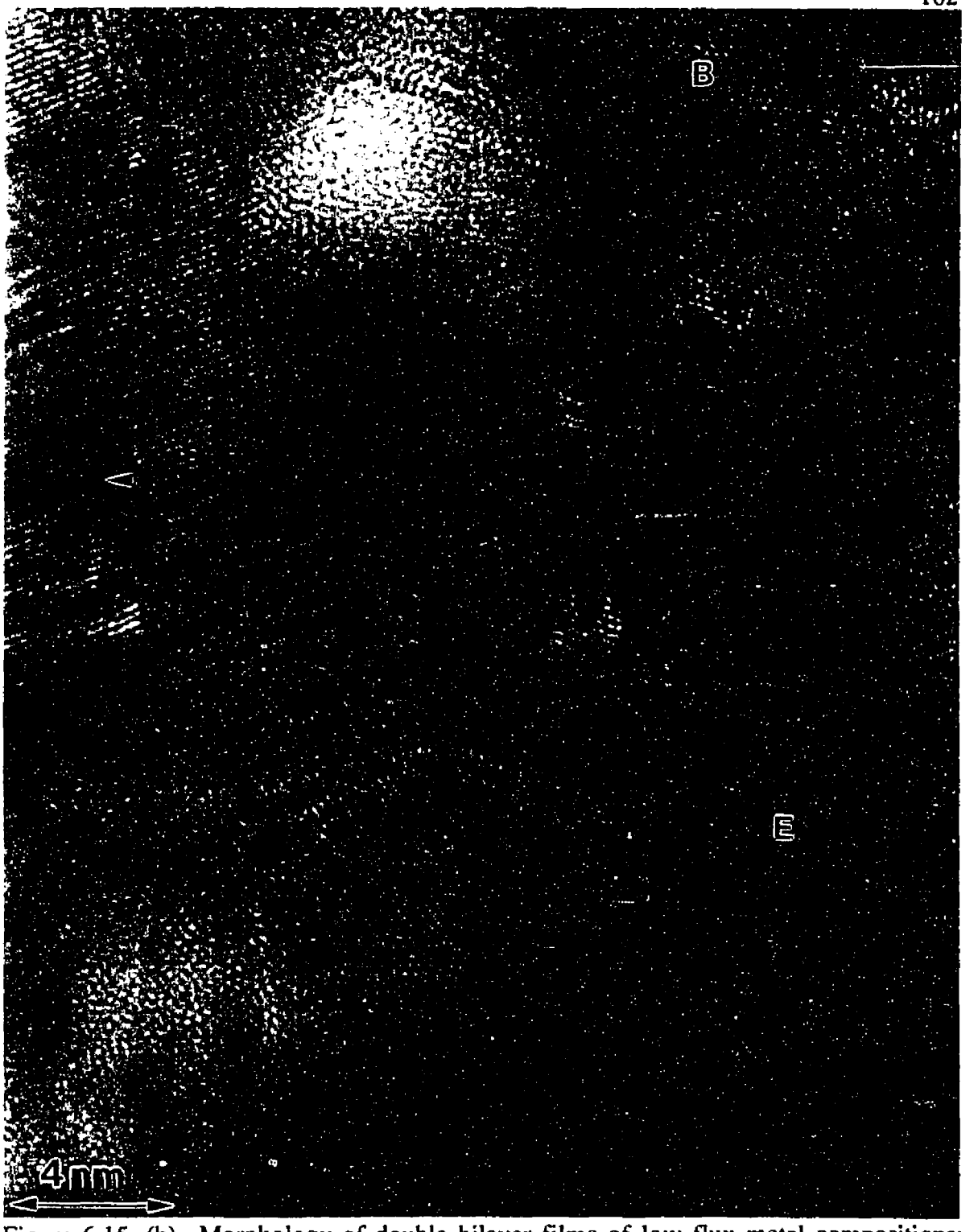

Figure 6.15. (b) Morphology of double bilayer films of low flux metal compositions: hexagonal domains of the basal islands (**B**) and edge islands (**E**) of MoS_2 co-exist with polycrystalline metal domains (arrowed).

The corresponding TED patterns show the differences from the corresponding SB cases: the (002) ring of MoS_2 was faintly visible in both cases, while an extremely weak (100) ring of MoS_2 was also seen in the 5 nm Au-Pd case. This suggests that the morphology of MoS_2 varies strongly with the nature of the underlayer (i.e., continuous film or island).

6.4 The role of co-sputtered metal dopants

6.4.1 *Introduction*

An alternative approach to incorporating multilayers is to use co-sputtered dopants, such as Ni, SbO_x, or Au. One of the advantages of the approach is that the hardware necessary for preparing cosputtered films is less complex (and less costly) than that used for multilayer films. Co-sputtered SbO_x-MoS_2 films in particular, are reported to have good tribological performance in sliding contact[239]. (Sb_2O_3 has been shown to be an effective tribological additive in burnished and bonded MoS_2 lubricant films[240,241].) Recently, two studies reported characterization via EXAFS and XPS, of MoS_2 films incorporating co-sputtered Ni or SbO_x, or multilayers of Ni or Au-20%Pd[242,243]. These studies showed that the metal-MoS_2 films consisted of a $MoS_{2-y}O_y$ phase coexisting with the MoS_2 phase, consistent with earlier findings on pure MoS_2 films[236]. The $MoS_{2-y}O_y$ phase exhibited a MoS_2-like structure, with oxygen substituting for sulfur atoms in the MoS_2 lattice. The amount of the $MoS_{2-y}O_y$ phase could be as high as 25 times that of the MoS_2 phase. Increasing oxygen content (up to 40% was detected in SbO_x-MoS_2 films) correlated with increasing values of "y" in the $MoS_{2-y}O_y$ phase, as well as with decreasing relative amounts of the pure MoS_2 phase. For the Ni-containing films, EXAFS showed that Ni had not reacted chemically with either $MoS_{2-y}O_y$ or MoS_2, but instead formed a disordered NiO phase. Short-range order decreased slightly with increasing Ni content. Films co-sputtered with SbO_x, on the other hand, had little or no short-range order. These EXAFS studies did not provide data however, on the effect of the additives on the final

microstructure of the MoS_2 films.

An attempt was therefore made to characterize the final microstructure of the Ni-MoS_2 and SbO_x-MoS_2 co-sputtered films; similar to the study on the multilayer films, HREM and TED data were recorded using the conventional vacuum microscope.

6.4.2 *Experimental Results*

Pure MoS_2 films were prepared by direct current (d.c.) triode sputtering, using equipment reported in greater detail elsewhere[229]. Co-sputtering was accomplished by sputtering from rod targets of compressed MoS_2 powder, and of Ni or Sb_2O_3. Films of four nominal compositions were prepared, i.e., Pure, 3% Ni, 9% Ni, and 20%SbO_x, by deposition onto amorphous carbon grids for time periods of 50 and 150 seconds. These were studied so as to characterize the microstructure as a function of both metal composition and total film thickness.

The 150 seconds case

HREM images revealed the co-existence of basal and edge islands for all four types of films studied. Nearly identical microstructures were seen for both the pure and 3% Ni co-sputtered MoS_2 films. The morphology in these cases was dominated primarily by edge islands with regions of short-range ordered basal islands; this was in stark contrast to that observed in the 9% Ni and SbO_x co-sputtered films. These differences are evident in both Figures 6.16 and 6.17, which are montages of data collected from the

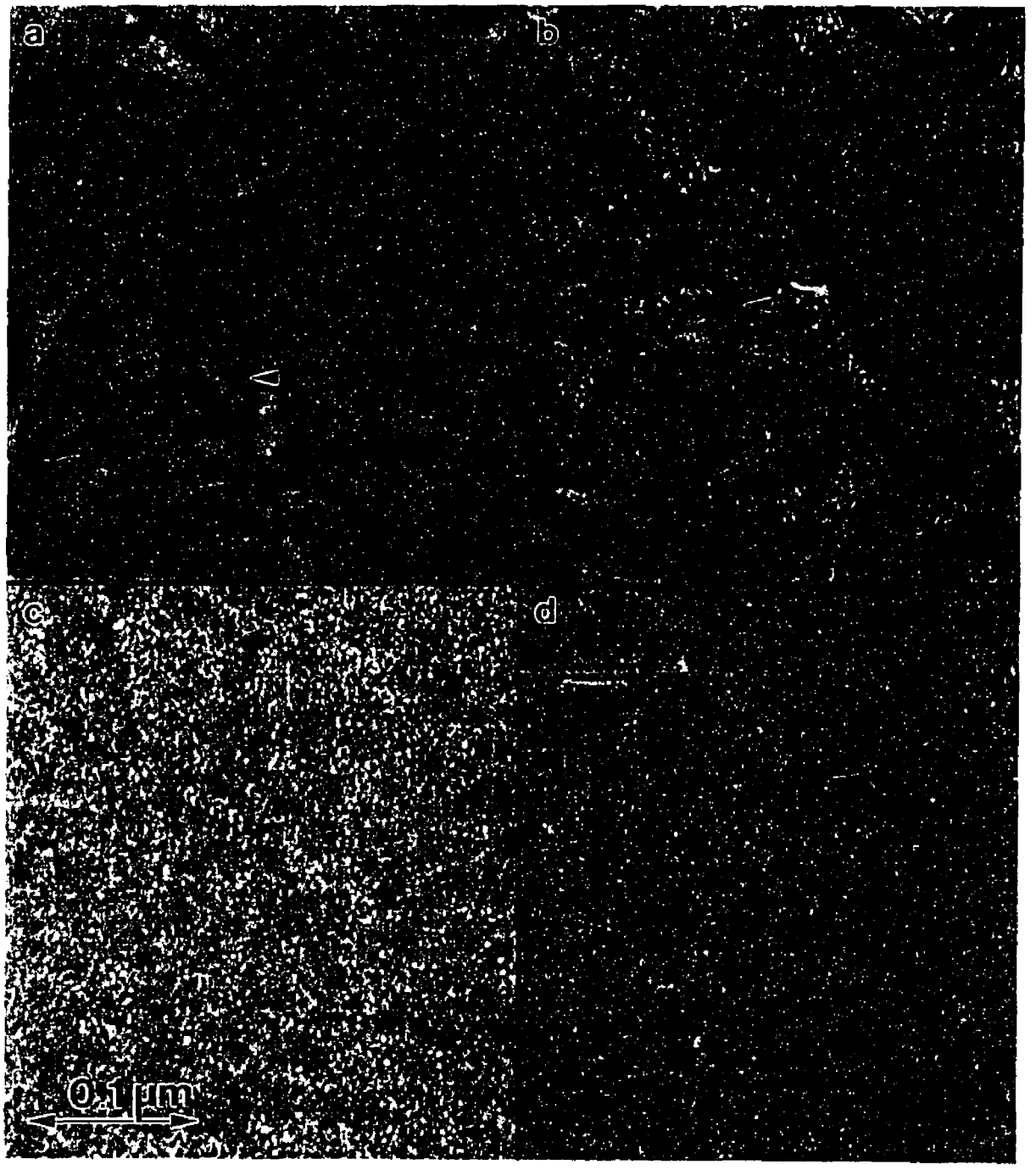

Figure 6.16. Montage of images recorded at low magnification from films of four different compositions, deposited for 150 seconds: a) Pure MoS_2, b) 3% Ni-MoS_2, c) 9% Ni-MoS_2, and d) 20% SbO_x-MoS_2. Edge islands in a) and b) are arrowed; note the decrease in their density in c) and d), in comparison to a) and b).

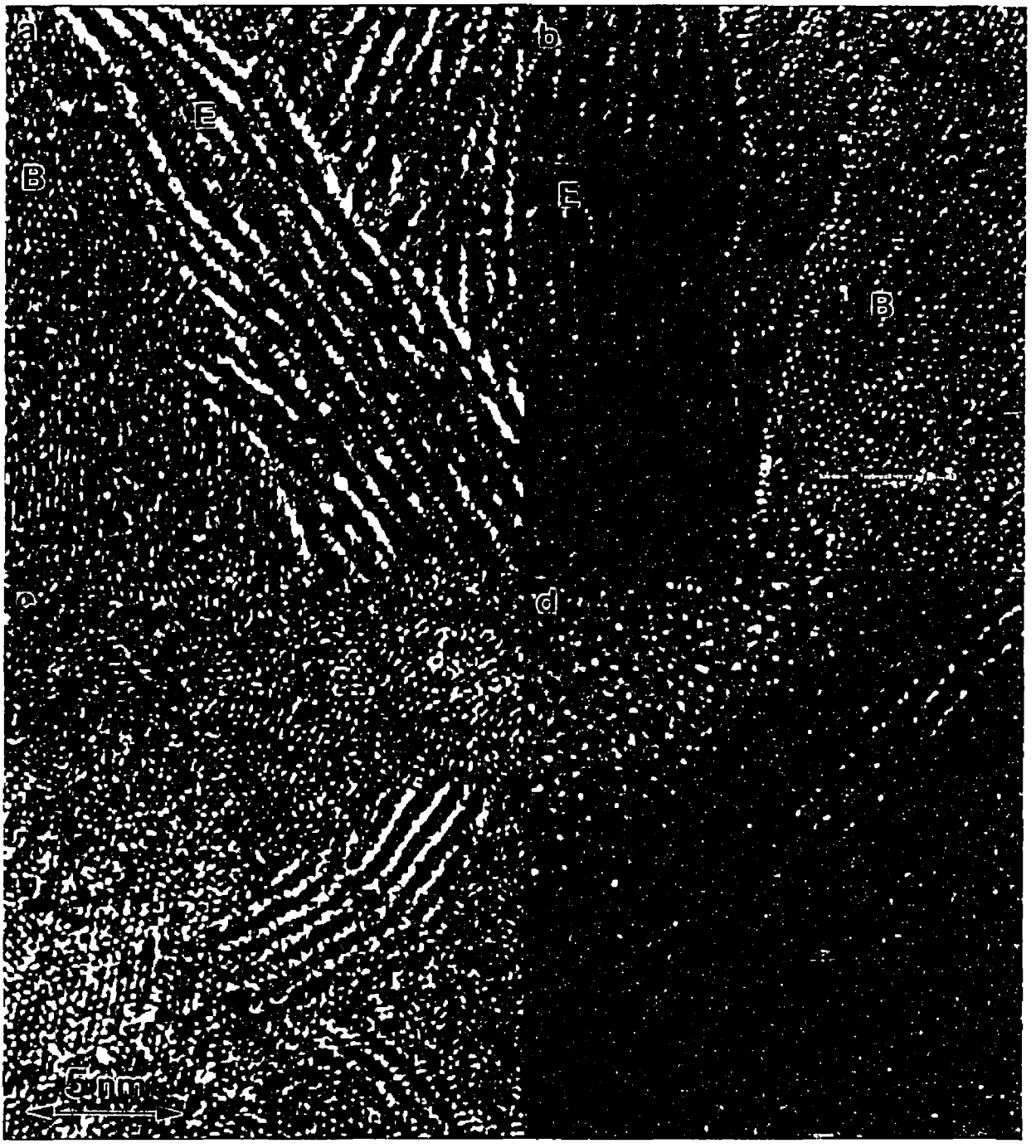

Figure 6.17. Montage of images recorded at higher magnification of the regions in Figure 6.16. Hexagonal basal island (denoted by **B**) domains coexist with edge islands (denoted by **E**) in a)-c) while the extreme short range order of basal islands is apparent in d).

films at low and high magnification respectively. Figure 6.16 clearly reveals that the population of edge islands decreased rather dramatically (in comparison to the pure and 3% Ni co-sputtered MoS_2 films) on sputtering with either SbO_x or 9% Ni. In addition, a decrease in the size of these islands was also noticeable in the 9% Ni co-sputtered MoS_2 films: the edge islands in these films ranged in width and length between 2.5 to 4 nm and 5 to 7 nm; in comparison, the islands were nearly 10 to 15nm wide and about 40 to 60nm in length in films of the other three compositions.

TED patterns recorded from the regions in Figure 6.17 are montaged in Figure 6.18, and showed changes in the film microstructure as a function of addition of either Ni or SbO_x. The intensities in the patterns have all been scaled to the same dynamic range, to facilitate both qualitative and quantitative comparisons. The as-sputtered films and Ni co-sputtered films were highly polycrystalline in nature. In the case of the pure films, the (100) and (110) rings of the basal islands were clearly seen to co-exist with an extremely strong (002) ring, arising from the dominant edge island morphology; a very weak (103) ring due to the near-basal regions, was also observed in these patterns (the feature is probably lost in the reproduction process). Films co-sputtered with 3% Ni showed a slight decrease in the intensity of the (002) ring, and a sharpening and increase in the intensity of the (103) ring, relative to the pure case.

Thus, TED data revealed subtle changes in the morphology in the form of a decrease in the population of edge islands, and an increase in that of the near-basal islands to accompany the sputtering process (these were not apparent in the HREM images). The dramatic changes in the microstructure seen in HREM images of the 9%

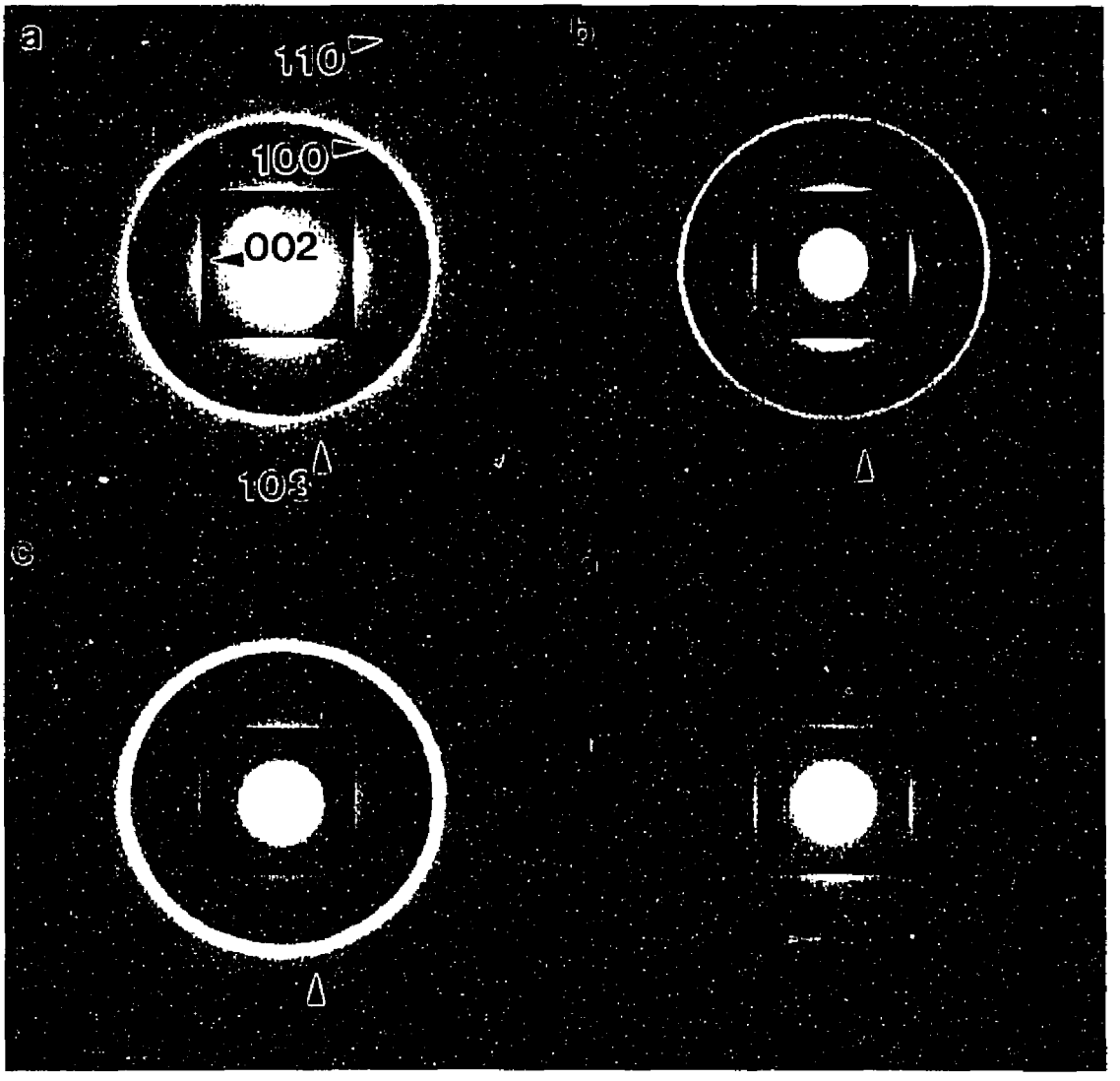

Figure 6.18. Montage of TED patterns from corresponding regions in Figure 6.17. Insets show the region around the transmitted beam, extracted from patterns recorded at a lower exposure time. The (002), (100), (110) and (103) rings are arrowed for reference in the pure film. Note the decrease in intensity of the (002) ring and increase in that of the (100) and (110) rings with increasing Ni content. Disappearance of the (103) ring between b) and c) reveals significant reorientation of the near-basal regions. Weak diffuse rings in d) corroborate the extreme short range order in Figure 6.17(d).

Ni co-sputtered films were also corroborated by the corresponding TED data. These showed a complete disappearance of both the (002) and (103) rings in comparison with the pure and 3% Ni films; a significant increase in the sharpness and intensity of the (100) and (110) rings was also seen. TED patterns from films co-sputtered with SbO_x showed extremely diffuse, weak rings suggesting that the grains had exceedingly short range order.

The 50 seconds case

In comparison to the films described above, those deposited for only 50 seconds showed a generic decrease in both the fraction and size of edge islands; the latter however, still dominated the morphology for pure and 3% Ni films. Edge islands were nearly non-existent in films co-sputtered with either 9% Ni or SbO_x, as shown in Figures 6.19 and 6.20, which are montages of the microstructures of the films observed at low and high magnification respectively. TED patterns recorded from these films also showed a corresponding decrease in the intensity of the rings (as compared to the ones in Figure 6.19), thus agreeing very well with the HREM data.

Aside from the MoS_2 reflections, in the 3% and 9% Ni cases, sharp rings of extremely weak intensity were also seen. Based on their spacings and earlier EXAFS data[237], they are hypothesized to originate from regions of Ni-oxide.

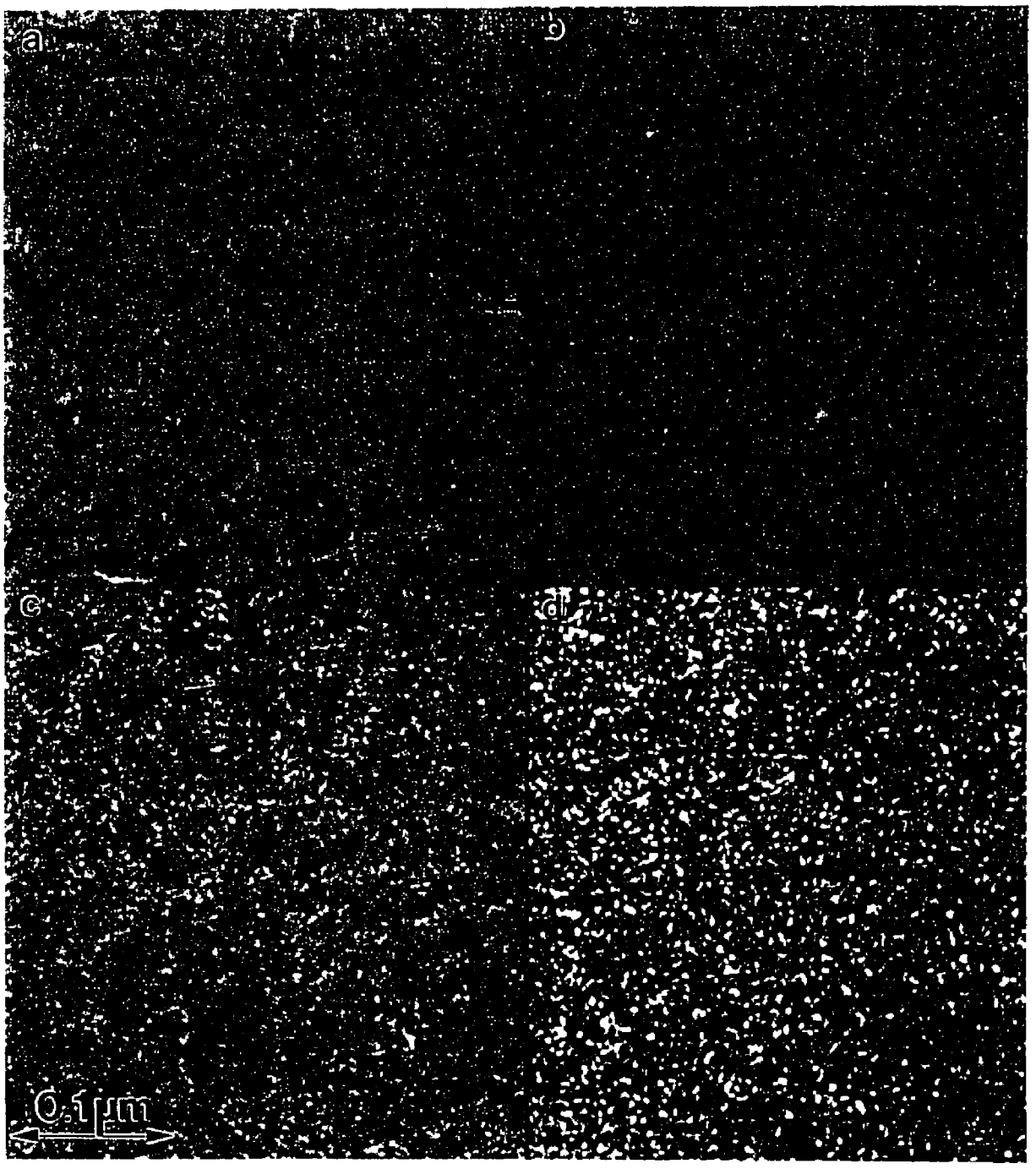

Figure 6.19. Montage of images, recorded at low magnification, from films deposited for a total time of 50 seconds. a)-d) represent the same compositions as in Figures 6.16 and 6.17. Note the generic decrease in edge island density, in comparison to Figure 6.16.

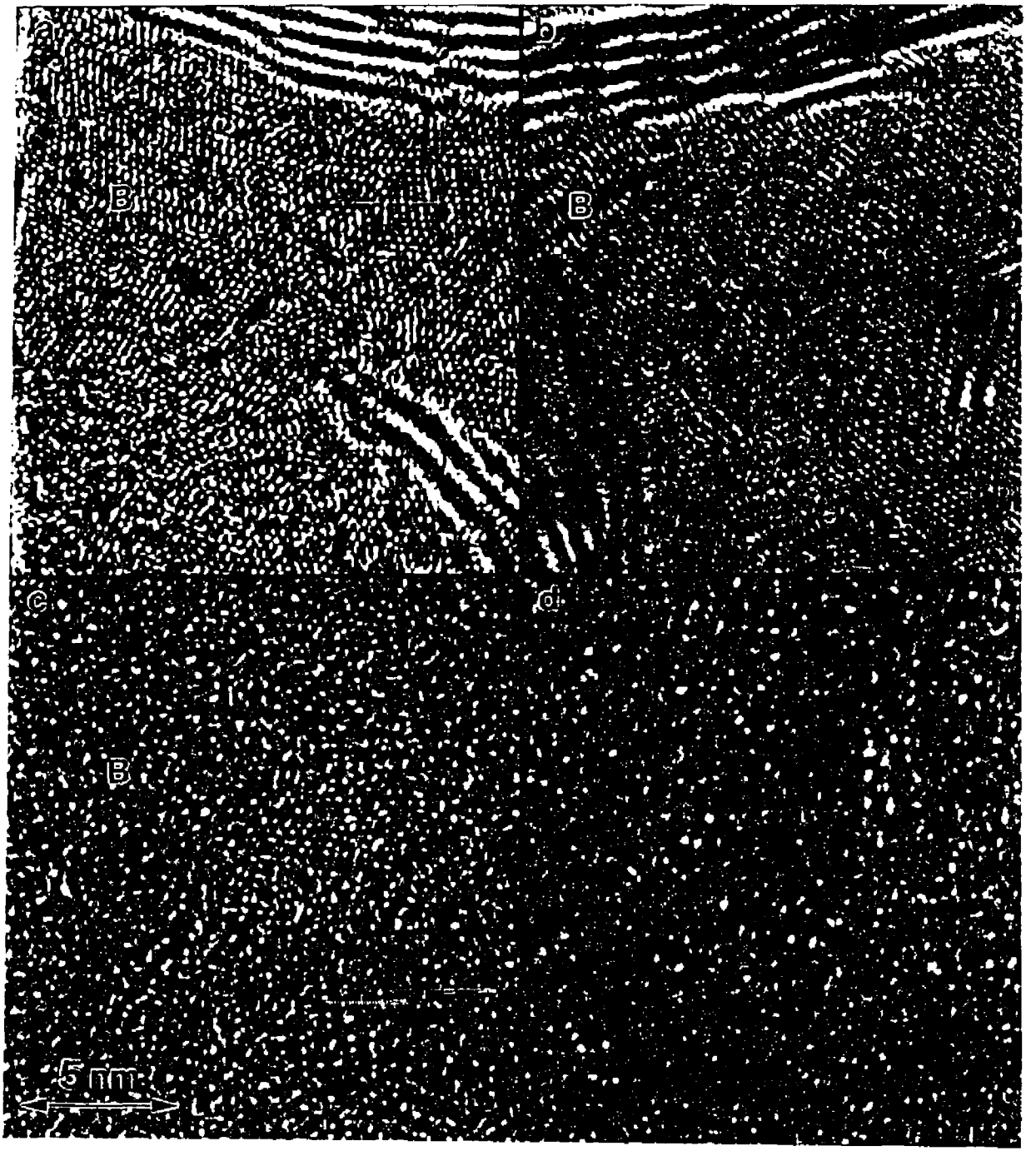

Figure 6.20. Montage of images, recorded at higher magnification, from regions in Figure 6.19. Primarily basal orientation (denoted by **B**) is apparent in c) in contrast to (a) and (b), while the films in d) possess a very short range order, similar to ones in Figure 6.17(d).

6.5 Discussion

6.5.1 *The effect of Substrate Temperature*

Pure sputter-deposited films are seen to be nanophase materials, which near the substrate consist primarily of basal oriented regions with edge oriented islands dispersed throughout. These basal oriented regions have nanometer scale grains, subgrains, or domains. The films underwent recrystallization during thermal annealing in UHV at 550°C, with the AT films being less stable than the HT films; this would be consistent with the shorter range order of the AT films. In the time periods studied (< 15 minutes) at 550°C, an atmosphere of 10^{-4} Pa of oxygen was required for MoO_3 to form. This agrees well with other oxidation studies (the morphology evolution as a function of oxidation and annealing conditions is presented in Table III) which report slightly lower temperatures, albeit, with higher oxygen pressures, e.g., in an *in situ* TEM study of MoS_2 flakes, Baker *et al*[244] observed MoO_3 formation at 527°C in 400 Pa of oxygen, while Kim and Lieber[245] using atomic force microscopy reported formation of MoO_3 on single crystal MoS_2 after atmospheric oxygen exposure at 480°C for 10 minutes.

The occurrence of thermally induced recrystallization complicates the studies of the kinetics of MoS_2 oxidation that would use higher temperatures to accelerate reactions (and obtain activation energies). In pure oxygen, without water vapor, in the conditions studied, recrystallization was seen to occur either before or with oxidation. Of greater interest is the study of MoS_2 oxidation in humid air environments, which can occur at room temperature. These experiments would, however, need to be conducted within

Table III

Summary of the morphological data on AT and HT films as a function of annealing and oxidation treatments

	AT FILMS	HT FILMS
As-grown Morphology	Basal and edge islands	Edge, longer range basal
Anneal @ 400°C	Small Domain Nucleation	No change
Anneal @ 550°C	Domain Size Increase	Small Domain Nucleation
Anneal @ 550°C in 10^{-4} O_2	Inhomogeneous MoO_3 nucleation	Not performed
Anneal @ 700-800°C in 10^{-4} O_2	Complete oxidation to MoO_3	Not performed
Au Growth on Pristine and annealed films	Textured 3D island growth	Textured 3D island growth

time-temperature combinations that avoid such recrystallization. These experiments with the UHV-HREM facility indicate that the instrument provides a useful pathfinder capability in kinetics experiments to find such transformation boundaries with limited samples quickly. Once known, these boundaries help to define an experimental matrix consisting of several samples at different annealing conditions. After thermal processing, these samples can be characterized by conventional TEM.

6.5.2 *The effect of Au-Pd Multilayers*

Nanostructures of multilayer metal-MoS_2 films are shown to be more complex than the simple model originally proposed[230], of alternating continuous layers of metal and basal-oriented MoS_2. Au-Pd in the low flux regime, in these multilayer films, consists of 3D islands that are not continuous; higher concentrations appear to lead to coalescence of islands to form quasi-continuous layers. (It should also be noted that the presence of a 2D layer under these islands cannot be ruled out.)

A key finding of this investigation is that some edge island orientation was present in these films, which could not be detected by a companion XRD study of thicker films of the same composition (carried out at Aerospace Corporation, CA). Thicker films grown at this pressure without metal layers develop mixed orientations of basal and edge oriented grains that are detected by XRD[230]. The periodic interruption of MoS_2 deposition, and incorporation of Au-Pd appears to be blocking the elongation of edge islands and repeatedly capturing a largely, but not exclusively, basal-oriented near-

interface nanostructure of MoS_2; this could possibly explain the absence of the edge plane reflections in the XRD data.

The difference in metal continuity between the low and high flux films provides some insight to the indentation and rolling contact data of Hopple *et al*[220], which showed that the high flux films had better fracture/spallation resistance than the low flux ones. Multilayers do not directly enhance the fracture toughness of the film against lateral cracks running parallel to the film-substrate interface[246]. Instead, these multilayer toughening mechanisms can inhibit the propagation of radial cracks perpendicular to the film-substrate interface. Extensions of these radial cracks relieve tensile hoop stresses that would otherwise restrain lateral crack propagation. In the low flux films, these propagating cracks probably encounter the Au particles, which may blunt cracks more than pure MoS_2 films while in the high flux case, it is probable that continuous metal layers generate more surface area or metal volume that blunt cracks more effectively.

Another benefit of such multilayer MoS_2 films might be improved oxidation resistance. The high degree of basal orientation of multilayer MoS_2 is expected to provide these films with superior resistance to oxidation in humid storage[226]. Continuous layers of Au-Pd should improve oxidation resistance even further.

6.5.3 *The effect of co-sputtering Ni and SbO_x*

Incorporation of Ni or SbO_x above a critical amount results in the relative suppression of edge island growth. For films containing 9% Ni, a predominance of basal

islands is observed. The HREM data agree with the hypothesis from EXAFS data that the majority of Ni is dispersed in small disordered clusters of Ni-oxide. The presence of Ni-oxide appears to interrupt or suppress the rapid growth of edge islands, which allows the basal islands to grow. For films containing 20% SbO_x, no crystalline order was detected by TED. HREM detected only fragments of edge islands in the 50 seconds films while both the population and density of these islands increased in the 150 seconds case. The HREM and TED data are consistent with EXAFS in that little order was detected in the basal island regions of the SbO_x-MoS_2 films.

There is one aspect of the EXAFS data that the current study could not confirm--the existence of the $MoS_{2-y}O_y$ phase. This is because neither HREM, nor TED has sufficient resolution to distinguish between the MoS_2 and $MoS_{2-y}O_y$ phases, which are isostructural. Further, discernment is strongly complicated by the possibility that the two phases could be physically overlapping in various regions (HREM/TED data represent superimposed information through the film regions). Note that the EXAFS study[242] reported that the SbO_x-MoS_2 films have a large concentration of the $MoS_{2-y}O_y$ phase relative to the MoS_2 phase. The general disorder in the SbO_x-MoS_2 films may be due, in part, to the large presence of $MoS_{2-y}O_y$ clusters whose formation are promoted by oxygen transfer from SbO_x.

Thus, the results from the study are in good agreement with those reported from EXAFS studies which suggest that Ni and SbO_x promote densification by different means. Ni forms Ni-oxide which retards the rapid growth of edge islands, allowing basal islands to form. SbO_x promotes the formation of $MoS_{2-y}O_y$, creating many clusters of material

having short-range order. However, the microstructural differences observed in the HREM data may be due to concentration effects. Future studies of the effects of cosputtered metal or oxides on MoS_2 film growth should include SbO_x of less than 20%, and Ni of greater than 9%. Studies of cosputtered Au would be helpful to compare with data on Au-Pd multilayer MoS_2 films. This data will provide insight to better control the endurance and environmental stability of cosputtered and multilayer MoS_2 lubricant films.

7. CONCLUSIONS

7.1 Summary

The goal of this thesis study was to elucidate different structural characteristics of certain semiconductor systems, i.e., Si(001), GaAs(100), and MoS_2, using HREM and TED data recorded under both UHV and conventional vacuum conditions. The outcomes of the investigations conducted in this regard were:

a) Determination of the atomic structure of a clean Si(001) surface.

b) A quantitative description of the morphology map of Ag deposits on these surfaces at room temperature, and of the chemical identity and geometric arrangement in the annealed Au-Si(001) system.

c) Demonstration of the role of the substrate cleanliness on the final chemical and structural aspects of the Au-GaAs interface, and

d) Illustration of the influence of deposition parameters on the final morphology (and therefore the tribological properties) of MoS_2 solid lubricant thin films.

The results from the Si(001) system in particular have important ramifications for future studies using the UHV-HREM facility. In fact, the clean surface preparation provided the first true test for the facility since the structure de-reconstructed under atomic hydrogen, limiting the data collection lifetime to ~2 hours. (Typical survival lifetimes in earlier studies by my predecessors on relatively inert clean surfaces of

Au(001), Si(111), and Ir(001) were on the order of a few days to a week.) Modifications made to the pumping line in the microscope column in this regard increased this period to 3-4 hours implying that it is now possible to record information from such reactive surfaces on a rather routine basis. Aside from the instrumentation aspect, these studies have also highlighted the considerable progress made by the UHV-HREM group in the field of data analysis for retrieval of surface structure information.

In specific, the results on the structure of the Si(001)-2x1 and the Si(001)-5x3-Au surfaces demonstrate the potency of quantitative interpretation of TED and HREM data respectively, in such analyses. Accuracies down to 0.005nm enabled a conclusive prediction of the asymmetric dimer model for the Si(001)-2x1 surface. In contrast to the asymmetric structure predicted by earlier studies[98,99,108-114], the model resulting from the TED analysis had second layer atoms moving off the bulk locations, but not towards each other. This detection was possible due to the higher sensitivity of TED to the in-plane displacements; collection of better data sets (defocussed beams) would enable comparison against the p(2x2) and c(4x2) structures, which are reported to be more stable[125,126]. Quantitative HREM analysis on the other hand facilitated determination of features (that were not resolved by the only other real-space study of the Si(001)-5x3-Au surface[149]), i.e., the identity of the species on the surface stripe and in the trench, and was able to advance a reason for the surface layer compression.

When such high levels of precision are not required, a less rigorous approach can be used, as demonstrated in the study of Ag deposits on clean Si(001) surfaces. The investigation revealed structural details about small particle morphologies that had

eluded observation by other techniques for over a decade and highlighted the importance of the initial stages of nucleation and growth in determining the final thin film morphology (a phase map was also predicted in this regard). A good demonstration of this relationship was the polycrystalline nature of the 5nm thick Au-Pd deposits on MoS_2 which evolved from the coalescence of the MTP's and Sc's (seen in the 1.5nm thick Au-Pd films). These investigations in unison emphasized the need for well-controlled UHV conditions in surface analyses.

However, the main limitation of these studies was the lack of a powerful tool for surface chemical analyses, as illustrated by the results of the Au-GaAs(001) (where XPS confirmed the alloy existence) and Si(001)-Au-5x3 (where lack of XPS and AES precluded comment on alloy existence, either at room temperature or on annealing) systems. The successful installation and operation of SPEAR should enable a more extensive characterization of the surface geometric structure and chemistry in these systems and the following section highlights some of the areas for future studies.

7.2 Suggestions for future work

7.2.1 *Ag on Si(001)-2x1*

Three issues of importance that still need to be addressed with this system are the actual growth mode, the structure and saturation coverage of the 2D layer, and the evolution of the morphologies at higher coverages. Both the on-zone and off-zone HREM images were fairly inconclusive on the existence of a 2D layer at the few monolayer

growth regime investigated in the study, i.e., it was difficult to determine if growth mode was either the SK or VW type. A more comprehensive study involving a combination of UHV-HREM and AES techniques, as a function of deposition from the very initial stages, should shed light on this aspect. If the growth mode is revealed to be SK, it should be possible to determine the saturation coverage of the 2D layer and the transition between the 2D and 3D layer growth, and therefore comment on the pseudo-SK growth mode reported by STM[162]. Also, for the 2D layers in these cases it would be imperative to perform a quantitative analysis of the HREM data to resolve the manner in which Ag atoms adsorb on the Si(001)-2x1 substrate; the rectangular shape of the Sc's observed in the current study could probably then be explained on the basis of these results.

The initial stages of formation of the 3D islands also need to be documented to observe any kind of transition in the behavior of the different morphologies. In specific, strong interfacial forces were hypothesized to be responsible for both the very small percentage of Ic MTP's and their preferential <112> orientation; study at lower coverages (than the ones in the current study) might test the assumption. It would also be interesting to chart the evolution of the morphologies at the other end of the spectrum, i.e., as a function of increasing coverage (in the few tens of nm range) to test the phase map predicted in Figure 4.11.

7.2.2 *Si(001)-Au-5x3*

One of the fundamental questions that needs to be answered in this system is the

behavior of Au deposits at room temperature, both in terms of structure and chemistry. The growth mode in the system was not investigated in the current study and if 3D islands exist, it would of interest to characterize their morphology (and contrast to the Ag/Si(001) results). Current TED data suggest formation of a gold-silicide compound in the initial stages of deposition. This issue can be resolved by using the TED data in combination with XPS and AES results on the surface. Also of interest would be the critical thickness value at which the silicide forms. Further, the structural evolution of such an alloy should be carried out as a function of annealing to determine whether it co-exists with the surface reconstruction and if so, its contribution to the A and B-type features in the TED patterns, e.g., Figure 4.14.

Spectroscopy data from such annealed (and reconstructed) surfaces would enable estimation of the concentration of Au in the first few layers and test the model advanced in Figure 4.19. Finally, although not attempted in the current study, a rigorous quantitative analyses of TED data can also be carried out (similar to that carried out for the Si(001)-2x1 surface) as a consistency check.

7.2.3 *GaAs(001)*

Since one of the motivations behind the attempted study was to characterize the structure of the surface, the primary goal would be to obtain such reconstructed surfaces through some judicious combination of gentle ion milling, annealing temperature and

arsenic backpressure. Once such surfaces are obtained, the associated atomic arrangement needs to be understood (via quantitative analyses of HREM and/or TED data) prior to attempting studies of metal deposition. In the latter, the issue of alloy formation and the associated critical coverage will have to be addressed for Au deposits on these clean surfaces, and contrasted against the results detailed in Chapter 5.

7.2.4 MoS_2

As mentioned in the discussion section in chapter 6, of practical importance is a study of the oxidation behavior of MoS_2 in humid air environments (necessitate an environmental cell). It would be interesting to characterize the HT and AT films, and also the co-sputtered and multilayer metal-MoS_2 films on this basis and obtain a microstructure-property correlation. Also, a drawback with the current investigations was that the films were deposited *ex situ* and therefore, the role of the contaminants, e.g., in influencing the morphology of Au and Au-Pd islands, is not immediately clear. In this respect, a sputter deposition chamber should be added to one of the ports on the SPEAR to permit UHV deposition since this would enable strict control over the deposition parameters and therefore, the final microstructure and stoichiometry of the films.

REFERENCES

1. Woodruff, D. P; Delchar, T. A. *Modern techniques of surface science*; Cambridge University: Cambridge, 1986.

2. Wood, E. A. *J. Appl. Phys.* **1964,** *35,* 1306.

3. LaFemina, J. P. *Surf. Sci. Rep.* **1992,** *16,* 133.

4. Venables, J. A.; Spiller, G. D. T.; Hanbücken, M. *Rep. Prog. Phys.* **1984,** *47,* 399.

5. Zangwill, A. *Physics at surfaces;* Cambridge University: Cambridge, 1988.

6. Osakabe, N.; Tanashiro, Y.; Yagi, K. *Surf. Sci.* **1981,** *109,* 353.

7. Yagi, K.; Yamanaka, A.; Yamaguchi, H. *Surf. Sci.* **1993,** *283,* 300.

8. Yamaguchi, H.; Tanashiro, Y.; Yagi, K. *Appl. Surf. Sci.* **1992,** *60/61,* 79.

9. Alfonso, C.; Bermond, J. M.; Heyraud, J. C.; Métois, J. J. *Surf. Sci.* **1992,** *262,* 371.

10. Ma, Y.; Lordi, S.; Larsen, P. K.; Eades, J. A. *Surf. Sci.* **1993,** *289,* 47.

11. Larsen, P. K.; Meyer-Ehmsen, G. *Surf. Sci.* **1990,** *240,* 168.

12. Bolger, B.; Larsen, P. K. *Rev. Sci. Instrum.* **1986,** *57,* 1363.

13. Telieps, W.; Bauer, E. *Surf. Sci.* **1985,** *162,* 163.

14. Mundschau, M.; Bauer, E.; Telieps W.; Swiech, W. *Surf. Sci.* **1989,** *223,* 413.

15. Tromp, R. M.; Reuter, M. C. *Phys. Rev. Lett.* **1992,** *68,* 820.

16. Phaneuf, R. J.; Bartelt, N. C.; Williams, E. D.; Swiech W.; Bauer, E. *Phys. Rev. Lett.* **1991,** *21,* 2986.

17. Mundschau, M.; Bauer, E.; Telieps, W.; Swiech, W. *Surf. Sci.* **1989,** *213,* 381.

18. Mundschau, M.; Bauer, E.; Telieps, W.; Swiech, W. *J. Appl. Phys.* **1989,** *65,* 4747.

19. Mundschau, M.; Bauer, E.; Swiech, W. *J. Appl. Phys.* **1989,** *65,* 581.

20. Tersoff, J.; Denier van der Gon, A. W.; Tromp, R. M. *Phys. Rev. Lett.* **1993,** *70,* 1143.

21. Schlier, R. E.; Farnsworth, H. E. *J. Chem. Phys.* **1959,** *30,* 917.

22. Tong, S. Y.; Maldonado, A. L. *Surf. Sci.* **1978,** *78,* 459.

23. Veneklasen, L. H.; *Rev. Sci. Instrum.* **1992,** *63,* 5513.

24. Altman, M. S.; Pinkvos, H.; Hurst, J.; Poppa, H.; Marx, G.; Bauer, E. In *Proceedings of the Materials Research Society*; Sugita, Y.; Clemens, B. M.; Laughlin, D. E.; Ouchi, K.; Suzuki, T., Eds.; MRS Symposium Series 232, North-Holland: New York, 1991; p. 125.

25. Ertl, G. *Science* **1991,** *254,* 1750.

26. Bauer, E.; Mundschau, M.; Swiech, W.; Telieps, W. *Ultramic.* **1989,** *31,* 49.

27. Engel, W.; Kordesch, M. E.; Rotermund, H. H.; Kubala, S.; Oertzen, A. V. *Ultramic.* **1991,** *36,* 164.

28. Griffith, O. H.; Rempfer, G. F. *Adv. in Opt. and Elect. Microsc.* **1987,** *10,* 270.

29. Sato, H.; Tanashiro Y.; Yagi, K. *Appl. Surf. Sci.* **1992,** *60/61,* 367.

30. Tonner, B. P. *Nucl. Inst. and Meth.* A **1991,** *291,* 60.

31. Rempfer, G.; Mauck, M. S. *Optik* **1992,** *92,* 3.

32. Venables, J. A.; Smith, D. J.; Cowley, J. M. *Surf. Sci.* **1987,** *181,* 235.

33. Jones, G. W.; Venables, J. A. *Ultramic.* **1985,** *18,* 439.

34. Futamoto, M.; Hanbücken, M.; Harland, C. J.; Jones, G. W.; Venables, J. A. *Surf. Sci. 1985, 150,* 430.

35. Harland, C. J.; Venables, J. A. *Ultramic.* **1985,** *17,* 17.

36. Hembree, G. G.; Venables, J. A. *Ultramic.* **1992,** *47,* 109.

37. Drucker, J.; Krishnamurthy, M.; Hembree, G. *Ultramic.* **1991,** *35,* 323.

38. Drucker, J.; Scheinfein, M. R. *Phys. Rev.* B **1993,** *47,* 4068.

39. Liu, J.; Cowley, J. M. *Ultramic.* **1993,** *48,* 381.

40. Feenstra, R. M.; Lutz, M. A. *Surf. Sci.* **1991,** *243,* 151.

41. Giesen, M.; Frohn, J.; Poensgen, M.; Wolf, J. F.; Ibach, H. *J. Vac. Sci. Technol.*A **1992,** *10,* 597.

42. Kitamura, N.; Webb, M. B. *Bull. Am. Phys. Soc.* **1993,** *38,* 509.

43. Lagally, M. G.; Mo, Y. W.; Kariotis, R.; Swartzentruber, B. S.; Webb, M. B. In *Kinetics of Ordering and Growth at Surfaces;* Lagally, M. G., Ed.; Plenum: New York, 1990; p. 40.

44. Bennett, P. A.; Copel, M.; Cahill, D.; Falta, J.; Tromp, R. M. *Phys. Rev. Lett.* **1992,** *69,* 1224.

45. Dunn, D. N.; Xu, P.; Marks, L. D. *J. Cryst. Growth* **1992,** *125,* 543.

46. Hana, Y; Takayanagi, K. *Ultramic.* **1992,** *45,* 95.

47. Dunn, D. N.; Xu, P.; Marks, L. D. *Surf. Sci.* **1993,** *294,* 308.

48. Ross, F. M.; Gibson, J. M. *Phys. Rev. Lett.* **1992,** *68,* 1782.

49. Yagi, K.; Yamana, A.; Sato, H.; Shima, M.; Ohse, H.; Ozawa, S.; Tanashiro, Y. *Prog. Theor. Phys. Suppl.* **1991,** *106,* 303.

50. Honjo, G.; Takayanagi, K.; Kobayashi, K.; Yagi, K. *J. Cryst. Growth* **1977,** *42,* 98.

51. Takayanagi, K.; Tanashiro, Y.; Takahashi, S.; Takahashi, M. *Surf. Sci.* **1985,** *164,* 367.

52. Gibson, J. M. *Surf. Sci. Lett.* **1990,** *239,* L531.

53. Twesten, R. D.; Gibson, J. M. *Ultramic.* **1994,** *53(3),* 223.

54. Marks, L. D.; Xu, P.; Dunn, D. N. *Surf. Sci.* **1993,** *294,* 322.

55. Hirsch, P.; Howie, A.; Nicholson, R. B.; Pashley, D. W.; Whelan, M. J. *Electron Microscopy of Thin Crystals;* Robert Krieger: Florida, 1977.

56. *Electron Diffraction Techniques;* Cowley, J. M., Ed.; Oxford University: New York, 1992.

57. Cowley, J. M. *Diffraction Physics*; Elsevier Science: The Netherlands, 1990; Vol.1.

58. Spence, J. C. H. *Experimental High-Resolution Electron Microscopy;* Oxford University: New York, 1988.

59. Cowley, J. M.; Moodie, A. F. *Acta Cryst.* **1957**, *10,* 609

60. Marks, L. D. In *Topics in Current Physics;* Schommers, W.; von Blanckenhagen, P., Eds.; Springer-Verlag: Berlin, 1986; Vol. 41, p. 71.

61. Cherns, D. *Philos. Mag.* **1974,** *30,* 549.

62. Lempfuhl, G.; Uchida, Y. *Ultramic.* **1979,** *4,* 275.

63. Iijima, S. *Ultramic.* **1981,** *6,* 41.

64. Krakow, W.; Ast, D. G. *Surf. Sci.* **1976,** *58,* 485.

65. Kambe, K.; Lehmpfuhl, G. *Optik* **1975,** *42,* 187.

66. Moodie, A. F.; Warble, C. E. *Philos. Mag.* **1967,** *16,* 891.

67. Smith, D. J. In *Chemistry and Physics of Solid Surfaces VI;* Vanselow, R.; Howe, R., Eds.; Springer-Verlag: Berlin, 1986; Chapter 15.

68. Cowley, J. M. *J. Vac. Sci. Technol.*A **1989,** *7,* 2823.

69. Cowley, J. M. *Prog. Surf. Sci.* **1986,** *21,* 209.

70. Marks, L. D. *Surf. Sci.* **1984,** *139,* 281.

71. Marks, L. D. *Phys. Rev. Lett.* **1983,** *51,* 1000.

72. Marks, L. D.; Smith, D. J. *Nature* **1983,** *303,* 316.

73. Ikarashi, N.; Kobayashi, K.; Hoike, H.; Hasegawa H.; Yagi, K. *Ultramic.* **1988,** *26,* 195.

74. Gibson, J. M.; McDonald, M. L.; Unterwald, F. C. *Phys. Rev. Lett.* **1985,** *55,* 1765.

75. Mitome, M.; Takayanagi, K. *Surf. Sci.* **1991,** *242,* 69.

76. Lu, P.; Smith, D. J. *Phys. Rev. Lett.* **1987,** *59,* 2177.

77. Ennos, A. E. *Br. J. Appl. Phys.* **1953,** *4,* 101.

78. Bassett, G. A. In *Proceedings of the International Symposium on Condensation and Evaporation of Solids*; Rutner, E.; Goldfinger, P.; Hirth, J. P., Eds.; Gordon and Breach: New York, 1962; p. 599.

79. Poppa, H. *J. Vac. Sci. Technol.* **1965,** *2,* 42.

80. Barna, A.; Barna, P. B.; Pocza, J. F. *Vacuum* **1967,** *17,* 2.

81. Wilson, R. J.; Petroff, P. M. *Rev. Sci. Instrum.* **1983,** *54,* 1534.

82. Moorhead, R. D.; Poppa, H. In *Proceedings of the 27th Annual Meeting of the Electron Microscopy Society of America*; Arceneaux, C. J., Ed.; San Francisco Press: San Francisco, 1969; p. 116.

83. Valdré, U.; Robinson, E. A.; Pashley, D. W.; Stowell, M. J.; Law, T. J. *J. Phys.* E **1970,** *3,* 501.

84. Métois, J. J.; Nitsche, S.; Heyraud, J. C. *Ultramic.* **1989,** *27,* 349.

85. McDonald, M. L.; Gibson, J. M.; Unterwald, F. C. *Rev. Sci. Instrum.* **1989,** *60,* 700.

86. Marshall, M. T.; Tong, X.; Gibson, J. M. In *Proceedings of the 51st Annual Meeting of the Electron Microscopy Society of America;* Bailey, G. W.; Rieder, C. L., Eds.; San Francisco Press: San Francisco, 1993; p. 640.

87. Poppa, H.; Heinemann, K.; Elliot, A. G. *J. Vac. Sci. Technol.* **1971,** *8,* 471.

88. Smith, D. J.; Gajdardziska-Josifovska, M.; Lu, P.; McCartney, M. R.; Podbrdsky, J.; Swann, P. R.; Jones, J. S. *Ultramic.* **1993,** *49,* 26.

89. Schlier, R. E.; Farnsworth, H. E. In Semiconductor Surface Physics; University of Pennsylvania Press: Philadelphia, 1957; p. 3.

90. Lander, J. J.; Morrison, J. *J. Chem. Phys.* **1962,** *37,* 729.

91. Poppendieck, T. D.; Ngoc, T. C.; Webb, M. B. *Surf. Sci.* **1978,** *75,* 287.

92. Müller, K.; Lang, E.; Hammer, L.; Grim, W.; Heilman, P.; Heinz, K. In Determination of Surface Structure by LEED; Marcus, P. M.; Jona, F., Eds.; Plenum: New York, 1984; p. 483.

93. Wang, H. -C.; Lin, R. -F.; Wang, X. *Phys. Rev.* B **1987,** *36,* 7712.

94. Martin, J. A.; Savage, D. E.; Moritz, W.; Lagally, M. G. *Phys. Rev. Lett.* **1986,** *56,* 936.

95. Aruga, T.; Murata, Y. *Phys. Rev.* B **1986,** *34,* 5654.

96. Seiwatz, R. *Surf. Sci.* **1964,** *2,* 473.

97. Jona, F.; Shih, H. D.; Ignatiev, A.; Jepson, D. W.; Marcus, P. M. *J. Phys.* C **1977,** *10,* L67.

98. Chadi, D. J. *Phys. Rev. Lett.* **1979,** *43,* 43.

99. Chadi, D. J. *J. Vac. Sci. Technol.* **1979,** *16,* 1290.

100. Rowe, J. E. *Phys. Lett.* A **1974,** *46,* 400.

101. Himpsel, F. J.; Eastman, D. E. *J. Vac. Sci. Technol.* **1979,** *16,* 1302.

102. Alerhand, O. L.; Mele, E. J. *Phys. Rev.* B **1987,** *35,* 5533.

103. Appelbaum, J. A.; Hamann, D. A. *Surf. Sci.* **1978,** *74,* 21.

104. Tromp, R. M., Smeenk, R. G.; Saris, F. W. *Phys. Rev. Lett.* **1981,** *46,* 939.

105. Aono, M.; Hou, Y.; Oshima, C.; Ishizawa, Y. *Phys. Rev. Lett.* **1982,** *49,* 567.

106. Appelbaum, J. A.; Baraff, G. A.; Hammann, D. R. *Phys. Rev.* B **1975,** *12,* 5749.

107. Kerker, G. P.; Louie, S. G.; Cohen, M. L. *Phys. Rev.* B **1978,** *17,* 706.

108. Yin, M. T.; Cohen, M. L. *Phys. Rev.* B **1981,** *24,* 2303.

109. Roberts, N.; Needs, R. J. *Surf. Sci.* **1990,** *236,* 112.

110. Yang, W. S.; Jona, F.; Marcus, P. M. *Sol. Stat. Commun.* **1982,** *43(11),* 847.

111. Yang, W. S.; Jona, F.; Marcus, P. M. *Phys. Rev.* B **1983,** *28,* 2049.

112. Holland, B. W.; Duke, C. B.; Paton, A. In *Proceedings of 17th International Conference on the Physics of Semiconductors;* Chadi, D. J.; Harrison, W. A., Eds.; Springer: Berlin, 1984; p. 55.

113. Jedrecy, N.; Sauvage-Simkin, M.; Pinchaux, R.; Massies, J.; Greiser, N.; Etgens, V. H. Surf. Sci. **1990,** *230,* 197.

114. Shkrebtii, A. I.; Del Sole, R. *Phys. Rev. Lett.* **1993,** *70,* 2645.

115. Bring, R. S.; Verwoerd, W. S. *Surf. Sci.* **1985,** *154,* L203.

116. Ong, C. K.; Chan, B. C. *J. Phys.: Condens. Matter* **1989,** *1,* 3931.

117. Bechstedt, F.; Reichardt, D. *Surf. Sci.* **1988,** *202,* 83.

118. Batra, I. P. *Phys. Rev.* B **1990,** *41,* 5048.

119. Weakliem, P. C.; Carter, E. A. *J. Chem. Phys.* **1992,** *96,* 3240.

120. Tang, S.; Freeman, A. J.; Delley, B. *Phys. Rev.* B **1992,** *45,* 1776.

121. Tromp, R. M.; Hamers, R. J.; Demuth, J. E. *Phys. Rev. Lett.* **1985,** *55,* 1303.

122. Hamers, R. J.; Tromp, R. M.; Demuth, J. E. *Phys. Rev.* B **1986,** *34,* 5343.

123. Wolkow, R. A. *Phys. Rev. Lett.* **1992,** *68,* 2636.

124. Weakliem, P. C.; Smith, G. W.; Carter, E. A. *Surf. Sci. Lett.* **1990,** *232,* L219.

125. Garcia, A; Northrup, J. E. *Phys. Rev.* B **1993,** *48,* 17350.

126. Ramstad, A.; Brocks, G.; Kelly, P. J. *Phys. Rev.* B **1995,** *51,* 14504.

127. Boland, J. J. *Phys. Rev. Lett.* **1990,** *65,* 3325.

128. Sakurai, T.; Hagstrom, H. D. *Phys. Rev.* B **1976,** *14,* 1593.

129. Frank, J. In *Computer Processing of Electron Microscope Images;* Hawkes, P. W., Ed.; Springer-Verlag: New York, 1980; p. 187.

130. Buckett, M. I.; Marks, L. D.; Luzzi, D. E. In *Proceedings of the 45th Annual Meeting of the Electron Microscopy Society of America,* San Francisco Press: San Francisco, 1987; p. 752.

131. Marks, L. D., in preparation.

132. Dennis, J. E. Dennis; Gay, D. M.; Welsch, R. E. *ACM Trans. Math. Software* **1981,** *7,* 348.

133. Marks, L. D. *Ultramic.* **1992,** *45,* 145.

134. Mazur, A.; Pollmann, J. *Surf. Sci.* **1990,** *225,* 72.

135. Rideout, V. L. *Sol. Stat. Elec.* **1975,** *18,* 541.

136. Heslinga, D. R.; Weitering, H. H.; van der Werf, D. P.; Klapwijk, T. M.; Hibma, T. *Phys. Rev. Lett.* **1990,** *64,* 1589.

137. Tung, R. T.; Levi, A. F. J.; Sullivan, J. P.; Schrey, F. *Phys. Rev. Lett.* **1991,** *66,* 72.

138. Weitering, H. H.; Sullivan, J. P.; Carolissen, R. J.; Graham, W. R.; Tung, R. T. *Appl. Surf. Sci.* **1993,** *70/71,* 422.

139. Samsavar, A.; Miller, T.; Chiang, T.-C. *Phys. Rev.* B **1988,** *38,* 9889.

140. Nishimori, K.; Tokutaka, H.; Tamon, T.; Kishida. S; Ishihara, N. *Surf. Sci.* **1991,** *242,* 157.

141. Hricovini, K.; Bonnet, J. E.; Carrière, B.; Deville, J. P.; Hanbücken, M.; LeLay, G. *Surf. Sci.* **1989,** *211/212,* 630.

142. Hanbücken, M.; Imam, Z.; Métois, J. J.; LeLay, G. *Surf. Sci.* **1985,** *162,* 628.

143. Hiraki, A. *Surf. Sci.* **1986,** *168,* 74.

144. Narusawa, T.; Kinoshita, K.; Gibson, W. M.; Hiraki, A. *J. Vac. Sci. Technol.* **1981,** *18,* 872.

145. Oura, K.; Makino, Y.; Hanawa, T. *Jap. J. Appl. Phys.* **1976,** *15,* 737.

146. Oura, K.; Hanawa, T. *Surf. Sci.* **1979,** *82,* 202.

147. Green, A. K.; Bauer, E. *Surf. Sci.* **1981,** *103,* L127.

148. Lu, Z. H.; Sham, T. K.; Norton, P. R. *Sol. Stat. Commun.* **1993,** *85,* 957.

149. Lin, X. F.; Wan, K. J.; Glueckstein, J. C.; Nogami, J. *Phys. Rev.* B **1993,** *47,* 3671.

150. Samsavar, A.; Hirschorn, E. S.; Leisble, F. M.; Chiang, T. -C. *Phys. Rev. Lett.* **1989,** *63,* 2830.

151. Hashizume, T.; Hamers, R. J.; Demuth, J. E.; Markert, K.; Sakurai, T. *J. Vac. Sci. Technol.* A **1990,** *8,* 249.

152. Brodde, A.; Badt, D.; Tosch, St.; Neddermeyer, H. *J. Vac. Sci. Technol.* A **1990,** *8,* 251.

153. Lin, X. F.; Wan, K. J.; Nogami, J. *Phys. Rev.* B **1993,** *47,* 10947.

154. Lin, X. F.; Wan, K. J.; Nogami, J. *Phys. Rev.* B **1993,** *47,* 13491.

155. Hanawa, T.; Oura, K. *Jap. J. Appl. Phys.* **1977,** *16,* 519.

156. Hanbücken, M.; Neddermeyer, H. *Surf. Sci.* **1982,** *114,* 563.

157. Hanbücken, M.; Neddermeyer, H.; Rupieper, P. *Thin Solid Films* **1982,** *90,* 37.

158. Hanbücken, M.; Futamoto, M.; Venables, J. A. *Surf. Sci.* **1984,** *147,* 433.

159. Hanbücken, M.; LeLay, G. *Surf. Sci.* **1986,** *168,* 122.

160. Borensztein, Y.; Alameh, R. *Appl. Surf. Sci.* **1993,** *65/66,* 735.

161. Kimura, Y.; Takayanagi, K. *Surf. Sci.* **1992,** *276,* 166.

162. Winau. D.; Itoh, H.; Schmid, A. K.; Ichinokawa, T. *Surf. Sci.* **1994,** *303,* 139.

163. Luo, F. C. H.; Hembree, G. G.; Venables, J. A. In *Proceedings of the Materials Research Society;* Thompson, C. V.; Tsao, J. Y.; Srolovitz, D. J. Eds.; North-Holland: New York, MRS Series 49, 1992; p. 202.

164. Shirokoff, J.; Erb, U. Philos. Mag. Lett. **1988,** *58,* 255.

165. Ino, S. *J. Phys. Soc. Jpn.* **1966,** *21,* 346.

166. Marks, L. D.; Smith, D. J. *J. Cryst. Growth* **1981,** *54,* 425.

167. Marks, L. D., submitted for publication in *Ultramic.*

168. Doraiswamy, N.; Marks, L. D. *Philos. Mag.* **1995,** *71,* 271.

169. Buffat, P. A.; Flueli, M.; Spycher, R.; Stadelmann, P.; Borel, J. P. *Faraday Discuss.* **1991,** *92,* 173.

170. Gillet, M. *Surf. Sci.* **1977,** *67,* 139.

171. Altenheim, C.; Giorgio, S.; Urban, J.; Weiss, K. *Z. Phys. D* **1991,** *19,* 303.

172. Allpress, J. G.; Sanders, J. V. *Surf. Sci.* **1967,** *7,* 1.

173. Marks, L. D. *Rep. Prog. Phys.* **1994,** *57,* 603.

174. Ino, S. *J. Phys. Soc. Jpn.* **1969,** *27,* 941.

175. Marks, L. D. *Philos. Mag. A* **1984,** *49,* 81.

176. Howie, A.; Marks, L. D. *Philos. Mag. A* **1984,** *49,* 95.

177. Ajayan, P. M.; Marks, L. D. *Phase Trans.* ***1990,*** *24,* 229.

178. Cleveland, C. L.; Landman, U. *J. Chem. Phys.* ***1991,*** *94,* 7376.

179. Winterbottom, W. L. *Acta Met.* **1967,** *15,* 303.

180. Yagi, K.; Takayanagi, K.; Kobayashi, K.; Honjo, G. *J. Cryst. Growth* **1975,** *28,* 117.

181. Bonevich, J. E.; Marks, L. D. *J. Mater. Res.* **1992,** *7,* 1489.

182. Iijima, S.; Ichihashi, T. *Phys. Rev. Lett.* **1986,** *56,* 616.

183. Honjo, G.; Takayanagi, K.; Kobayashi, K.; Yagi, K. *Phys. Stat. Sol. A* **1979,** *55,* 353.

184. Marks, L. D. *Thin Solid Films* **1986,** *136,* 309.

185. Smith, D. J.; Marks, L. D. *J. Cryst. Growth* **1981,** *54,* 433.

186. Haluska, M.; Kuzmany, H.; Vybornov, M.; Rogl, P.; Fejdi, P. *Appl. Phys.* **1993,** *56,* 61.

187. Zhou, R. -H.; Cao, P. -L.; Lee, L. -Q. *Surf. Sci. Lett.* **1993,** *290,* L649.

188. Meade, R. D.; Vanderbilt, D. In *The Structure of Surfaces III*; Tong, S. Y.; Van Hove, M. A.; Takayanagi, K.; Xie, X. D. Eds.; Springer-Verlag Berlin: Heidelberg, 1990; Vol. 24; p. 4.

189. Lin, X. F.; Nogami, J. *J. Vac. Sci. Technol. B* **1994,** *12,* 2090.

190. Marks, L. D., in preparation.

191. Sato, H.; Yagi, K. *J. Phys.: Condens. Matter* **1993,** *5,* 2095.

192. Petroff, P. M.; Wilson, R. J. *Phys. Rev. Lett.* **1983,** *51(3),* 199.

193. Marks, L. D.; Plass R., submitted for publication in *Phys. Rev. Lett.*

194. Chadi, D. J. *J. Vac. Sci. Technol. A* **1987,** *5,* 834.

191. Biegelsen, D. K.; Brigans, R. D.; Northrup, J. E.; Swartz, L. -E. *Phys. Rev. Lett.* **1990,** *65,* 452.

192. Drathen, P.; Ranke, W.; Jacobi, K. *Surf. Sci.* **1978,** *77,* L162.

193. Bachrach, R. Z.; Bauer, R. S.; Chiaradia, P.; Hansson, G. V. *J. Vac. Sci. Technol.* **1981,** *19,* 335.

194. Larsen, P. K.; van der Veen, J. F.; Mazur, A.; Pollmann, J.; Neave, J. H.; Joyce, B. A. *Phys. Rev. B* **1982,** *26,* 3222.

195. Larsen, P. K.; Neave, J. H.; van der Veen, J. F.; Dobson, P. J.; Joyce, B. A. *Phys. Rev. B* **1983,** *27,* 4966.

196. Chadi, D. J.; Tanner, C.; Ihm, J. *Surf. Sci.* **1982,** *120,* L425.

201. Chadi, D. J.; Ihm, J.; Tanner, C.; Joannopoulos, J. D. *Physica B* **1983,** *117/118,* 798.

202. Vandenberg, J. M.; Kinsbron, E. *Thin Solid Films* **1980,** *65,* 259.

203. Yoshiie, T.; Bauer, C. L.; Milnes, A. G. *Thin Solid Films* **1984,** *111,* 149.

204. Kim, T.; Chung, D. D. L. *Philos. Mag.* **1990,** *62,* 283.

205. Hiraki, A.; Kim, S.; Kammura, W.; Iwami, M. *Surf. Sci.* **1979,** *86,* 706.

206. Hu, Q. -H.; Kvist, A.; Andrén, H. -O. *Inst. Phys. Conf. Ser.* **1991,** *117(2),* 91.

207. Leung, S.; Milnes, A. G.; Chung, D. D. L. *Thin Solid Films* **1983,** *104,* 109.

208. Beam, E.; Chung, D. D. L. *Thin Solid Films* **1985,** *128,* 321.

209. Chung, D. D. L.; Beam, E. *Thin Solid Films* **1985,** *128,* 299.

210. Weizer, V. G.; Fatemi, N. S. *J. Appl. Phys.* **1988,** *64,* 4618.

211. Liliental-Weber, Z.; Gronsky, R.; Washburn, J.; Newman, N.; Spicer, W. E.; Weber, E. R. *J. Vac. Sci. Technol.* B **1986,** *4(4),* 912.

212. Watson, R. E.; Hudis, J.; Perlman, M. L. *Phys. Rev.* B **1971,** *4,* 4139.

213. Hilton, M. R.; Fleischauer, P. D. *Surf. and Coat. Technol.* **1992,** *54/55,* 435.

214. Hilton, M. R.; Fleischauer, P. D. In *Metals Handbook:* Friction, Lubrication and Wear Technology; ASM International: Materials Park, Ohio, **1992;** Vol. 18, p. 150.

215. Spalvins, T. *ASLE Trans.* **1971,** *14,* 267; **1973,** *17,* 1; *Thin Solid Films* **1982,** *96,* 17.

216. Hilton, M. R.; Fleischauer, P. D. In *Proceedings of the Material Research Society,* Eds.; MRS Symposium Series 140; North-Holland: New York, 1989; p. 227.

217. Hilton, M. R.; Fleischauer, P. D. *J. Mater. Res.* **1990,** *5(2),* 406.

218. Fleischauer, P. D.; Bauer, R. *Tribol. Trans.* **1988,** *31(2),* 239.

219. Hilton, M. R.; Bauer, R.; Fleischauer, P. D. *Thin Solid Films* **1990,** *188,* 216.

220. Hopple, G. B.; Keem, J. E.; Loewenthal, S. H. *Wear* **1993,** *162-164,* 919.

221. Hopple, G. B.; Loewenthal, S. H. *Surf. and Coat. Technol.* **1994,** *68/69,* 398.

222. Hilton, M. R. *Surf. and Coat. Technol.* **1994,** *68/69,* 407.

223. Loewenthal, S. H.; Chou, R. G.; Hopple, G. B.; Wenger, W. L. *Tribol. Trans.* **1994,** *37(3),* 505.

224. Fleischauer, P. D.; Bauer, R. *Tribol. Trans.* **1988,** *31(2),* 39.

225. Fleischauer, P. D.; Tolentino, L. U. In *Proceedings of the Third International Conference on Solid Lubrication*, American Society of Lubrication Engineers: Park Ridge, IL, 1984; S-14, p. 223.

226. Fleischauer, P. D. *ASLE Trans.* **1983,** *27(1),* 82.

227. Stewart, T. B.; Fleischauer, P. D. *Inorg. Chem.* **1982,** *21,* 2426.

228. Pope, L. E.; Panitz, J. K. G. *Surf. and Coat. Technol.* **1988,** *36,* 341.

229. Stupp, B. C. *Thin Solid Films* **1981,** *84,* 257.

230. Hilton, M. R.; Bauer, R.; Didziulis, S. V.; Dugger, M. T.; Keem, J.; Scholhamer, J. *Surf. and Coat. Technol.* **1992,** *53,* 13.

231. Niederhauser, P.; Hintermann, H. E.; Maillat, M. *Thin Solid Films* **1983,** *108,* 209.

232. Müller, C.; Menoud, C.; Maillat, M.; Hintermann, H. E. *Surf. and Coat. Technol.* **1988,** *36,* 351.

233. Aubert, A.; Nabot, J. Ph.; Etnoult, E.; Renoux, Ph. *Surf. and Coat. Technol.* **1990,** *41,* 127.

234. Bolster, R. N.; Singer, I. L.; Wegand, J. C.; Fayeulle, S.; Gossett, C. R. *Surf. and Coat. Technol.* **1991,** *46,* 207.

235. Walck, S. D.; Donley, M. S.; Zabinski, J. S.; Dyhouse, V. J. *J. Mater. Res.* **1994,** *9(1),* 236.

236. Lince, J. R.; Hilton, M. R.; Bommannavar, A. S. *Surf. and Coat. Technol.* **1990,** *43/44,* 640.

237. Moser, J.; Lévy, F. *J. Mater. Res.* **1993,** *8(1),* 206.

238. Singh, S. R.; Marks, L. D. Northwestern University, unpublished results.

239. Gardos, M. N.; Bohner, J. J. *Tech. Rep.* AFML-TR-79-4091, Part II; December, 1979.

240. Lavik, M. T.; Hubble, R. D.; McConnell, B. D. *Lubr. Eng.* **1975,** *31,* 20.

241. Zabinski, J. S.; Donley, M. S.; McDevitt, N. T. *Wear* **1993,** *165,* 103.

242. Lince, J. R.; Hilton, M. R.; Bommannavar, A. S. *J. Mater. Res.* in press.

243. Lince, J. R.; Hilton, M. R.; Bommannavar, A. S. *Thin Solid Films* in press.

244. Baker, R. T. K.; Chludzinski Jr., J. J.; Sherwood, R. D. *J. Mater. Sci.* **1987,** *22,* 3831.

245. Kim, Y.; Lieber, C. M. *Science* **1992,** *257,* 297.

246. Hilton, M. R., The Aerospace Corporation, CA, personal communications, 1995.